Université de Montréal

Vector Boson Scattering at high energy at the LHC

par
John Paulo Idárraga Muñoz

Département Physique
Faculté des arts et des sciences

Thèse présentée à la Faculté des études supérieures
en vue de l'obtention du grade de Philosophiæ Doctor (Ph.D.)
en Novembre

2008,

Université de Montréal
Faculté des études supérieures

Cette thèse intitulée:

Vector Boson Scattering at high energy at the LHC

présentée par:

John Paulo Idárraga Muñoz

a été évaluée par un jury composé des personnes suivantes:

M. Paranjape,	président-rapporteur
G. Azuelos,	directeur de recherche
C. Leroy,	codirecteur
V. Zacek,	membre du jury
D. Hanna,	examinateur externe

Thèse acceptée le: .....

ABSTRACT

With present and upcoming colliders like the Tevatron and the Large Hadron Collider (LHC), the origin of electroweak symmetry breaking (EWSB) will be explored up to the TeV scale. In the absence of a light Higgs boson (SM or supersymmetry) vector boson scattering will be the best probe for the study of the mechanism of EWSB. Here a Chiral Lagrangian (ChL) Model, inspired by pion scattering, is used to extrapolate to what may happen at LHC energies in such case. This scenario is explored with simulation tools to evaluate the sensitivity of the ATLAS detector to new physics.

We investigate WZ and ZZ scattering in various decay channels with full ATLAS detector simulation. Several techniques for event selection were developed: the study of heavy jets and their inner structure, forward jet tagging and jet veto. A cut-based analysis was implemented using the selections tools mentioned. The very high QCD background associated to the signals studied, was fully taken into account for the first time in VBF studies, also with full simulation. We conclude that to be able to detect this signals with ATLAS we would need an integrated luminosity of about 100fb^{-1}.

TABLE DES MATIÈRES

LISTE DES FIGURES

LISTE DES TABLEAUX

LISTE DES ANNEXES

A mi gente ... a quienes siguen esperando en silencio ...

I want to thank very specially my advisor Georges Azuelos for his confidence and all these years of good and very intense work. Also to the director of the laboratory René-J.-A.-Lévesque and co-director of this thesis, professor Claude Leroy, for the invitation to work on the ATLAS-MPX project. It is needless to say that the time in the lab at the UdeM, at CERN, Prague and all the other destinations, that would have been unthought of five years ago, came to my academic life as the perfect scenario for my formation as a physicist.

It is probably not the best idea trying to write a list of names in this acknowledgment page to all those that I would like to thank. There are too many names and I am afraid I may forget some of them. Still, those memories are wonderful, strong and clear in my mind. I thank YOU ever so much to all who accompanied me through life up to now, and very specially to those who still stand today with me.

Let knowledge help us understanding how to treat our fellow men with more respect.

all my bests,

John P. Idárraga Muñoz

Contributions of the author to the ATLAS experiment

- VBF studies. Study of several channels for high luminosity signals with the ATLAS detector (2004 - 2008). This worked was carried out within the Exotics Physics group of the ATLAS collaboration comprising around 20 researchers from different institutions.

- Production manager for the Exotics Physics group in the CSC excercise (2007-2008).

- Trigger infrastructure. Work done with the ATLAS group at McGill University and the ATLAS trigger group at CERN. Custom hardware was set up and tested at McGill University to help defining final trigger infrastructure for the ATLAS detector (2006 - 2008).

- Trigger online integration. Participation in two trigger groups (jet and missing E_T) (2007 - 2008).

- Low energy radiation in the ATLAS cavern (ATLAS-MPX project). Detector calibration, data model and analysis framework design and implementation. Participated in the installation of MediPix devices at the ATLAS cavern. Development of the online infrastructure for ATLAS-MPX (2007 - 2008).

- Development of monitoring system at point1 for the ATLAS-MPX project (2008).

- Contribution to the online infrastructure for the Inner Detector system (2008).

List of acronyms

EWSB	Electroweak Symmetry Breaking
SBS	Symmetry Breaking Sector
VB	Vector Boson
VBS	Vector Boson Scattering
VBF	Vector Boson Fusion
ChL	Chiral Lagrangian
CSC	Computer Systems Commissioning
SM	Standard Model
EWWG	Electroweak Working Group
e.w.	electroweak
MC	Montecarlo
CERN	European Organization for Nuclear Research
LEP	Large Electron Positron collider
LHC	Large Hadron Collider
ATLAS	A Toroidal LHC ApparatuS
CMS	Compact Muon Solenoid
ALICE	A Large Ion Collider Experiment
LHCb	Large Hadron Collider b-experiment
RODs	Read Out Drivers
SCT	Silicon Tracker
TRT	Transition Radiation Tracker
DAQ	Data Acquisition
FEX	Feature Extraction
HLT	High Level Trigger
EF	Event Filter
EDM	Event Data Model
MDM	Medipix Data Model
THL	Threshold

INTRODUCTION

At the present and upcoming colliders, the Tevatron and the LHC (Large Hadron Collider), some of the most fundamental questions regarding the composition of matter and forces are to be answered in the quest of our understanding of nature. Although the Standard Model (SM) gives an excellent description of known phenomena, it leaves some unanswered questions. It will be essential to search for physics beyond the SM. In particular, the Higgs boson has not been found yet and it may not exist. In such a case we will have to look somewhere else in order to be able to explain the origin of Electroweak Symmetry Breaking (EWSB).

Looking for Vector Boson (VB) scattering at high energy is a way of studying the EWSB sector since this process is not physical in the SM at high energies, and may reveal new physics. In order to properly describe VB scattering at LHC energies, a Chiral Lagrangian (ChL) Model is used here to extrapolate to what may happen at high energies in the eventual absence of a light Higgs Boson, inspired by an effective pion scattering theory that successfully reproduces the vector-boson scattering behavior at low energies. A unitarization procedure, suggests that we will likely have VB resonances. This thesis describes a search for vector boson pair resonances with the ATLAS (**A** Toroidal **LHC** Apparatu**S**) detector, using full simulation, in various decay channels.

The first chapter briefly summarizes the SM of electroweak interactions, drawing attention to the formidable experimental match we get between experiment and the SM predictions. There follows a discussion of the problems that this same theory currently faces, as an invitation to consider new possibilities beyond the SM scenario. In this chapter, I also briefly describe the ChL model and some of the previous work on ChL signals in the past. In the second chapter, I present the ATLAS detector. In the third chapter, I concentrate on the phenomenology of Vector Boson Fusion (VBF) resonances that are predicted by this model which is the main subject of the present work.

The subsequent study is based on simulation, starting from MonteCarlo generation of events of a given process and including full and detailed detector simulation, i.e. the matter-radiation interaction simulation of a physical process. The event reconstruction

of such a simulation is done with state-of-the-art software available at the time, written by the ATLAS collaboration and ourselves, to gather and sort the overwhelming amount of data produced by the detector subsystems. The simulation and reconstruction-studies in this early stage of the ATLAS experience serve also as a very convenient sand-box for future reconstruction-studies on the actual real data. These studies are presented in the fourth chapter.

The analysis of VBS involves many experimental aspects of event-reconstruction. The *jets* in the calorimeters are complicated objects resulting from the recombination of hadrons produced from a high energy primary parton, leaving a collimated deposition of energy in the calorimeter material. Reconstruction tools are still being developed, even if many of the lessons learned from former experiments like D0 and CDF are being used in the process. Algorithms used for event selection have been developed by the author of this thesis and will not be presented in detail here due to the strongly software-oriented nature. In particular, composite jets (dijets from boosted W decay reconstructed as a single jet) must be discriminated from light QCD jets.

Previous work done in the searching for resonances with the ChL model has been performed by a number of groups[14, 15, 16, 17]. In most of these studies the signals have been simulated with fast simulation software (see appendix III) which does not give a realistic picture of the detector effects on the final-state particles that constitute the signal, limiting the prediction power of the studies. Golden channels, with purely leptonic final states, have been found to be measurable but only with $\sim 100\text{fb}^{-1}$ of integrated luminosity. Channels involving hadronic decays of VB's did not have the background properly taken into account before, since multijet processes were simulated with parton showers. For these reasons, the predictions done before on ChL resonances needed to be revised. In this thesis the QCD backgrounds have been taking into account, if not in full, with a more realistic scenario, but still it is found that non-fully-leptonic signals can also contribute to the discovery reach, although a limitation in statistics does not allow us to give precise conclusions. Also, detector effects and the standard reconstruction software available have been used with full simulation of the ATLAS detector (see appendix III) giving a realistic representation of what we may expect with real beam.

Discovery of the physics signals studied here will, in general, require high integrated luminosity. It will require also extremely large samples of simulated backgrounds, fine tuning of all reconstruction algorithms, and a good understanding of the detector performance, which will only gradually develop after the first few years of LHC running. The main purpose of this work is not, therefore, to evaluate with precision the discovery potential of ChL resonances, but to establish some strategy for the search of this important signal. The main emphasis will be put on those aspects most particular to the high mass vector boson scattering process; that is, the reconstruction of hadronically decaying vector bosons at high p_T, and the reconstruction of the high rapidity tag jets.

This work was performed in the framework of the Computer Systems Commissioning (CSC) exercise of ATLAS, which aimed to exercise the whole data production chain: generation, simulation, reconstruction using centrally produced samples with grid tools and official validated software plus analysis tools.

In section 2.10 we draw particular attention to an experimental aspect of this thesis work. We participated in the calibration and further installation of a constellation of pixel detector devices used to measure low energy radiation in the ATLAS cavern and detector.

CHAPTER 1

BEYOND THE STANDARD MODEL, MOTIVATION.

In the last decades, the Standard Model (SM) of electroweak interactions has been thoroughly tested and verified by various precision measurements, principally at LEP[1] and SLC[2]. These measurements have, for example, verified the existence of triple gauge boson couplings and have even predicted the mass of the top quark from precision observables before it was discovered at the Tevatron[3]. They now serve to impose severe constraints on any theory beyond the SM.

The SM is, to this day, the most successful effort at unifying the electromagnetic and weak interactions. There remain, however, a number of fundamental questions to be answered by such a theory as well as a proper justification for some elements that are introduced completely *ad hoc*. The idea of an elementary Higgs field with a quadratic potential is a plausible mechanism, but there is no reason why it would be the only option, and more importantly, the particle associated with this field has not been found experimentally.

A clearer understanding of the origin of the electroweak symmetry breaking (EWSB) sector will require a higher energy scale than has been available until now. With former and current experiments like those at LEP and the Tevatron, we have explored the region around the electroweak scale ($\sim$ 100 GeV). The LEP experiments have yielded such precision measurements that the indirect sensitivity to electroweak physics can already put serious constraints on what we may be able to see directly at future colliders.

The Large Hadron Collider (LHC), with a new generation of experiments, will be able to reach energies suitable for a better understanding of EWSB. LHC and its four experiments[4] (ATLAS, CMS, ALICE and LHCb) will provide direct sensitivity to the $\sim$ TeV region. As we will show, we are essentially guaranteed to find either a SM Higgs

[1] Large Electron Proton (CERN).
[2] Stanford Linear Collider (CA, USA).
[3] Fermi National Laboratory (IL, USA).
[4] Presented on chapter 2, paying great attention to ATLAS.

boson, or new physics phenomena related to the origin of the Symmetry Breaking Sector (SBS).

In this chapter, after a reminder of the weaknesses of the Standard Model of EWSB, we briefly review alternative models and motivate the search for signals from a model-independent effective theory of EWSB.

1.1 Basic assumptions of the SM

Before reviewing alternative models of EWSB, we will briefly sketch the basic ideas of the SM. From numerous experiments in high-energy physics, we know that the electromagnetic and weak interactions can be described in terms of a non-abelian gauge theory with spontaneously broken $SU(2)_L \times U(1)_Y$ symmetry.

The particle spectrum is made up of three families of quarks and leptons as shown in Table 1.I.

			Q_{em}	T_3	$Y/2$
Leptons					
$\begin{pmatrix} \nu_e \\ e \end{pmatrix}_L$	$\begin{pmatrix} \nu_\mu \\ \mu \end{pmatrix}_L$	$\begin{pmatrix} \nu_\tau \\ \tau \end{pmatrix}_L$	0 -1	$+1/2$ $-1/2$	-1 -1
e_R	μ_R	τ_R	-1	0	-2
Quarks					
$\begin{pmatrix} u \\ d \end{pmatrix}_L$	$\begin{pmatrix} c \\ s \end{pmatrix}_L$	$\begin{pmatrix} t \\ b \end{pmatrix}_L$	$+2/3$ $-1/3$	$+1/2$ $-1/2$	$+1/3$ $+1/3$
u_R	c_R	t_R	$+2/3$	0	$+4/3$
d_R	s_R	b_R	$-1/3$	0	$-2/3$

Table 1.I: SM fermion spectrum. Q_{em} is the electromagnetic charge, T_3 corresponds to the third component of isospin and Y is the hypercharge.

The fermions are chiral, and left-handed and right-handed fermions have a different form of interaction. They are represented as left-handed doublets and right-handed singlets of weak isospin $SU(2)_L$.

The Lagrangian of the Standard Model includes interactions of fermions with the weak bosons, a quantum-field theory description which has evolved from the current-

current effective-description that Enrico Fermi constructed in the 30's as a first explanation of β decay.

The existence of charged and neutral weak interactions suggests that we can combine the electromagnetic and weak interactions in a gauge group $SU(2)_L \times U(1)_Y$. We have chosen $SU(2)_L$ because we know that the weak interaction couples to left-handed fermions only, violating parity conservation.

In quantum field theory, invariance under a local symmetry transformation (i.e. a transformation $\psi' = \psi e^{i\alpha(x).T}$, where α is not a constant but a function of the space and T is the generator of the symmetry group) implies the existence of massless gauge fields. In the case of Quantum Electrodynamics (QED) for example, gauge invariance produces a boson that is massless i.e., the photon with, consequently, a long range interaction. The vector bosons of the weak interaction could also derive from local gauge invariance. However, as we have just explained, local gauge invariance implies that we have massless gauge bosons, which we know is not the case. To solve this problem we invoke the Higgs mechanism. We include a complex doublet scalar field, the Higgs field, that takes part in the spontaneous symmetry breaking. It is defined as

$$\Phi = \begin{pmatrix} \phi^+ \\ \phi^0 \end{pmatrix}, \tag{1.1}$$

with charged ($T_3 = +1/2$) and neutral ($T_3 = -1/2$) weak isospin components.

The scalar part of the SM Lagrangian is

$$\mathcal{L}_{scalar} = \mathcal{D}^\mu \phi \mathcal{D}_\mu \phi - V(\phi^\dagger \phi) \tag{1.2}$$

where the covariant derivative $\mathcal{D}^\mu$ is introduced to preserve the invariance under the symmetry group transformation. It can be defined as

$$\mathcal{D}^\mu = \partial^\mu + i\frac{g'}{2}B^\mu Y + i\frac{g}{2}\vec{\tau}\cdot\vec{W}^\mu. \tag{1.3}$$

The second term in Eq. 1.3 is associated with $U(1)_Y$ and the third term refers to $SU(2)_L$, each symmetry group containing its respective bosons B^μ and W^+_μ, W^0_μ, W^-_μ.

Y is the weak hypercharge (quantum number associated with $U(1)_Y$) and τ is the third component of weak isospin. Both are related to the electric charge Q through the Gell-Mann-Nishijima relation

$$Q = \tau_3 + Y/2. \tag{1.4}$$

g' and g are the coupling constants associated with the $U(1)_Y$ and $SU(2)_L$ groups respectively.

In the SM, the potential in Eq. 1.2 is assumed to be of the form

$$V(\Phi^\dagger\Phi) = \mu^2\Phi^\dagger\Phi + \lambda(\Phi^\dagger\Phi)^2. \tag{1.5}$$

It includes a self-interacting term (second term).

When $\mu^2 < 0$, the potential has the well known shape of Mexican hat and thus does not have a minimum at $\phi = 0$. The symmetry is said to be spontaneously broken when one solution for the vacuum expectation value of the Higgs field is chosen. We can write the vacuum solution as

$$< \Phi >_0 = \begin{pmatrix} 0 \\ v/\sqrt{2} \end{pmatrix} \tag{1.6}$$

where

$$v = \sqrt{-\frac{\mu^2}{\lambda}}. \tag{1.7}$$

Around this vacuum expectation value, the Higgs scalar doublet is

$$\Phi = \frac{1}{\sqrt{2}} \begin{pmatrix} 0 \\ v + h \end{pmatrix} e^{i\frac{\vec{\xi}\cdot\vec{\tau}}{2v}}. \tag{1.8}$$

The fields $\vec{\xi}$ will be "eaten" to give mass to the gauge bosons of the weak interaction and the field h remains at the Higgs boson.

Expanding the various components of the SM Lagrangian, we can identify mass

terms for the gauge bosons

$$\frac{g^2v^2}{2}(W_\mu^{+\dagger}W^{+\mu} + W_\mu^{-\dagger}W^{-\mu}) \tag{1.9}$$

$$\frac{g^2v^2}{8\cos\theta_w{}^2}Z_\mu Z^\mu \tag{1.10}$$

where a proper combination of the fields associated with $U(1)$ and $SU(2)$ results in the definition of the gauge boson mediators of the weak and electromagnetic interactions

$$W_\mu^\pm = \frac{1}{\sqrt{2}}(W_\mu^1 \mp W_\mu^2), \tag{1.11}$$

$$\begin{pmatrix} A_\mu \\ Z_\mu \end{pmatrix} = \begin{pmatrix} \cos\theta_W & \sin\theta_W \\ -\sin\theta_W & \cos\theta_W \end{pmatrix} \begin{pmatrix} B_\mu \\ W_\mu^3 \end{pmatrix}, \tag{1.12}$$

where θ_w is called the Weinberg angle and the relation with the $SU(2)$ and $U(1)$ coupling constants hold

$$\sin\theta_W = \frac{g'}{\sqrt{g^2+g'^2}}, \quad \cos\theta_W = \frac{g}{\sqrt{g^2+g'^2}}. \tag{1.13}$$

Thus the following values for the masses are obtained

$$\begin{aligned} M_\gamma &= 0 \\ M_{W^\pm} &= \frac{gv}{2} \\ M_Z &= \frac{M_{W^\pm}}{\cos\theta_w}. \end{aligned} \tag{1.14}$$

We see that the photon has remained massless as desired. The value of v is 246 GeV. In summary, the symmetry breaking involves the inclusion of a complex spin-0, weak isospin-$1/2$ field (see equation 1.1) that we call the Higgs doublet. Three of the four components of the isodoublet become Goldstone bosons that combine with the gauge fields

to result in massive $W^{\pm}$ and Z^0 gauge bosons. In addition, the photon remains massless since the Gell-Mann-Nishijima relation (Eq. 1.4) forces invariance under a transformation by one linear combination of the group generators whose symmetry has not been broken. The fourth physical component of the Higgs isodoublet is a massive object called the Higgs Boson.

Self-interaction terms for vector bosons also result from the SM Lagrangian, they include the following vertices: $WWZ, WW\gamma, WW\gamma\gamma, WW\gamma Z, WWZZ$ and $WWWW$. The interactions ZZZ or $ZZ\gamma$ are not present.

Electroweak couplings to fermions involve charged and neutral interactions (having performed already proper rotations of the fields as in Eq. 1.12). They also involve interaction with the Higgs boson via Yukawa couplings, proportional to the fermions masses

$$\begin{aligned}
\mathcal{L}_{\text{fermion}} &= \sum_i \bar{\psi}_i \left(i\partial\!\!\!/ - m_i - \frac{g m_i H}{2M_W} \right) \psi_i \\
&\quad -\frac{g}{2\sqrt{2}} \sum_i \bar{\psi}_i \gamma^\mu (1-\gamma^5)(T^+ W_\mu^+ + T^- W_\mu^-)\psi_i \\
&\quad -e \sum_i q_i \bar{\psi}_i \gamma^\mu \psi_i A_\mu \\
&\quad -\frac{g}{2\cos\theta_W} \sum \bar{\psi}_i \gamma^\mu (g_V^i - g_A^i \gamma^5)\psi_i Z_\mu
\end{aligned} \tag{1.15}$$

where $g_V = T_3^i - 2Q_i \sin^2\theta_W$ and $g_A = T_3^i$, where Q_i is the electric charge of fermion i. We can easily identify from equation 1.15 the electromagnetic current coupled to the photon field A_μ and the electromagnetic coupling to be

$$e = g \sin\theta_W = g' \cos\theta_W. \tag{1.16}$$

The Lagrangian in equation 1.15 reproduces the $(V - A)$ structure of the weak charged-and-neutral currents, one of the most remarkable characteristics of the SM, i.e. weak interactions with parity violation and including neutral currents.

1.2 Limits on the Higgs boson mass

As was mentioned above, diagrams involving a light Higgs boson are essential for the vector boson (VB) scattering process. Without them, perturbative unitarity is violated at energies $\sim$ 1.2 TeV [1], meaning that the cross section becomes strong and the probability of an interaction becomes effectively > 1 which is, of course, unphysical. The reason is that the Goldstone bosons have interactions which grow with energy, and they will eventually violate perturbative unitarity if the energy is high enough.

Unitarity violation can be seen by writing the differential cross section in terms of partial waves and using the optical theorem, which states that the total cross section is the imaginary part of the amplitude at zero degrees of scattering angle [18] (see also section 1.7.2). This leads to the following unitarity conditions

$$\begin{aligned} |a_l|^2 &= \mathrm{Im}(a_l) \\ |Re(a_l)| &< \frac{1}{2}, \end{aligned} \tag{1.17}$$

where a_l correspond to the spin l partial wave.

Let us consider then the scattering of longitudinal gauge bosons, $W_L^+W_L^- \rightarrow W_L^+W_L^-$, which can be calculated to $\mathcal{O}(M_W^2)/s$ from Goldstone boson scattering. We will see later in section 1.8 that the scattering amplitude of longitudinal vector bosons turns out to be approximately the same as the scattering amplitude of Goldstone bosons (the equivalence theorem). Going to very high energy, $s >> M_h^2$, it has the limit:

$$a_0^0(\omega^+\omega^- \rightarrow \omega^+\omega^-) \overset{s>>M_h^2}{\longrightarrow} -\frac{M_h^2}{8\pi v^2}. \tag{1.18}$$

Applying the unitarity condition, $|\mathrm{Re}(a_0^0)| < 1/2$, (Eq. 1.18) gives the restriction

$$M_h < 870 \text{ GeV}. \tag{1.19}$$

It means that for heavier masses of the Higgs boson perturbation theory is not valid

anymore and unitarity is violated (it corresponds to an indirect limit on the Higgs mass). Let us now apply the limit where the Higgs boson has a mass much heavier than the energy scale. In this limit the partial wave

$$a_0^0(\omega^+\omega^- \to \omega^+\omega^-) \overset{s<<M_h^2}{\longrightarrow} -\frac{s}{32\pi v^2}, \tag{1.20}$$

from where, applying again the unitarity condition it can be found that it is valid only for

$$\sqrt{s_c} < 1.7 \text{ TeV}, \tag{1.21}$$

according to Eq. 1.20. Conditions on Eq. 1.19 and Eq. 1.21 coming from limits on Eq. 1.18 and Eq. 1.20 and the unitarity conditions in Eq. 1.17 constitute the motivation of this work and the promise of finding interesting information from VB scattering at high energy at the LHC. Whether we discover a light Higgs with $M_h < 870$ GeV, in which case the SM or SUSY would be a good description, or we find something new in the TeV region. In fact, the only way to avoid a light Higgs is to presume new physics at high energy.

Other indirect limits on the Higgs mass come from triviality and vacuum stability [1] bounds, which can be determined as a function of the scale Λ as we can see in Fig. 1.1. The Higss mass is quite restricted (around 160 GeV) if the SM is to be valid up to the Planck scale $\sim 10^{19}$ GeV. Conversely, if the SM is valid only up to a few TeV's the Higgs mass is loosely constrained by these theoretical considerations.

1.3 Why the Standard Model is inadequate.

Having in mind that the SM has achieved a remarkable and unprecedented success as a theory of the fundamental interactions, it is clear today that it is nevertheless inadequate for a number of reasons:

- **The Higgs boson has not been found yet**

  As is discussed in section 1.4, based on electroweak precisions measurements at

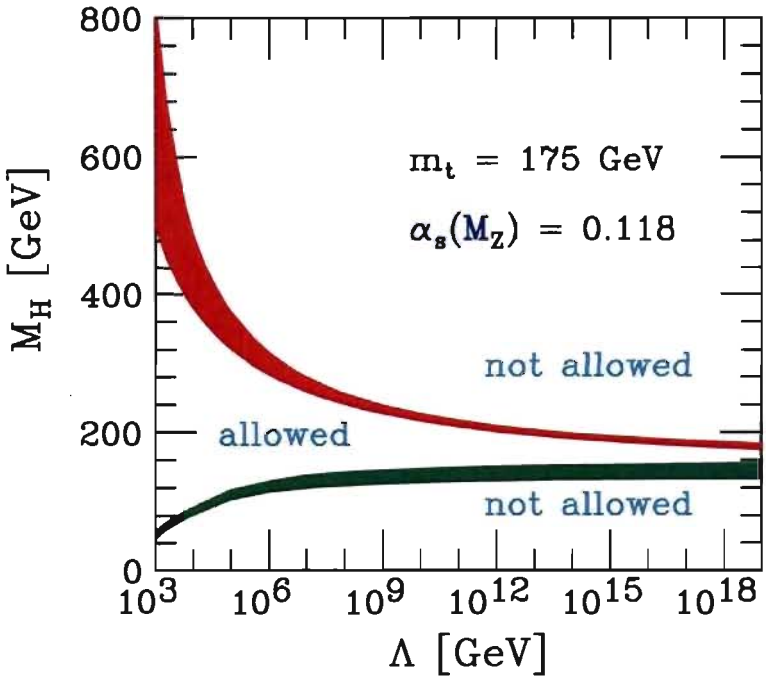

Figure 1.1: The triviality (upper) bound and the vacuum stability (lower) bound on the Higgs boson mass as a function of the New Physics or cut–off scale Λ for a top quark mass $m_t = 175 \pm 6$ GeV and $\alpha_s(M_Z) = 0.118 \pm 0.002$ [1].

LEP, if the SM model is valid the Higgs mass should not be much higher than its present experimental lower bound. Our best guess of the Higgs boson mass has already been excluded, but the LHC will explore higher masses.

- **No dynamical explanation of EWSB:**

  As pointed out before, the symmetry breaking mechanism has no dynamical origin. In the SM it is put by hand by forcing a μ^2 coefficient in the scalar potential to be negative. There is no reason, in the SM, for this to be the case.

- **Hierarchy problem:**

  The enormous difference between the scale of electroweak interactions, set by the vacuum expectation value (vev) of the scalar Higgs field, 246 GeV, and the Planck scale of gravitation $\sim 10^{19}$ GeV, is known as the *big* hierarchy problem. Why is that a problem ? It is not strictly speaking a problem, but is unnatural. We would

expect a full theory, valid at all energies, to explain at about the same scale of energy, the electroweak, strong and gravitational forces.

- **Fine tuning:**

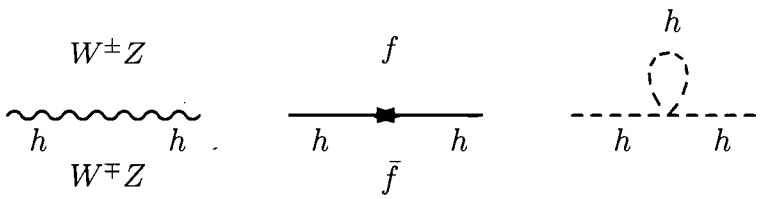

Figure 1.2: Corrections to the higgs field propagator. From left to right, the first diagram includes a loop with vector bosons W or Z, the second diagram brings a fermionic loop and the last one is the self energy correction.

Perturbative calculations in quantum field theory are often accompanied by the presence of divergences. Corrections coming from the higher order terms in the expansion, as in diagrams shown in 1.2 and higher orders, have values which diverge quadratically with the scale Λ up to which the SM is assumed to be valid. These corrections have to cancel to an extremely high degree of precision, which is unnatural.

- **Why three families ?**

  Three fermion families are used to build the particle spectrum in the SM. This is based on the experimental determination of the number of light neutrino types N_ν at LEP, from studies of the Z width in e^+e^- collisions [19]. A determination of the invisible partial width Γ_{inv} is obtained by subtracting the visible partial widths that correspond to charged-leptons and hadronic decays from the total Z width. The combined result from the four LEP experiments gives $N_\nu = 2.984 \pm 0.008$ [20]. This suggest that the number of light neutrinos should be 3, in agreement with the SM particle spectrum. However, there could exist heavier families since this method of determining N_ν is not sensitive when the decay $Z \rightarrow \nu_i\bar{\nu}_i$ is kinematically forbidden. The fact that there are three families is not explained by the SM.

- **Not a unification for electromagnetic and weak interactions**

  We have 3 couplings: g, $g^{'}$ and α_s. If they were truly unified, we could expect a unified group with a single coupling. Is the SM symmetry group a subgroup of a grand unification theory (GUT) ?

- **Left-handed coupling**

  It seems unnatural that there should be a left-handed coupling to fermions, but not a right-handed one. Again, the SM is perhaps a subgroup of a GUT.

- **Yukawa couplings:**

  These couplings in the SM Lagrangian are completely *ad hoc*. There is no explanation as to why, for example, the electron is light and the top quark heavy.

- **Neutrino mass:**

  Perhaps the first concrete indication of physics beyond the SM, is the existence of neutrinos with non-zero mass. There is now experimentally strong proof of neutrino oscillations [21], which implies that they have mass, and hence there must exist a right handed component. Neutrinos were chosen to have no right component in the SM just because, at the time it was proposed, neutrinos were believed to have no mass at all. It is not a problem to extend the SM to have massive neutrinos, but in fact, if introduced by hand, their masses would still be free parameters of the theory.

- **Gravitation is not included:**

  A complete theory of the fundamental interactions and particles should include gravitation which is missing in the SM.

- **No dark matter candidate:**

  There is no particle accounting for dark matter in the SM. We know from observation that dark matter exists.

I have dedicated this section to some of the problems and issues of the Standard Model. Nevertheless, I would like to stress the fact that the SM is certainly one of

the most successful theories ever developed in physics, delivering a description of the fundamental interactions (except by gravity) in a coherent framework.

For all the reasons mentioned above it is important that we consider alternative models of EWSB.

1.4 What we do know from precision measurements

The electroweak bosons of the SM ($W^{\pm}$,Z^0) have been discovered at the SPS collider at CERN in 1983-84 [22, 23] and have been studied in detail at LEP. Conversely, the Higgs boson, whose exact mass is not determined by theory, remains elusive and has been searched for by high energy physicists for many years. The observation of this particle, and confirmation of its couplings, would strongly support the symmetry breaking mechanism implicit in the SM.

The precision measurements obtained with the LEP results (and other experiments) are an unquestionable proof of the predictive power of the theory. Some key results from the Electroweak Working Group[5] (EWWG) are discussed here. In Fig. 1.3 we see the measurements on the W boson and the correlation with the Higgs mass from a global fit to the SM which suggests that $m_H \sim 100$ GeV. In fact direct searches for the Higgs boson find that its mass must be higher than 114.3 GeV (95 percent confidence level limit), indicated in the excluded area in Fig. 1.4 (right plot). On the left plot we also have the correlation between the W mass and the top quark mass for different Higgs masses which strongly suggest a light Higgs, given the experimental contour limits at 68% CL (in red-solid and blue-dashed lines), thanks to the precision in the measurement of the W and top masses. It is remarkable that the top mass was predicted with such high precision by indirect measurements of electroweak observables before it was discovered at the Tevatron.

Other quantities in the theory can be calculated to produce observables that can be compared with experiment. One case is the leptonic couplings g_V,g_A shown in Fig. 1.6 which suggest again a low Higgs mass (in the range of $\sim$ 100 GeV), if lepton universality

[5] http://lepewwg.web.cern.ch/LEPEWWG/

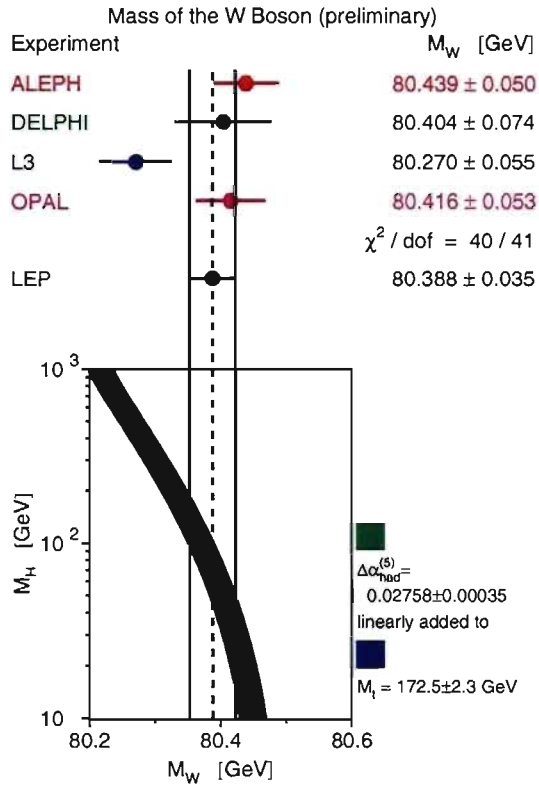

Figure 1.3: Precision measurements on the mass of the W boson. From EWWG - winter 2006.

if assumed.

The limits on the Higgs mass from indirect searches thus seem to suggest a discovery that is *around the corner*. The LHC takes us to that point and beyond. As we stated before, the Higgs boson plays a very important role in the SM. Not only does it represent the fundamental piece of the Higgs mechanism but it also guarantees regularization of the amplitudes for the electroweak-boson scattering processes. It also guarantees the renormalizability of the theory. But what if the LHC does not find the fundamental scalar of the SM ? The absence of the Higgs would compel the physics community to come out with a different description of the low energy SM dynamics.

Electroweak constraints from LEP precision data have already imposed some bounds on new physics at new colliders. Let us take for example the S, T, U Peskin and Takeuchi parameters. These variables parametrize, in a model-independent way, higher

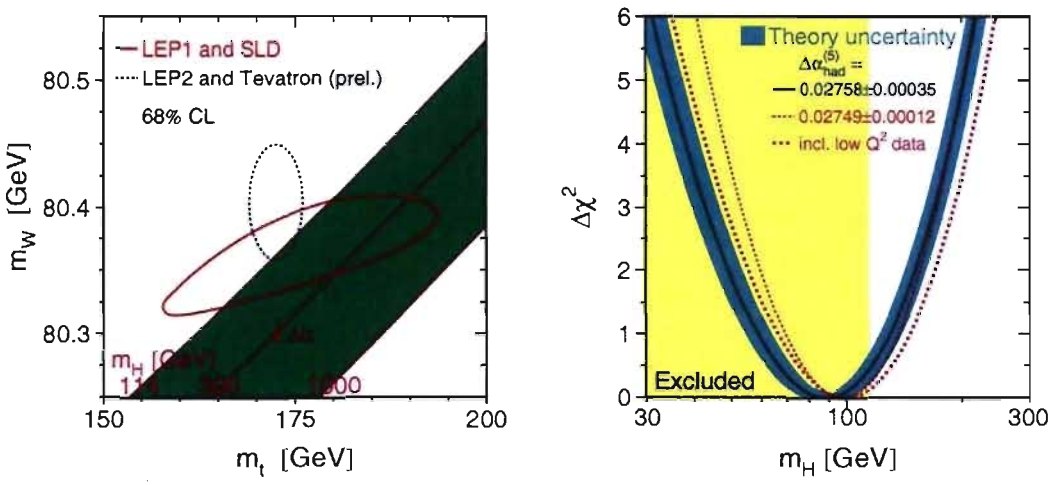

Figure 1.4: Precision measurements on the top mass (left) and $\Delta\chi^2$ curve for the Higgs mass (right). From EWWG - winter 2006.

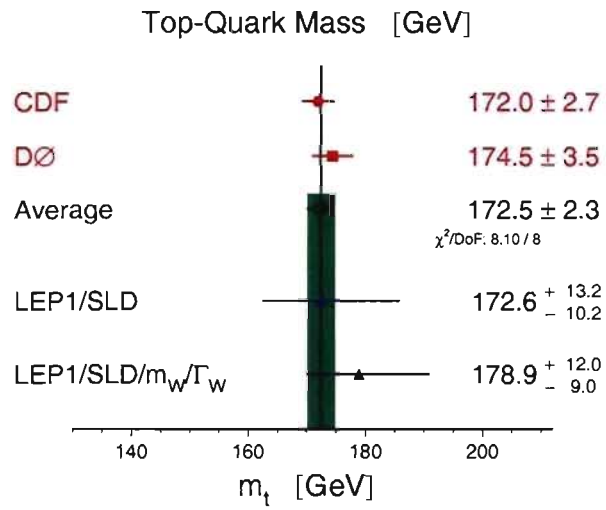

Figure 1.5: Precision measurements on the top mass for different experiments. From EWWG - winter 2006.

order corrections due to additional particles in loops in the SM model, and any deviation from their zero value within the SM should suggest the presence of new physics. On Fig. 1.7[2] we see the contour curve at 68% probability in the (T, S) plane. Within that

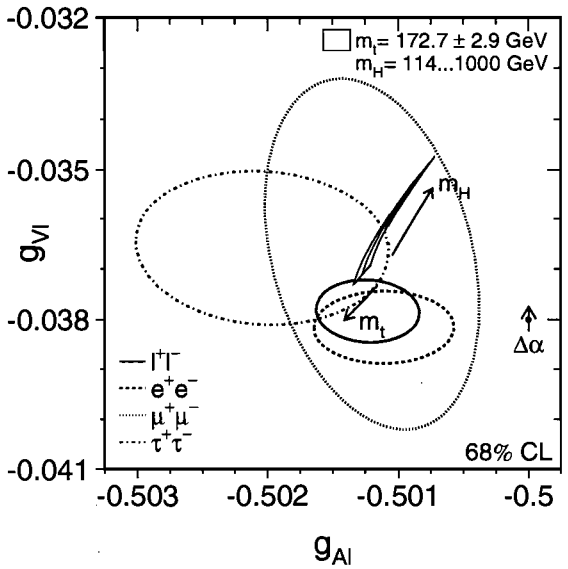

Figure 1.6: Leptonic couplings g_A,g_V. From EWWG - summer 2005.

region a very small range of Higgs masses is allowed. The shaded (yellow) region shows the predictions from different observables within the SM for $M_t = 178.0 \pm 4.3$ GeV (Tevatron Run-I) and $M_H = 300^{+700}_{-186}$ GeV. The SM reference point at which all S, T, U parameters vanish is chosen to be: $\Delta\alpha^{(5)}_{\rm had}(M_Z^2) = 0.02758$, $\alpha_{\rm S}(M_Z^2) = 0.118$, $M_Z = 91.1875$ GeV, $M_t = 175$ GeV, $M_H = 150$ GeV. The constraint $U = 0$ is always applied. (Note that the latest value for the top mass is $M_t = 170.9 \pm 1.1$ (stat) ± 1.5 (systematic) GeV [24]).

1.5 Models of EWSB

The assumption of spontaneous symmetry breaking is a mathematical description that gives mass to the vector bosons and fermions, but does not explain the origin of the Yukawa couplings, nor does it address the hierarchy problem: why would the physics responsible for the Higgs mechanism appear at such low scale ($\sim$ TeV) compared to the fundamental Planck scale ? With future experiments (like LHC) where we will be able

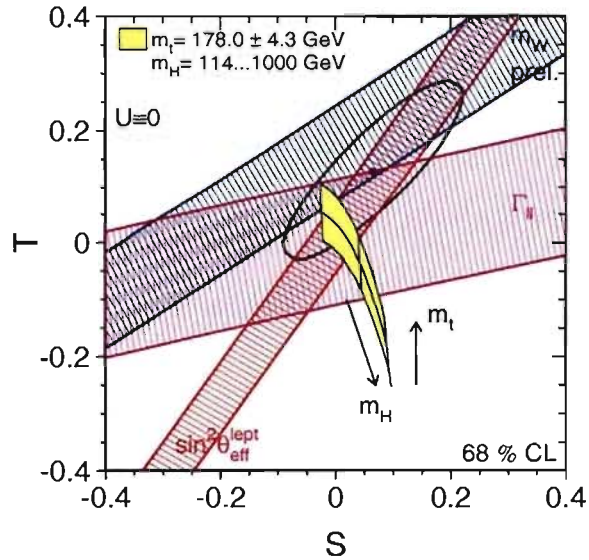

Figure 1.7: Electroweak constraints from LEP precision data. [2]. Contour curve of 68% probability in the (T, S) plane.

to look at phenomena directly happening at the electroweak scale and above, we will explore an energy domain where the simple SM Higgs mechanism may no longer be satisfactory and a better understanding could emerge.

1.5.1 SUSY

Supersymmetry (SUSY) is one of the most appealing theoretical scenarios where the flaws of the standard model discussed on section 1.3 can be solved altogether in a theory of the fundamental interactions. In SUSY, for each field, a supersymmetric partner is introduced. This denotes a symmetry between scalars and fermions which produces an extended spectrum of particles organized in superfields. Divergences are cancelled by the presence of both scalars and fermions in loops in the calculations. As a particular characteristic, in the most simple version of SUSY [25] called Minimal Supersymmetric SM (MSSM), a second higgs-doublet is present and 5 Higgs fields appear. The lightest

of those Higgs's has a mass of < 130 GeV.

Supersymmetry is a theoretical framework where:

- Divergences are canceled in a natural way by the supersymmetric fields, thus, the hierarchy problem is not present.
- It is an unification theory where the electroweak and strong forces find their common origin at very high energy. It also opens the possibility to include gravity in SUSY.
- A light Higgs is present.
- A dark matter candidate, the neutralino $\tilde{\chi}^0$, is predicted.

On the other hand, despite the big theoretical success of SUSY, from previous experiments, no evidence of the supersymmetric particles nor the Higgs bosons has been found. Supersymmetry will be widely tested at LHC since many of its predictions should be seen at LHC energies. For instance, the mass of the lightest so-called *super-partners* is expected to be in the region of < 1 TeV, and therefore evidence of SUSY, if it is a correct description of nature, should be seen. SUSY has, however, a very large parameter space and one can say that a large part of it, in simple models, is already excluded experimentally.

1.6 Beyond SM

A number of alternative EWSB scenarios exist. In most of the cases these proposals include new particles that are to be discovered, as in the case of multiple Higgs-doublet models (MHDM), or supersymmetric theory (as discussed in section 1.5.1). Other attempts use dynamical symmetry breaking as in the case of Technicolor models where a new interaction, copied from QCD, is introduced at higher scale. Technicolor introduces new massless fermions whose chiral symmetry is spontaneously broken by a mechanism that at the same time is responsable for EWSB (fermion condensate) [26]. For the intermediary particles, three of the Goldstone bosons (so called technipions [27]) produced

at the breaking of the chiral symmetry, provide the longitudinal components that give mass to the $W^{\pm}$ and Z bosons.

Another option for EWSB comes from theories with extra dimensions. It has been realized in the last years that compactified extra dimensions could actually play an active role in the physics at the TeV scale bringing the true Planck scale to the TeV range. Among extra dimensions theories are the *Higgsless* models, meaning that nothing like the Higgs mechanism is needed to achieve EWSB. For example the observed vector boson masses are Kaluza-Klein states of gauge bosons propagating in the fifth (warped) extra dimension, satisfying certain boundary conditions at fixed branes. They constitute a suitable candidate for physics beyond SM. Some of these theories, where we could explain the discrepancy of the electroweak and the Planck scale by the presence of extra space dimensions, are actually predicting resonances in the energy range reachable at the LHC and we will be able to test them in the years to come [28].

A way to look at some of these alternative models of EWSB is the search for resonances in VB scattering as shown in Fig. 1.8. The K-matrix and Padé unitarization are described in section 1.7.2.

In this chapter we will visit one appealing possibility to explain phenomena beyond the SM capabilities, and very importantly, without the use of the Higgs mechanism. This approach is achieved by starting from a non-renormalizable field theory using a Lagrangian with chiral symmetry. This theory describes properly low-energy physics and we will try to extrapolate to LHC energies. With this extrapolation we will find that unitarity is violated at high energy and the theory alone would fail describing phenomena at the range of $\sim$ TeV. Fortunately, a regularization method can be implemented to safely calculate observables at LHC energies up to around 3 TeV. This Chiral Lagrangian model (ChL) constitutes an effective theory that is not, by any means, an attempt to make a fundamental descriptions of the electroweak interactions and a proper implementation of EWSB, but an effective approach to describe what may happen in the absence of a light Higgs bosons at LHC energies. In particular, we are interested in the part of the Lagrangian that has to do with Vector Boson Scattering, believing that the study of those interactions at high energy may shed light on a fundamental approach to the EWSB

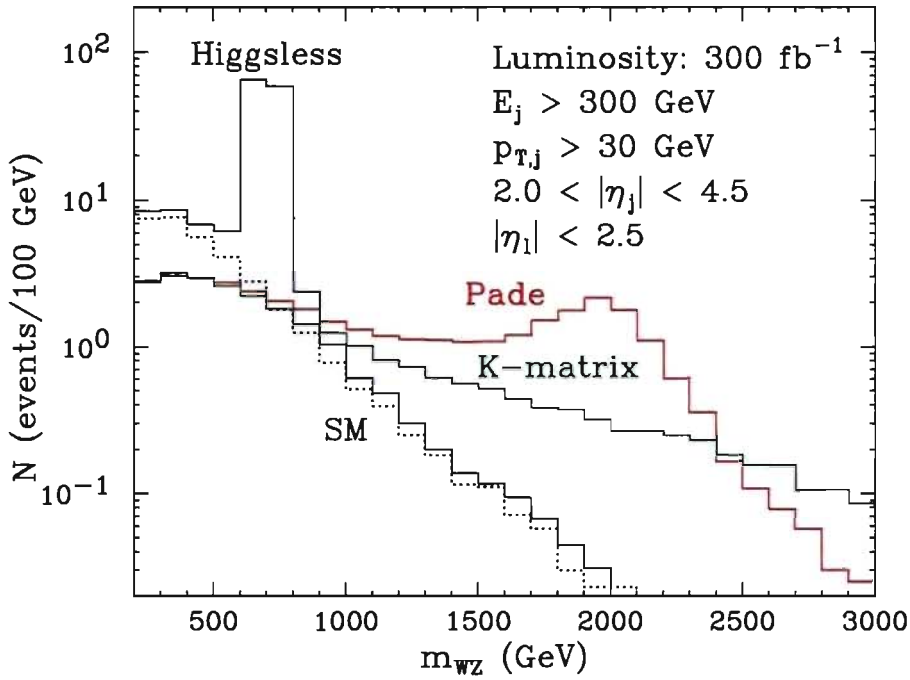

Figure 1.8: WZ elastic scattering resonances in the SM (dotted), Higgsless model (blue), and two unitarization models: Padé (red) and K-matrix (green). See section 1.7.2.

sector as it will be explained later on this chapter. Since the parameter space for such a theory is in principle infinite, one can say that any result we might be able to pull from it, properly reproducing observable phenomena, could hopefully be predicted by some fundamental underlying theory which we know nothing about. This theory may be one of the proposed possibilities above or something completely new that we have not thought of yet, hopefully again solving the hierarchy problem and proposing a proper implementation of the EWSB sector.

In the search for an appropriate and higgless symmetry breaking sector for the electroweak interactions, one can consider two different views. On the one hand, as in the SM, we could think that the electroweak gauge symmetry is an *an accidental* approximate symmetry which brings us back to the hierarchy problem where we would have to accept that the extremely small breaking terms $v_{\text{e.w.}}/M_{Planck} \sim 10^{-17}$ are pure coincidence, and it seems just too unnatural. On the other hand we could think that electroweak gauge symmetry is a good description but is incomplete, with more new physics present

at high energies.

However, building a satisfactory theory of fundamental particles and forces has proven to be a complicated task mainly because the whole spectrum of known particles is quite difficult to accommodate in a natural way, without awkward parametrization, i.e. very light leptons and quarks and a heavy top quark within the same description. Furthermore, even if it is clearly worthwhile to search for signals of specific models in future colliders like the LHC, the energy range is still limited and we may not be able to access new states associated with the EWSB sector directly. In such situation a model-independent approach to the dynamics we are searching for, might be an easier base line for new physics searches.

1.7 The Chiral Lagrangian model

If the symmetry-breaking mechanism, either from the standard model, from supersymmetry (MSSM), or from little Higgs models, is not valid, we could expect that there will not exist a light Higgs boson. In this case as we have seen, the interaction between vector bosons becomes strong at high energies. The best probe of alternative models of EWSB is then VBS in the high energy regime. The ChL model [29, 30] is an effective theory that reproduces well the phenomenology of VBS at low energy and includes terms that should allow extrapolation to higher energies. For a detailed description of the model see [31].

At very low energies, below the mass of the W and Z, QED and QCD forces dominate the interactions between leptons and quarks. The Lagrangian includes mass terms of dimension 3 (fermions have dimension $3/2$ and bosons dimension 1) such as

$$\bar{Q}_L M_Q Q_R \tag{1.22}$$

where Q_L and Q_R are isospin doublets

$$Q_{L,R} = \begin{pmatrix} U_{L,R} \\ D_{L,R} \end{pmatrix} \tag{1.23}$$

and similarly for leptons. The Lagrangian also includes kinetic and interaction terms of dimension 4 such as

$$i\bar{Q}_L \not{\mathcal{D}} Q_L \tag{1.24}$$

where the covariant derivative $\mathcal{D}_\mu = \partial_\mu + ieqA_\mu$. In addition there is a term for the field energy $-\frac{1}{4}A_{\mu\nu}A^{\mu\nu}$ where $A_{\mu\nu} = \partial_\mu A_\nu - \partial_\nu A_\mu$ is the field energy tensor. At these very low energies, the weak interaction is present as an effective Fermi contact term of dimension 6 such as

$$v_{ijkl}(\bar{f}_i\gamma^\mu f_j)(\bar{f}_k\gamma_\mu f_l) \tag{1.25}$$

where a vector coupling is shown here.

At higher energies, closer to the mass scale of the electroweak vector bosons W and Z, we have to include gauge bosons and their kinetic terms (dimension 4)

$$\mathcal{L}_{4(W)} = \frac{1}{2}tr[\boldsymbol{W}_{\mu\nu}\boldsymbol{W}^{\mu\nu}] - \frac{1}{2}tr[\boldsymbol{B}_{\mu\nu}\boldsymbol{B}^{\mu\nu}], \tag{1.26}$$

where the field strength tensors are defined in terms of vector fields W^a $(a = 1, 2, 3)$ and B

$$\boldsymbol{W}_{\mu\nu} = \partial_\mu \boldsymbol{W}_\nu - \partial_\nu \boldsymbol{W}_\mu + ig[\boldsymbol{W}_\mu, \boldsymbol{W}_\nu] \tag{1.27}$$

$$\boldsymbol{B}_{\mu\nu} = \partial_\mu \boldsymbol{B}_\nu - \partial_\nu \boldsymbol{B}_\mu \tag{1.28}$$

with $\boldsymbol{W}_\mu = W^a_\mu \frac{\tau^a}{2}$ and $\boldsymbol{B}_\mu = B_\mu \frac{\tau^3}{2}$, where τ^a are the isospin operators of $SU(2)$ and τ^3 is the third component of weak isospin.

Mass terms (dimension 2)

$$M_W^2 W^{+\mu}W^-_\mu + \frac{1}{2}M_Z^2 Z^\mu Z_\mu \tag{1.29}$$

and Eq. 1.22 are not invariant. In Eq. 1.29 $W^\pm = \frac{1}{\sqrt{2}}(W^1 \mp W^2)$ and $Z = \cos\theta_W W^3 -$

$\sin\theta_W B$. To overcome this problem we make use of the non-linear sigma model. Since only three vector bosons acquire mass and no Higgs boson should remain, we introduce three scalar fields only (unlike the Higgs field which has 4 degrees of freedom). These fields are grouped into one sigma field represented as a 2×2 unitary matrix

$$\Sigma = e^{(-i\boldsymbol{w}(\boldsymbol{x})/v)}, \quad \text{with } \boldsymbol{w}(\boldsymbol{x}) = \omega(x)_a \tau_a, \quad a = 1, 2, 3 \tag{1.30}$$

The field Σ transforms like

$$\Sigma \rightarrow U(x)\Sigma V^\dagger(x) \tag{1.31}$$

where $U(x)$ is an $SU(2)_L$ transformation ($e^{i\alpha(x)\cdot\vec{\tau}/2}$) and $V(x)$ is a $U(1)_Y$ transformation ($e^{i\beta(x)/2}$). The quark mass terms are now

$$\bar{Q}_L \Sigma M_Q Q_R \tag{1.32}$$

which have the required symmetry [31].

The desired boson mass terms then result from the kinetic energy term of the sigma field

$$\mathcal{L}_{(W)} = -\frac{v^2}{4} tr[V_\mu V^\mu] \tag{1.33}$$

where $V_\mu = \Sigma(D_\mu\Sigma)^\dagger$ and D_μ is the covariant derivative

$$D_\mu = (\partial_\mu + igW_\mu - ig'B_\mu). \tag{1.34}$$

Fermions couple to gauge bosons via the covariant derivative as in the SM.

1.7.1 Anomalous couplings

It can be shown that the Chiral Lagrangian discussed above is not renormalizable as it does not contain all the possible operators consistent with electroweak symmetry. The term of dimension 4 in Eq. 1.33 was completely determined by the symmetry. Imposing

CP-invariance on the effective Lagrangian, the complete list of other dimension-four operators not contained in this Lagrangian is as follows:

$$\mathcal{L}_1 = \alpha_1 g g' \,\mathrm{tr}\left[\Sigma \mathbf{B}_{\mu\nu} \Sigma^\dagger \mathbf{W}^{\mu\nu}\right] \tag{1.35}$$

$$\mathcal{L}_2 = i\alpha_2 g' \,\mathrm{tr}\left[\Sigma \mathbf{B}_{\mu\nu} \Sigma^\dagger [V^\mu, V^\nu]\right] \tag{1.36}$$

$$\mathcal{L}_3 = i\alpha_3 g \,\mathrm{tr}\left[\mathbf{W}_{\mu\nu} [V^\mu, V^\nu]\right] \tag{1.37}$$

$$\mathcal{L}_4 = \alpha_4 (\mathrm{tr}\left[V_\mu V_\nu\right])^2 \tag{1.38}$$

$$\mathcal{L}_5 = \alpha_5 (\mathrm{tr}\left[V_\mu V^\mu\right])^2 \tag{1.39}$$

$$\mathcal{L}_6 = \alpha_6 \,\mathrm{tr}\left[V_\mu V_\nu\right] \mathrm{tr}\left[T V^\mu\right] \mathrm{tr}\left[T V^\nu\right] \tag{1.40}$$

$$\mathcal{L}_7 = \alpha_7 \,\mathrm{tr}\left[V_\mu V^\mu\right] \mathrm{tr}\left[T V_\nu\right] \mathrm{tr}\left[T V^\nu\right] \tag{1.41}$$

$$\mathcal{L}_8 = \tfrac{1}{4}\alpha_8 g^2 (\mathrm{tr}\left[T \mathbf{W}_{\mu\nu}\right])^2 \tag{1.42}$$

$$\mathcal{L}_9 = \tfrac{i}{2}\alpha_9 g \,\mathrm{tr}\left[T \mathbf{W}_{\mu\nu}\right] \mathrm{tr}\left[T [V^\mu, V^\nu]\right] \tag{1.43}$$

$$\mathcal{L}_{10} = \tfrac{1}{2}\alpha_{10} (\mathrm{tr}\left[T V_\mu\right] \mathrm{tr}\left[T V_\nu\right])^2 \tag{1.44}$$

$$\mathcal{L}_{11} = \alpha_{11} g \epsilon^{\mu\nu\rho\lambda} \,\mathrm{tr}\left[T V_\mu\right] \mathrm{tr}\left[V_\nu \mathbf{W}_{\rho\lambda}\right] \tag{1.45}$$

Only 5 of these terms describe vector boson scattering: those with coefficients α_4, α_5, α_6, α_7 and α_{10}. Under some basic assumptions (custodial symmetry [32, 33]), it is generally expected that only the 2 parameters α_4 and α_5 are important for this process and the Lagrangian is then reduced to:

$$\mathcal{L}_{ChL} = -\frac{v^2}{4} tr[V_\mu V^\mu] + \alpha_4 [tr(V_\mu V_\nu)]^2 + \alpha_5 [tr(V_\mu V^\mu)]^2, \tag{1.46}$$

1.7.2 Unitarization

Up to here, the model is an effective theory at next-to-leading order. It is still non-renormalized, since it is not a complete theory. It is valid up to the scale $4\pi v \sim 3$ TeV, where $v = 246$ GeV is the vacuum expectation value of the Standard Model Higgs field. The theory can therefore provide a description of longitudinal gauge boson scattering at

the TeV scale when no light scalar Higgs boson is present.

We know, however, that at the LHC, vector boson scattering can indeed occur at the TeV energy scale but then, the interaction becomes strong and we are in danger of unitarity violation (see section 1.2). It is therefore necessary to unitarize this model. One popular prescription is the so-called Padé prescription, or Inverse Amplitude Method (IAM) [34], which gives an excellent description of high energy $\pi - \pi$ scattering[3], reproducing observed resonances (see Fig. 1.9).

Let us take for example $2 \longrightarrow 2$ elastic scattering, where the differential cross section is

$$\frac{d\sigma}{d\Omega} = \frac{1}{64\pi^2 s}|\mathcal{A}|^2. \tag{1.47}$$

Written as an expansion in partial waves, the amplitude can be written as

$$\mathcal{A} = 16\pi \sum_{l=0}^{\infty}(2l+1)P_l(\cos\theta)a_l, \tag{1.48}$$

where a_l is the angular momentum l partial wave and $P_l(\cos\theta)$ are the Legendre polynomials. The integrated cross section from Eq. 1.47 becomes

$$\sigma = \frac{16\pi}{s}\sum_{l=0}^{\infty}(2l+1)|a_l|^2. \tag{1.49}$$

The optical theorem [35] states that the total cross section is the imaginary part of the amplitude evaluated at $\theta = 0$.

$$\sigma = \frac{1}{s}Im\left[\mathcal{A}(\theta=0)\right] = \frac{16\pi}{s}\sum_{l=0}^{\infty}(2l+1)|a_l|^2. \tag{1.50}$$

This yields the condition

$$|a_l|^2 = Im(a_l) \quad \text{or} \quad Im\left(\frac{1}{a_l}\right) = -1 \tag{1.51}$$

since a_l can be written as $|a_l|e^{i\phi}$. Therefore, to unitarize an arbitrary amplitude, one prescription would be simply to add $-i$ to $Re\left(\frac{1}{a_l}\right)$. It yields

$$\begin{aligned}\hat{a}_l &= \frac{1}{\mathrm{Re}(1/a_l) - i} \\ &= \frac{a_l}{1 - ia_l} \text{ if } a_l \text{ is real.}\end{aligned} \tag{1.52}$$

On the other hand, elastic unitarity requires that the normalized eigenamplitudes

$$a_l = \frac{1}{32\pi} A_l \tag{1.53}$$

where A_l are the unnormalized eigenamplitudes. Eq. 1.52 can be rewritten as

$$\hat{A}_l = A_l + \Delta A_l \text{ , where } \Delta A_l = \frac{1}{32\pi} \frac{A_l^2}{1 - \frac{i}{32\pi} A_l} \tag{1.54}$$

This is the result of applying K-matrix unitarization procedure [36]. This method does not produce resonances. If the amplitude is dominated by an s-dependent pole of mass M

$$\mathcal{A}(s) = -\frac{M^2}{v^2} \frac{s}{s - M^2}, \tag{1.55}$$

it is transformed into (by the K-matrix prescription)

$$\hat{A}(s) = -\frac{M^2}{v^2} \frac{s}{s - M^2 + iM\Gamma \frac{s}{M^2}} \text{ with } \Gamma = \frac{M^2}{32\pi v^2} M. \tag{1.56}$$

The amplitude in Eq. 1.55 has the low energy expansion. As $s \to 0$, $A(s)$ can be written in power series where $s/M^2 << 1$ as follows

$$A(s) \to \frac{s}{v^2} + \frac{s^2}{M^2 v^2} = A^{(0)}(s) + A^{(1)}(s). \tag{1.57}$$

Eq. 1.56 exactly coincides with what could be obtained by applying the Padé [34] prescription to Eq. 1.57. We can say that, in the present context, the IAM or Padé unitarization is a special case of the K-matrix scheme. We take the IAM to implement the unitarization of the ChL model for VBS because it properly regularizes the amplitudes

respecting chiral symmetry and unitarity, and produces resonances. As we will see later it might be the only way to observe VBS at high energy at the LHC.

The partial wave amplitudes a_{IJ} for each combination of isospin and spin ($I = 0, 1, 2$ and $J = 0, 1$) have been calculated as a function of α_4 and α_5. They can be written as an energy expansion [4]:

$$t_{IJ}(s) = t^2_{IJ}(s) + t^4_{IJ}(s) + O(s^3), \tag{1.58}$$

where the superscript refers to the corresponding power of momenta (dimension 2 refer from the part of the Lagrangian in Eq. 1.33 and dimension 4 from terms involving α_4 and α_5 in equations 1.38 and 1.39). The EChL predictions [37, 38] for the $V_L V_L$ elastic scattering t_{IJ} partial waves, in terms of the renormalized α_4, α_5 couplings, are:

$$\begin{aligned}
t^{(2)}_{00} &= \frac{s}{16\,\pi v^2}, \\
t^{(4)}_{00} &= \frac{s^2}{64\,\pi v^4}\left[\frac{16(11\alpha_5(\mu) + 7\alpha_4(\mu))}{3}\right. \\
&+ \left.\frac{1}{16\,\pi^2}\left(\frac{101 - 50\log(s/\mu^2)}{9} + 4\,i\,\pi\right)\right]. \\
t^{(2)}_{11} &= \frac{s}{96\,\pi v^2}, \\
t^{(4)}_{11} &= \frac{s^2}{96\,\pi v^4}\left[4(a_4(\mu) - 2a_5(\mu)) + \frac{1}{16\,\pi^2}\left(\frac{1}{9} + \frac{i\,\pi}{6}\right)\right]. \\
t^{(2)}_{20} &= \frac{-s}{32\,\pi v^2}, \\
t^{(4)}_{20} &= \frac{s^2}{64\,\pi v^4}\left[\frac{32(\alpha_5(\mu) + 2\alpha_4(\mu))}{3}\right. \\
&+ \left.\frac{1}{16\,\pi^2}\left(\frac{273}{54} - \frac{20\log(s/\mu^2)}{9} + i\,\pi\right)\right].
\end{aligned} \tag{1.59}$$

The resonance mass and width turn out to be a linear combination of these parameters:

$$M_\rho^2 = \frac{v^2}{4(\alpha_4 - 2\alpha_5) + \frac{1}{9(4\pi)^2}}, \Gamma_\rho = \frac{M_\rho^3}{96\pi v^2}, \tag{1.60}$$

where ρ stands for a vector resonance. The mass and width of a scalar resonance denoted σ is

$$M_\sigma^2 = \frac{12v^2}{16(11\alpha_5 + 7\alpha_4) + \frac{101}{3(4\pi)^2}}, \Gamma_\sigma = \frac{M_\sigma^3}{16\pi v^2}. \tag{1.61}$$

In Fig. 1.10 we show the α_4, α_5 parameter spectrum for vector and scalar resonances. Depending on the values of these two parameters, one can obtain, for example, higgs-like scalar resonances and/or technicolor-like vector resonances. There is a region which is theoretically forbidden on the basis of causality arguments.

1.8 Equivalence theorem

At the LHC the possibilities for the Chiral description scenario will be tested for the first time in W and Z interactions at the TeV scale. Longitudinal gauge bosons are basically the Goldstone Bosons and the on-shell amplitudes are almost the same at those energies from what we know as the Equivalence Theorem [39].

$$\mathcal{A}(V_L^a, V_L^b, V_L^c \cdots) \simeq \mathcal{A}(\omega^a, \omega^b, \omega^c \cdots) + O(M_W^2/\sqrt{s}), \tag{1.62}$$

which holds for any spontaneously broken non-Abelian theory. The use of the Equivalence Theorem may seem incompatible with a ChL formalism since it is only valid in the high energy limit. However it is a very good approximation at leading order if we consider energies ~ 1.5 TeV.

1.9 Previous work

1.9.1 Possible LHC sensitivity to VBS

Previous work on the study of order-4 couplings through the scattering of gauge-bosons in reactions such as $qq \rightarrow qqVV \rightarrow VVjj$, with $V = W^{\pm}$ or Z^0 has been published in [5], assuming that there are no heavy resonances at the LHC energy scale. On Fig. 1.11 we see the 90% CL exclusion region in the α_4, α_5 parameter space which they obtained for W^+W^-, $W^{\pm}W^{\pm}$, $W^{\pm}Z$ and ZZ channels for an integrated luminosity of 100fb^{-1}. The work concludes that the LHC bounds on quartic anomalous parameters like α_4, α_5 can be greatly constrained with LHC data. The decay channels studied were $WW \rightarrow l\bar{\nu}\bar{l}\nu$, $W^+Z \rightarrow l\bar{\nu}l\bar{l}$ and $ZZ \rightarrow 4l$.

In reference [11] a similar, more recent study was performed. They find that at 99% CL, a model without a light Higgs boson presents the following bounds (for $100\ \text{fb}^{-1}$)

$$\begin{aligned} -7.7 \times 10^{-3} < \quad \alpha_4 \quad < 15 \times 10^{-3}, \\ -12 \times 10^{-3} < \quad \alpha_5 \quad < 10 \times 10^{-3}. \end{aligned} \tag{1.63}$$

A phenomenology study in [6] searching for "Golden channels" (purely leptonic) considered several unitarization models, including some resonance scenarios. As an example, Fig. 1.12 shows what might be expected for a vector resonance model. It is clear that the signals are very weak.

In this thesis we include a purely leptonic channel study for the $ZZ \rightarrow \nu\nu ll$ final state (see chapter 4), with realistic full simulation of the ATLAS detector, and still find it suitable for discovery probably at $100\ \text{fb}^{-1}$.

1.9.2 Electroweak constraints on the ChL parameters

Bounds on the dimension-4 parameter in the ChL lagrangian compatible with precision electroweak constraints have been obtained in [7]. On Fig. 1.13 the region of allowed values in the α_4, α_5 plane (in gray) as provided by combining indirect bounds and causality constraints is shown. Also depicted, the region below which LHC will not

be able to resolve the coefficients (Black box), given above in Eq. 1.63 according to [11].

The size of the coefficients α_4,α_5, describing the relevant dynamics of VBS at high energy in the effective ChL description can be given bounds by reasonable assumptions based on different models of the strongly interacting sector, as discussed in [7], and model-independent constraints as discussed in this section. In [7] the values are compared with LHC sensitivity and they seem to fall in the region where LHC is not sensible to this type of processes. Therefore, the presence of vector and scalar resonances required by unitarity will be the only plausible characteristic signatures to look for at the LHC.

1.9.3 Previous fast simulation work in ATLAS

Previous work on EChL signals with Padé unitarization exists. Reference [14] presents studies for strong symmetry breaking scenarios at the LHC, in particular vector boson scattering at ATLAS. The author uses the framework of the Electroweak Chiral Lagrangian with Padé unitarisation to generate possible signal scenarios. The signals are simulated with ATLFAST simulation. The work concludes that signals could be observed with an integrated luminosity of 30 fb^{-1}. However, this study did not take into account, in a realistic way, the background $W+$ jets since it was produced with the PYTHIA generator, where $W + n$ jets process is only obtained by parton shower, and not by matrix element calculation. Extra jets are produced by hadronization and fragmentation and the background can not be considered complete. We know now, from the study in this thesis, that this signal would most likely be observed at higher luminosities, probably about 100 fb^{-1}. One of the main reasons is that in the present work a more realistic $W + n$ jets background was used, and it was found to be much more important and complicated than thought before.

Other simulation effort for VBF signals with EChL and Padé unitarization has been done in [8]. Again in this work only ATLFAST simulation was used and the backgrounds not taken into account realistically. On Fig. 1.14 we see the reconstructed WZ system for the decay mode $WZ \rightarrow jjll$. The $Z+$ jets background is included. We conclude in this thesis work that the $Z+$jets background has a very different behavior and is

much more important than appears in these previous works.

Purely leptonic signal and background rates at the LHC for the ZZ, W^+W^-, $W^\pm Z$ and $W^\pm W^\pm$ final states associated with strongly interacting electroweak symmetry breaking have been also studied before [6]. Even if these leptonic channels have quite clean and well resolved final states, the authors conclude that leptonic channels are quite difficult due to their low cross section.

During 2005, a study with full simulated data for the ATLAS detector with WZ and WW resonances was done for the first time. These very preliminary results were shown in the ATLAS meeting at Rome 2005 [40].

Very recently another study of VB resonances with leptonic final states [41] also concludes that observation of these signals will require a few hundred fb^{-1}.

1.10 ChL as a way to look at VBS with ATLAS

We know that WZ pairs are going to be abundantly produced at the LHC, due to the high energy of the collision, with a cross section of about 26 pb. As we stated before, if some strongly-interacting symmetry breaking sector is realized in nature, we have a very good chance of seeing resonances at LHC energies. The effective approach of the ChL description plus the IAM method that allows one to regularize the cross section at high energy, seems to be a good underlying theory-independent way of looking at such a scenario. We may not be able to tell, in an early stage, what such resonances mean in terms of a fundamental description, but the considerable amount of work of preparing the path for identification of such processes can be done through this bottom-up approach and the full ATLAS-detector simulation studies that will be presented in the following chapter.

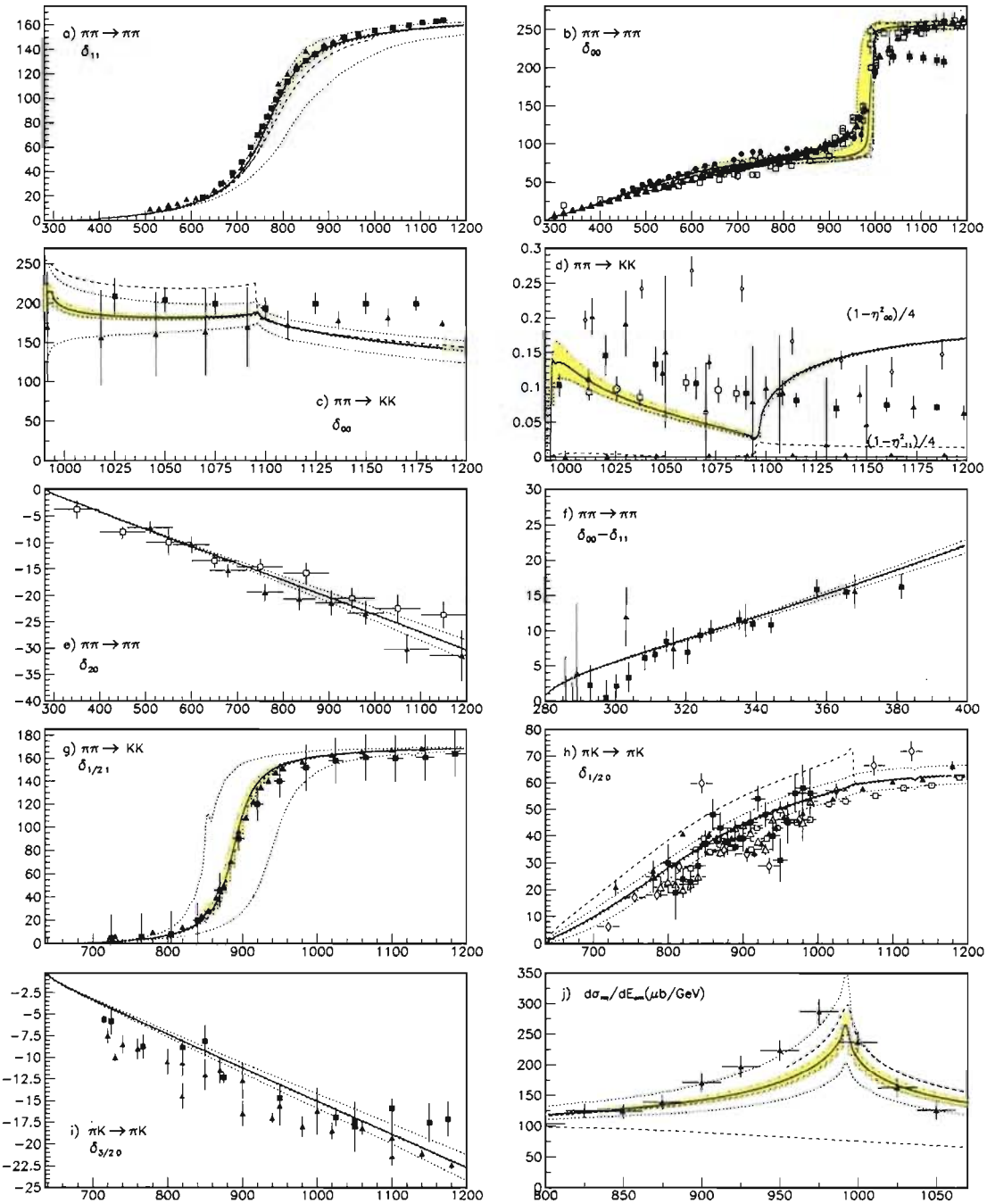

Figure 1.9: The curves represent the result of the coupled channel IAM fit to meson-meson scattering observables. The shaded area covers only the uncertainty due to the statistical errors in the parameters obtained from a fit implementation (MINUIT). The area between dotted lines corresponds to the error bands including in the parameters the systematic error added to the data. On the x axis the units are MeV. On Figures a,b,c,e,f,g,h, and i, the y axis is a phase (or phase difference) in units of degrees. On Figure d the y axis has units of inelasticity and on figure j the units in the y axis are μb/GeV. This plots have been taken from [3].

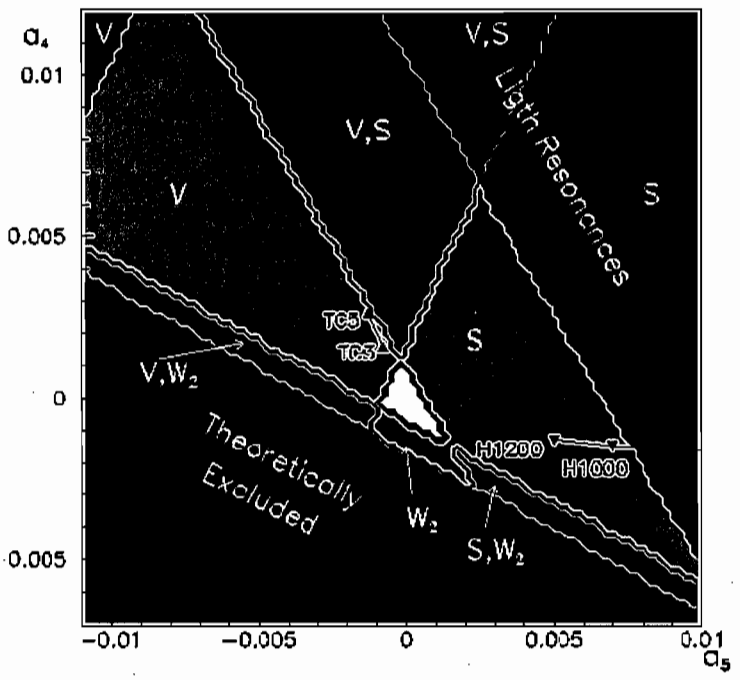

Figure 1.10: Resonance spectrum of the strong SBS. Vector resonances are produced in the area marked with V, S stands for Scalar resonances. This plot has been taken from [4].

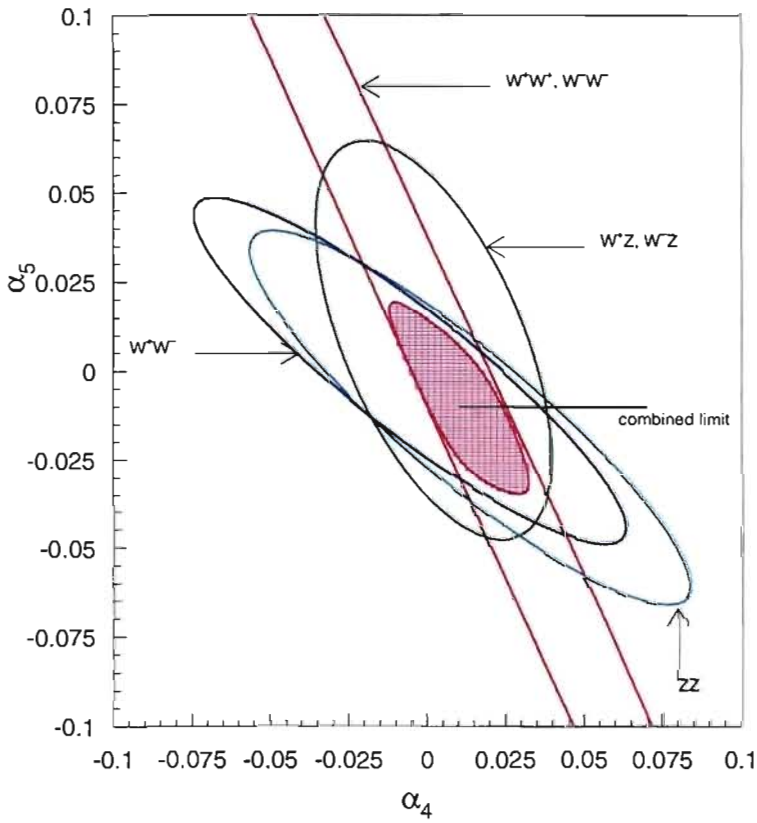

Figure 1.11: 90% CL exclusion region in the α_4, α_5 parameter space obtained for W^+W^-, $W^\pm W^\pm$, $W_\pm Z$ and ZZ channels for integrated luminosity of 100fb^{-1} [5].

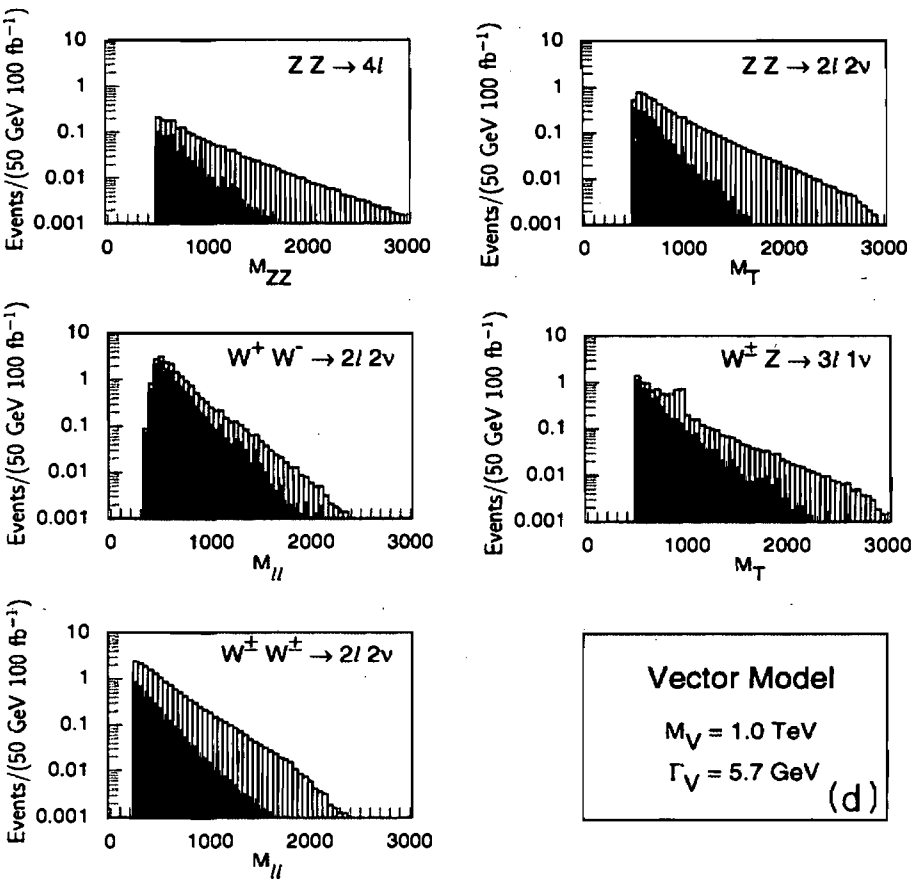

Figure 1.12: A chirally coupled vector with mass 1 TeV, $\Gamma = 5.7$ GeV [6]. The mass variable of the x axis is in units of GeV and the bin size is 50 GeV.

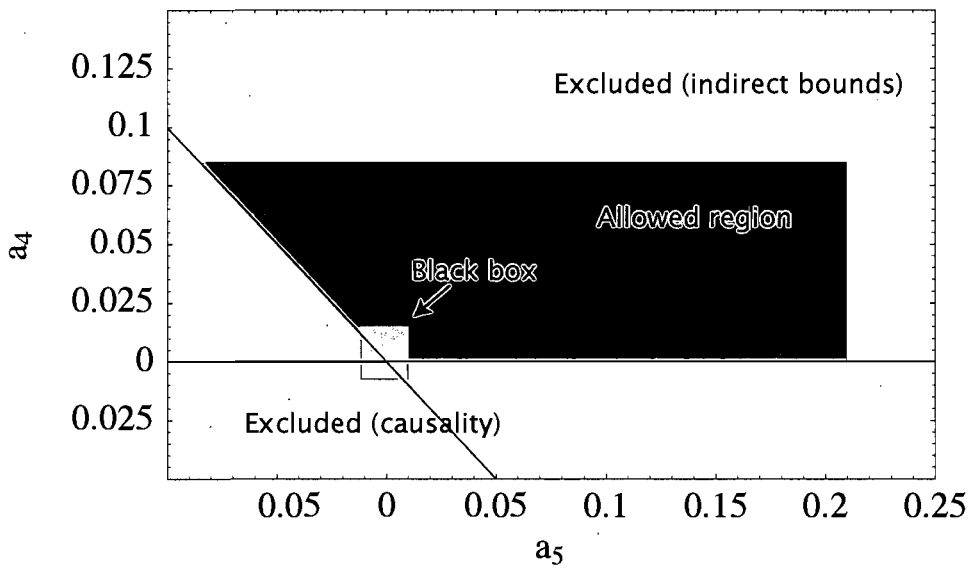

Figure 1.13: Region allowed by electroweak precision measurements for α_4, α_5 parameters [7] (in gray). Also causality constraints are shown. And depicted, the region below which LHC will not be able to resolve the coefficients (Black box).

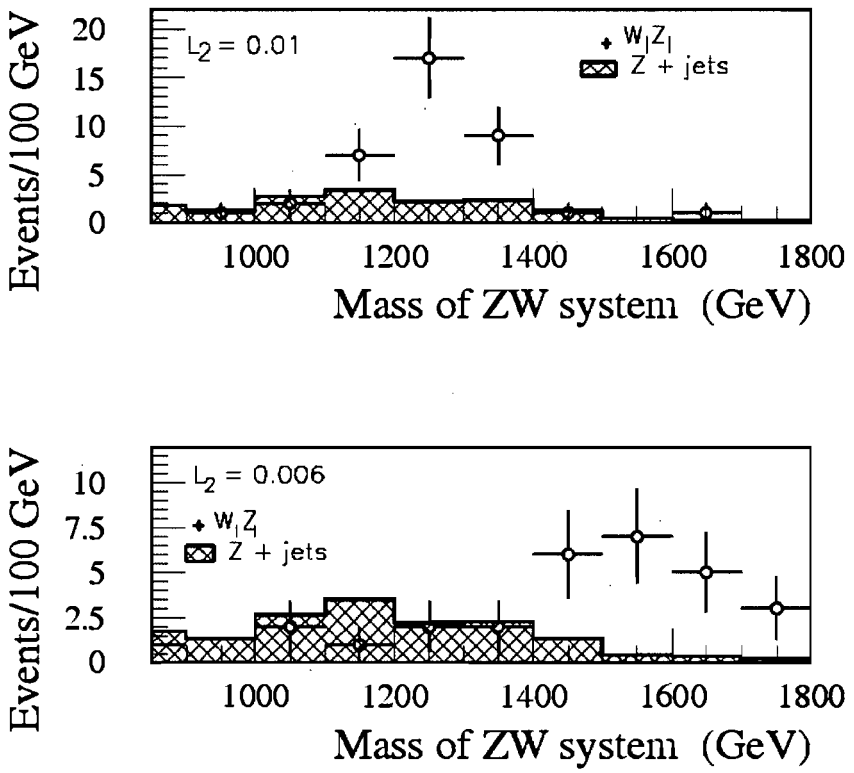

Figure 1.14: Mass distribution for the reconstruction of the WZ system for the decay mode $WZ \rightarrow jjll$. [8].

CHAPTER 2

THE ATLAS DETECTOR

The LHC (Large Hadron Collider), scheduled to start running at the end of fall 2008, is a 27 km superconductor ring, sitting at 100 meters underground, accelerating protons up to an energy of 7 TeV and producing proton-proton collisions with an energy at the center of mass of 14 TeV. The ATLAS (A Toroidal LHC ApparatuS) detector is one of the four big detectors around the ring designed to study the products of the collisions at the LHC. In this chapter, I give a very brief description of the ATLAS detector main subsystems to illustrate the detector functionality. ATLAS can be divided in its four main parts, namely, the inner detector, the calorimetry, the muon spectrometer and the magnet system. The joint performance of the detector subsystems ensure particle detection capabilities necessary to achieve the goals of the experiment. ATLAS has been designed to profit from the full potential of LHC, being sensitive to processes already known and expected from the SM, experimentally verified in former experiments (like LEP[1] and the Tevatron[2]) in order to extend the measurements to higher energies. But more importantly, thanks to the very high energy of the collisions and a nominal luminosity of $10^{34}\,\mathrm{cm}^{-2}\mathrm{s}^{-1}$, we should be in a good position to search for signals beyond the SM (BSM) in the TeV range, where we expect that the SM may begin to fail.

The other detectors in the LHC ring are: CMS (Compact Muon Solenoid), LHCb (Large Hadron Collider b-experiment) and ALICE (A Large Ion Collider Experiment). Like ATLAS, CMS is a general purpose detector, and is considered to have approximately the same capabilities as ATLAS, even if the detector subsystems are substantially different and the performance has different nominal (but still comparable) values. LHCb has been designed to study b-physics and ALICE is ready for heavy ion collisions. LHC will not only produce proton-proton collisions, but also proton-ion and ion-ion collisions in the years to come.

[1] Large Electron Positron collider. Former accelerator at CERN.
[2] At Fermilab, USA.

Along with the detector-hardware setup comes the entire software implementation of the experiment. From the lowest to the highest level (in terms of hardware abstraction) we have: the firmware embedded in the front-end hardware (RODs, Read Out Drivers) of the detector subsystems, the firmware in the Level-1 Trigger machine, the software in the Level-2 and Event Filter (EF[3]) and finally the so called *offline software* which is itself constituted of several different components. This last component is the result of a vast effort which brings software technology to the limit of present possibilities. It aims to build the tools necessary for data storage, simulation, reconstruction and manipulation, connecting to the analysis developed by the user to study the data and finally produce physics results. The effort is world-wide and it must be remarked that this thesis work relies heavily on the development and use of these tools. The author of this thesis actively contributed to this software effort but nearly all details of the software implementation and testing are beyond the scope of this thesis work due to its strongly software-oriented nature. However I will describe in some detail the trigger and analysis parts. I have produced all the figures in this chapter using simulated data of our signals, and the v-atlas software [42]. Complete and up-to-date descriptions of the detectors elements can be found in the ATLAS Detector Paper [43].

An ATLAS detector subsystem designed to measure the radiation environment in the ATLAS cavern is described in great detail in this chapter due to the participation of the author in the calibration, installation and on-line software for the ATLAS-MPX detector.

2.1 Inner detector

The purpose of the inner detector is to measure with precision charged particle tracks in order to allow reconstruction of decay vertexes of short lived particles and obtain the momentum of leptons and charged pions. It is composed of three main components: The pixel detector, the SCT (Silicon Tracker) and the TRT (Transition Radiation Tracker).

The inner detector surrounds the beam pipe with a diameter of 5 cm; and extends to

[3]Actually the Level-3 trigger.

the wall of a solenoidal magnet providing a field of 2 T. It has a radius of 115 cm and a length $|z| = 345$ cm. The main specifications of the inner detector, as a whole, for high luminosity, are:

- Pseudo-rapidity range coverage $|\eta| < 2.5$
- Momentum resolution of $\Delta p_T/p_T < 30\%$ at $p_T = 500$ GeV for $|\eta| < 2$. The resolution worsens as we approach $|\eta| = 2.5$ down to about 50%.
- Tracking efficiency of $> 95\%$ over the full coverage for isolated tracks with $p_T > 5$ GeV.

The inner detector combines the high precision tracking of pixel and strip detectors with straw tubes of the TRT which have a lower spatial resolution. The pixel detector consists of three barrel layers and five end-cap disks on each side. They are closest to the beam pipe, giving a tracking precision of 12 μm in $R\phi$ and 70 μm in z. Due to their coverage they should provide a few points per track with $|\eta| < 2.5$ as input to the pattern recognition algorithms. In addition, the pixel detector is the most radiation-hard system of ATLAS since it will be exposed to high fluxes of particles.

The strip detectors (4 barrel layers and 9 end-cap wheels on each side) are used for larger-area precision tracking. In the barrel region they are silicon detectors while in the forward region, which is subjected to a higher fluence, GaAs (gallium arsenide) detectors are used due to their higher radiation tolerance. This system, known as the Semi-Conductor Tracker (SCT), provides also a few hits to the tracking software. Finally the straw tubes are used at larger radii where the track density is relatively low. On a third stage, the straw tubes receive the X-Rays coming from transition radiation produced a lot more by electrons than by protons (or any other relatively heavy hadron) when crossing an interface between two different materials. The material interfaces, where the X-Ray shower produced by highly relativistic particles, are placed between the straws in great number. The straw tubes, full of Xenon and CO2 (as signal stabilizer), amplify the signal from the X-Rays, a technique that allows electron identification over heavy hadrons like pions or protons. This detector is known as the TRT. The TRT is necessary because at

very high energy most of the charged particles look very similar and it is impossible to tell them apart. For instance, an ultra-relativistic pion and electron, both having an energy of 10 GeV will look exactly the same in the tracker and we need to differentiate them. The quantity $\gamma = E/m_0$, where E is the energy of the particle and m_0 is its rest mass, allows for their identification since there is a difference of 3 orders of magnitude in their γ value at this energy. The identification is done in the TRT by measuring the X-Ray cascade and measuring the energy depositions in the tubes above a given threshold. In the ATLAS TRT system when the electron identification efficiency is of about 90% [44], the measured pion efficiency is about 1.2%, i.e. a great rejection factor is achieved. The conditions in this particular case are pions of 20 GeV and a magnetic field of 0.8 T in the barrel part of the TRT detector.

In summary, as the particle moves away from the collision point in the center of the detector, the tracking precision diminishes. The pixel detector is the most precise. The SCT and TRT still give a good precision (16 μm, 170 μm in $R\phi$ respectively) and will resist better the extreme particle and energy flux environment. In Fig.2.1 a model of the inner detector geometry is shown: the pixel detector in sea-green with some particle tracks (in dark blue). The pixel layers are removed in the center to show the tracks. The SCT detector is shown with part of the silicon layers removed to show the internal structure (with some tracks shown in white). Finally we can see the TRT detector, with details on its fibre radiator structure (straws in purple) and its tracks shown in red. Note the structure of the three tracks (dark blue, white and red) suggested by the picture. They are in fact the paths of two very energetic central jets, beautifully tracked by the inner detector system.

2.2 Calorimetry

The ATLAS Calorimetry system consists of (i) a barrel cryostat around the inner detector cavity which contains the barrel part of the electromagnetic calorimeter and the solenoidal coil which produces the magnetic field for the inner detector, (ii) two end-cap cryostats that enclose the electromagnetic (e.m.) and hadronic end-cap calorimeters

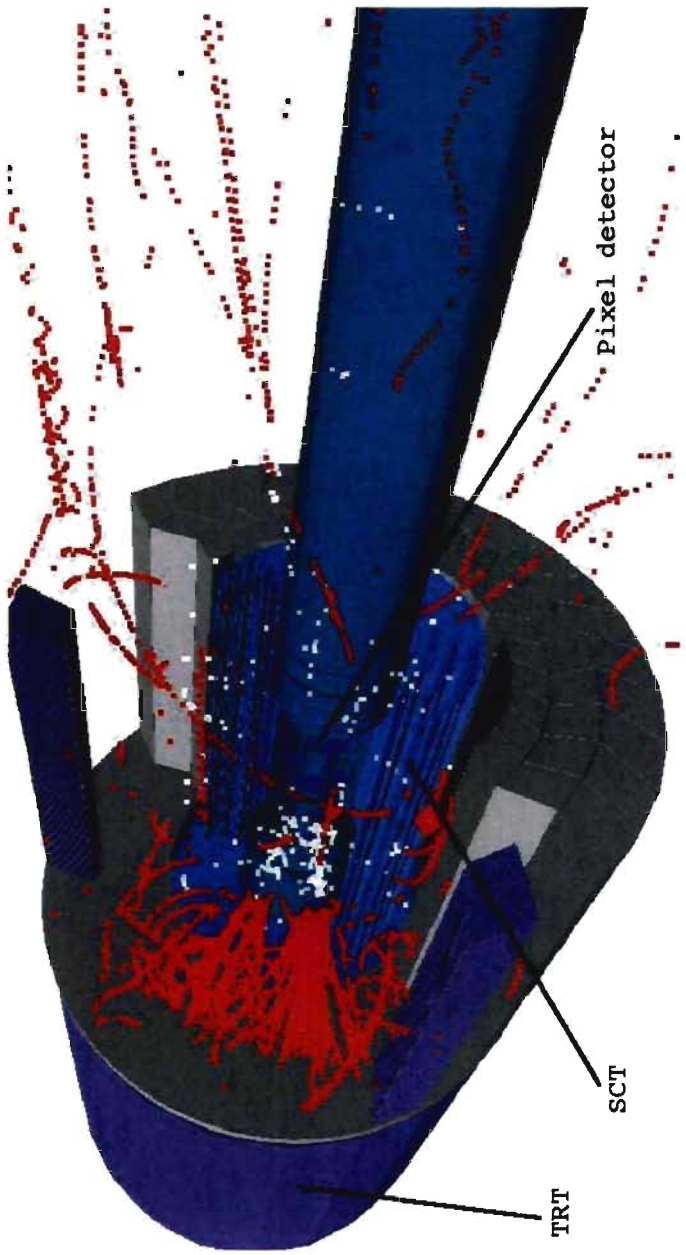

Figure 2.1: Virtual geometry model of the inner detector. It is composed of the inner detector (in sea-green), the SCT (sillicon tracker in blue) and the TRT (transition radiation tracker in purple). In blue, white and red the tracks of charged particles in the pixel detector, SCT and TRT respectively. The event used to simulate the response of the inner detector in this figure corresponds to a single event of $pp \rightarrow WZ \rightarrow jjll$.

as well as the forward calorimeter, (iii) the barrel and (iv) the extended barrel hadronic calorimeter, contained in an outer cylinder after the e.m. calorimeters.

The e.m. part of the calorimeter has been built with lead/liquid argon sampling technology. The absorbers consist of stainless steel covered lead plates with accordion shape with increasing pitch to keep the sampling fraction constant, i.e. more bent as we move away from the collision point (see Fig.2.2). The gap between two lead absorbers is filled with liquid argon and in the center we find a three layer polymide/copper electrode that is used as a cathode. The copper pads on the outer faces are set at high voltage and the absorbers are grounded. The functioning principle is as usual. The ionizing particle goes through the liquid argon ionizing the medium, and hence, due to the electric field, the ions produced drift towards the absorber and electrons towards the anode. What makes the Lead/Liquid Argon technology special for this particular case is the performance requirements. Materials and dimensions are such that a large dynamic range (from 50 MeV to 3 TeV), low noise, dead timeless operation and a huge sampling frequency can be achieved.

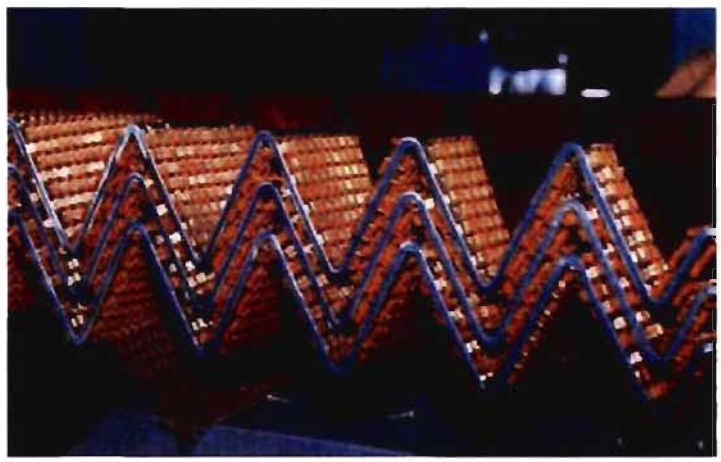

Figure 2.2: The accordion structure of the e.m. calorimeter. Honeycomb spaces position the electrodes between the lead absorber plates.

The e.m. barrel section of the calorimeter goes within the $|\eta|$ region < 1.4 and the end-caps $1.4 < |\eta| < 3.2$. The segmentation of the calorimeter is $\Delta\eta \times \Delta\phi \simeq 0.025 \times 0.025$ over most of the rapidity coverage. The hadronic section of the calorimeter

uses iron absorbers with scintillator plates. The scintillators are distributed parallel to the beam axis with a read-out system composed of wavelength-shifting fibres coupled radially to the scintillators and grouped to form readout cells with a segmentation $\Delta\eta \times \Delta\phi \simeq 0.1 \times 0.1$ [45]. At higher rapidity where higher radiation hardness is required, the hadronic calorimeter uses liquid argon and has a coverage $3.2 < \eta < 4.9$. All the calorimetry system has been designed to allow operation for more than ten years at high luminosity.

Physics goals such as the search for the decay of a Higgs boson into photons or into final states involving leptons, or the detection of new gauge bosons, like W' or Z' have dictated the design of the ATLAS calorimetry. New physics imposes tight requirements in terms of acceptance, dynamic range, particle tagging (low miss-tag rates) and energy resolution. Higgs signals like $H \rightarrow ZZ^* \rightarrow 4e$, require good electron reconstruction starting from energies $E_T \simeq 5$ GeV. The upper limit is given by processes like $Z' \rightarrow ee$ were the reconstructed mass could go up to 5 TeV. From such limiting cases, we find that a good perfomance for e.m. shower energies should cover the range between a few GeV and 5 TeV. Regarding the acceptance, according to M.C. studies, the combined coverage $|\eta| < 5$ ($|\eta| < 2.5$ for tracking) provides high-efficiency reconstruction of the signals requested. The dynamic range of the calorimetry system varies from 1.5 to 3 TeV per readout cell for the upper limit masses and from 35 to 100 MeV corresponding to the electronic noise levels.

In the case of the hadronic calorimeter, we are interested in very efficient jet identification with a good measurement of its energy and direction. It is essential also for the measurement of the total missing transverse energy E_T^{miss}. It complements the e.m. calorimetry by measuring leakage and isolation. Jet energy and subsequently E_T^{miss} measurements are limited by several effects. The jet energy can be calculated in many ways; there exist several algorithms for it, but in general terms we basically add up all the energy deposited in a cone of opening angle $\Delta R = \sqrt{\Delta^2\eta + \Delta^2\phi}$ around the jet axis. Such measurement is subject to a number of uncertainties. At LHC energies, pile-up from minimum-bias events becomes very important. The presence of 18 minimum-bias events gives, for example, an r.m.s of about 5 GeV for the E_T measure in a cone of

opening angle $\Delta R = 0.5$ in the barrel region. For E_T^{miss} reconstruction pile-up events produce an important background at low energy, below ~ 50 GeV.

Higgs search signals like $H \rightarrow WW \rightarrow l\nu jj$ where a vector boson decays into two jets requires very good segmentation in the calorimeter. Other beyond standard model signals, such as those studied in this thesis, where a vector resonance decays into two vector bosons $\rho \rightarrow WZ \rightarrow jjll$, have the exact same type of hadronic final state. Such signals can only be properly reconstructed with good efficiency and large background rejection in a well-segmented calorimeter. According to simulated data, the separation between jet pairs, for the Higgs channel, is approximately $\Delta R = 0.4$. A segmentation of at least $\Delta\eta \times \Delta\phi = 0.1 \times 0.1$ is needed to achieve good efficiency for reconstruction of the two jets. At high rapidity the segmentation does not need to be as good since the lateral energy deposition represents a large pseudorapidity variation. Proper forward jet tagging can be done with a segmentation of $\Delta\eta \times \Delta\phi = 0.2 \times 0.2$.

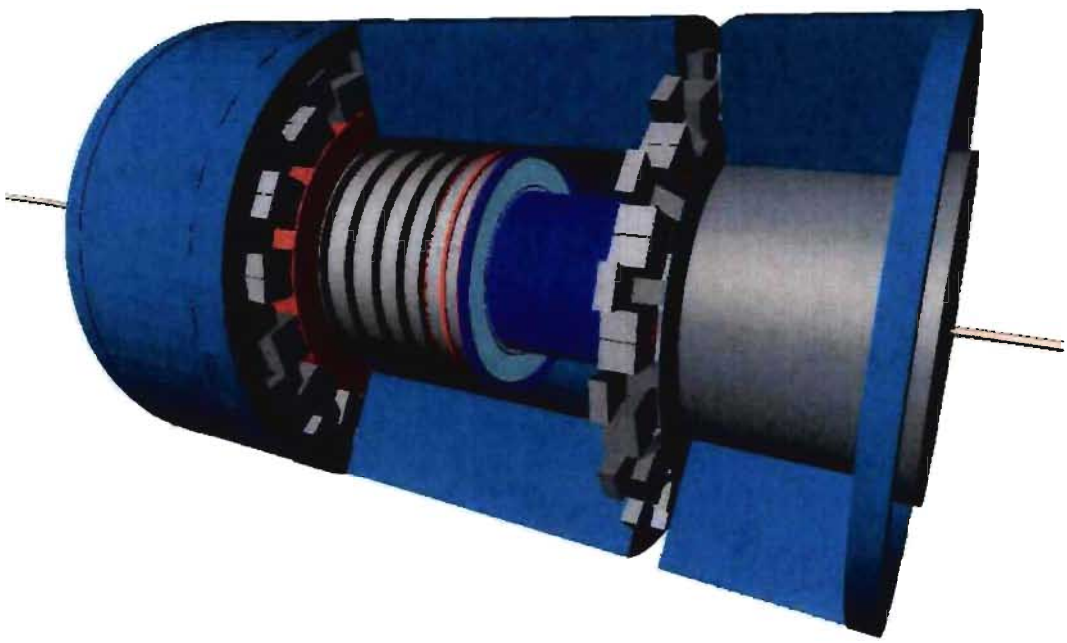

Figure 2.3: The calorimeter system is composed of a barrel cylinder (inner em in purple and hadronic in green), and end-caps (inner em in gray and hadronic in green).

2.3 Muon spectrometer

Only a small fraction of the collisions produced at the LHC will be interesting for SM physics and probably even fewer for physics BSM. Those detector signals that include isolated leptonic decays, in particular those with muons, will be important since they are expected to be cleaner than those where hadronic activity is present. Muon identification is possible even when the muon is present close to hadronic activity.

The muon system of the ATLAS detector provides a reliable, high resolution, performance over a p_T range from 5 GeV to $\geq$ 1000 GeV. It is located at the outer diameter of the detector (occupying a very large volume) since muons are minimum ionizing and do not stop in the calorimeter. The momentum resolution is about $\Delta p_T/p_T \simeq 2 \times 10^{-2}$ at 100 GeV, and drifts to $\Delta p_T/p_T \simeq 10^{-1}$ for 1 TeV with some dependence on η. At low energy, good resolution is required for the B physics programme, for muon momentum down to $p_T \sim 5$ GeV. The reconstruction of Z bosons decaying to muons can be extremely clean. Simulations have shown that we can reconstruct the Z mass with very good precision, of up to ~ 3 GeV [46].

The muon spectrometer is composed of:

- The toroidal magnet system, (presented in subsection 2.3.1) whose field shape varies as a function of η and ϕ with a significant drop in the transition between the barrel and endcaps ($1.4 < |\eta| < 1.6$). Precision detectors are located where most of the magnetic field deflection occurs. The precision is typically better than 100 μm giving a very accurate measurement in the η-coordinate and somewhat poorer for ϕ.

- Resistive plates and thin gap chambers provide rough measurement for both η and ϕ coordinates.

- A dedicated trigger system for the muon spectrometer is one of the particular characteristics of this detector subsystem. The trigger chambers are available in the pseudorapidity range $|\eta| < 2.7$, and this coverage is considered sufficient for the most part of the physics program.

The muon chamber planes (as shown in purple on Fig.2.4) are attached to the toroid holders structure. There are three layers of chambers. One very close to the central barrel (where the calorimetry system is installed), another one close to the internal bounds of the toroidal magnetic system and an outer layer of muon chambers right after the magnet system. In the forward direction the chambers are placed at the front and back faces of the toroid cryostats (in yellow and green on Fig.2.4). For high energy muons, combining the track information from the SCT and muon spectrometer improves significantly the resolution since the solenoidal field in the central detector is higher than the toroidal magnetic field.

2.3.1 The Magnet System

There are two magnet systems in the ATLAS detector, the first one is a superconducting magnet positioned in front of the electromagnetic calorimeter integrated into the vacuum vessel of the LAr cryostat producing a nominal magnetic field of 2 T. Its inner diameter is 2.46m, its outer diameter is 2.63m and its axial length 5.3m. The second magnet system, much bigger in volume, is for the muon spectrometer. It is an air-core toroid of 26 m length and an outer diameter of 19.5 m. The total bending power, integrated between the first and last muon chambers, increases from about 3 Tm at $\eta = 0$ to about 8 Tm at $|\eta| = 2.8$. The whole magnetic system has a total weight of 1400 tons. On Fig. 2.5 a virtual geometry model of the air-core toroid with their anchors to the cavern floor is presented. Notice the disposition of the toroids; they produce a circular magnetic field (enclosing the barrel components of the detector) that would bend the trajectory of a muon, coming out in the transverse plane, towards the beam direction.

2.4 Data Acquisition and High Level Trigger (HLT).

The trigger system for the ATLAS experiment is in charge of the online selection of interesting events registered by the detector. By online, I mean in *real-time*, in the sense that the rate at which the trigger system can identify important events has to be equal to or greater than the actual throughput rate at which the detector works. Nevertheless

Figure 2.4: The muon spectrometer system composed by three barrel-shape layers of muon chambers (in purple) plus the chambers disposed for the forward region (in yellow and green).

the trigger system is not a real-time machine itself. Different mechanisms to achieve

Figure 2.5: External magnet system composed of eight toroids of 26 meters length with an outer diameter of 19.5 m. It is by far the biggest magnet system ever built. The components in magenta and green are the outer section of the inner barrel containing the calorimeters and the inner detector, included in this figure just to give an idea of the size of the system.

such a functionality have been developed by the Trigger-Infrastructure group in ATLAS. Out of the millions of events registered by the detector subsystems, the trigger has to be able to select a few, based on a very efficient search for interesting objects, tagged as jets, electrons, muons or any other interesting object or combination of objects satisfying certain conditions in an event.

An overall scheme of the Data Acquisition (DAQ) and Trigger system of the ATLAS experiment is shown in Fig. 2.6. The DAQ system (on the right side) gathers the data from the 400 read-out drivers (ROD) of the detector subsystems. The RODs are part of the DAQ front-end electronics and have the job of delivering digital data streams con-

taining the response of each part of the detector. The system will be producing data at an outstanding rate of $\sim$ 1 PB/s (PB: Petabyte = 10^{15} bytes) which has to be dramatically reduced for two important reasons. First of all, such a quantity of data cannot be stored at that rate; the technology simply does not exist, and secondly most of that data is not really useful. The trigger system solves this problem by implementing three trigger levels. The different levels of the trigger system are separated and independent (in the sense of implementation). The first-level trigger (L1) encounters an event rate of 40 MHz, and using custom electronics (with embedded firmware) has to be able to reduce the rate to $\sim$ 100kHz. The second-level (L2) is purely software based, and brings the rate down to a few kHz. And finally the third level, called Event Filter (EF) and also software based, needs to end up with a final rate of 200 Hz, which we can actually store and deliver for off-line analysis. The L2 and EF parts of the Trigger together are called the High Level Trigger (HLT) and are grouped due to their similar infrastructure and event selection software design. On the left side of Fig. 2.6 (at the very bottom) we see that at the output of the EF the output event rate has been reduced to $\sim$ 200 Hz, which corresponds to a rate of storage of around 300 MB/s.

The trigger conditions are defined in a *Trigger Menu*, a list of possible signatures that we want to see in the detector. A trigger menu takes the trigger as a whole, taking into account all the trigger levels working as a unit. One signature in the menu can be built with one or more possible trigger selections. For example, if we are looking for events where we require a single jet, in the $|\eta| < 3.2$ region with a transverse energy higher than 120 GeV, we configure the jet trigger to have such a threshold. Single and multi-jet trigger signatures will identify useful events for various Standard Model QCD measurements. We can also create more complex items that are made of a combination of several trigger selections. For example a dijet of a given energy plus two electrons with an energy higher than 60 GeV, plus jets with energy higher than 200 GeV in the forward calorimeters. This combination would be for example the trigger signature that an event should satisfy in the case of VBF signals.

In the following subsections I will describe the connection between the three different trigger levels and its functionality in some detail. As a working example, I shall take the

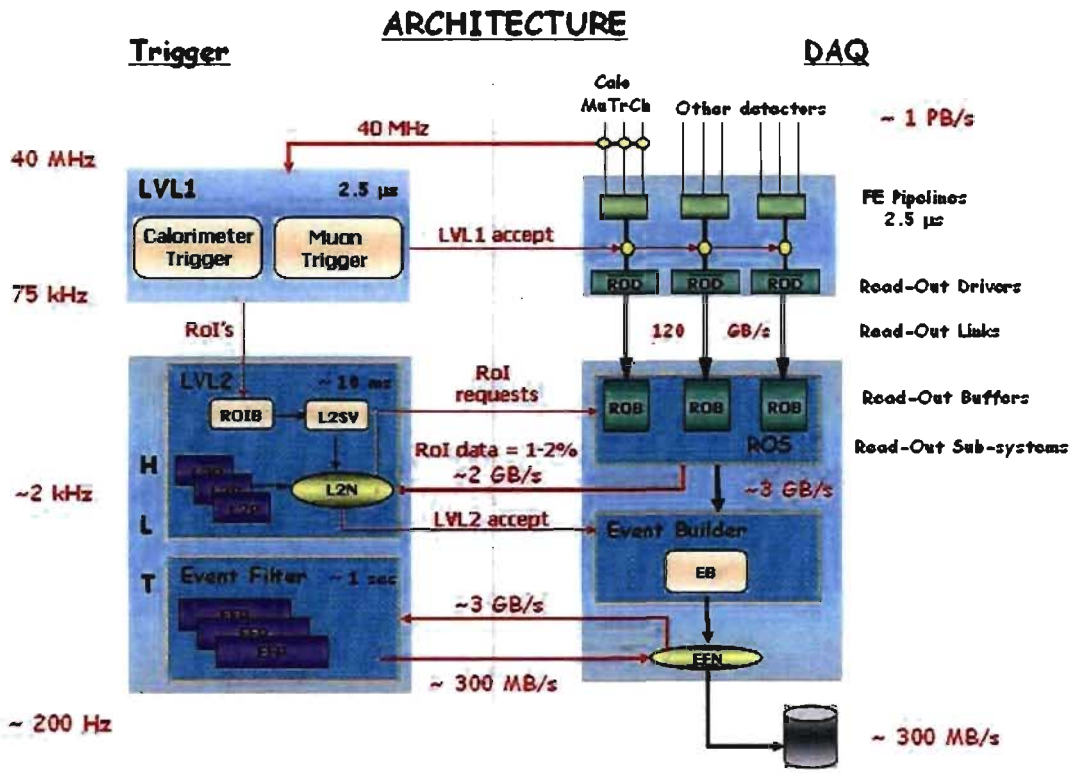

Figure 2.6: ATLAS Data Acquisition System (DAQ) and Trigger overall infrastructure.

jet trigger chain (called Jet Slice). This is a very important trigger. Indeed selection of events relies in part on the ability of the trigger to efficiently identify hadronic jets in an event since many of the SM and BSM signals we want to look for with ATLAS rely on hadronic activity.

2.4.1 The Level-1 trigger

The purpose of the Level-1 system, shown in Fig. 2.6 is to analyze calorimeter and muon detector data with a raw granularity, due to the very tight time constraint it has to deal with, and to identify the so-called *Regions-of-Interest* (RoIs) [47]. RoIs are basically *hot-spots* in the detector where the search for concrete objects can be started. The RoI feeds the actual L2 algorithms which then start analyzing the information in the vicinity of the position defined by this object.

The L1 jet trigger algorithm takes objects from the calorimeter called *trigger towers* with a granularity of $\sim 0.1 \times 0.1$ in $\eta \times \phi$ space. The trigger towers, composed of towers of cells from the calorimeter, are digitized by the L1 trigger which also associates them with a bunch crossing and performs pedestal subtraction. The pedestals are measured with data taken in the absence of beam. At the same time, a noise-suppression threshold and calibration are applied. The jet elements are built from the sum of 2×2 (a volume made up of two cell layers in the *phi* coordinate and two in η) trigger towers in the e.m. calorimeter added to 2×2 trigger towers in the hadronic calorimeter. It gives a granularity of 0.2×0.2. In order to take a decision, the L1 trigger uses a sliding window of programmable size that could be 2×2, 3×3 or 4×4 calorimeter elements. A jet is then reconstructed if the total transverse energy (e.m. plus hadronic) in the window selected is above a given threshold. To avoid background from overlapping jets, the transverse energy of a cluster, defined as a region spanned by 2×2 jet elements, has to constitute a local maximum within a radius of 0.4 in the η, ϕ plane. For the moment the jet algorithm searches for jets within the region of $|\eta| < 3.2$. In the case of the forward calorimeter ($|\eta| > 3.2$) the towers have a coarser granularity of $\sim 0.4 \times 0.4$. In the near future the forward jet part will be also turned on extending the jet algorithm reach up to the very forward values of η.

Knowing the efficiency of the L1 trigger (or any other trigger level) is crucial if we want to evaluate the cross section of a given physical process. The performance has been determined by different trigger groups for different slices (in the same way we defined before the jet slice, there is an e.m. slice, E_T miss slice, etc.). In particular, for the jet-slice, the performance was studied using simulated data of hadronic objects that span the whole E_T jet spectrum relevant for jet identification. An observable called *transverse energy scale*, defined as the ratio of the measured transverse energy to the corresponding particle truth (from Monte Carlo) jet E_T, is used as a measure of the quality of the calibration of the L1 trigger. In order to calculate such an observable we need to be able to match truth jets and the jets found by the trigger system. This match procedure is done using the distance between the two objects defined as $\Delta R = \sqrt{(\eta_{L1} - \eta_{\text{TPJ(0.4)}}) + (\phi_{L1} - \phi_{\text{TPJ(0.4)}})}$ (where TPJ(0.4) stands for Truth-

ParticleJet reconstructed with Cone size 0.4. See appendix I.). When ΔR is smaller than a certain threshold, the objects are said to be close enough to be considered as a match.

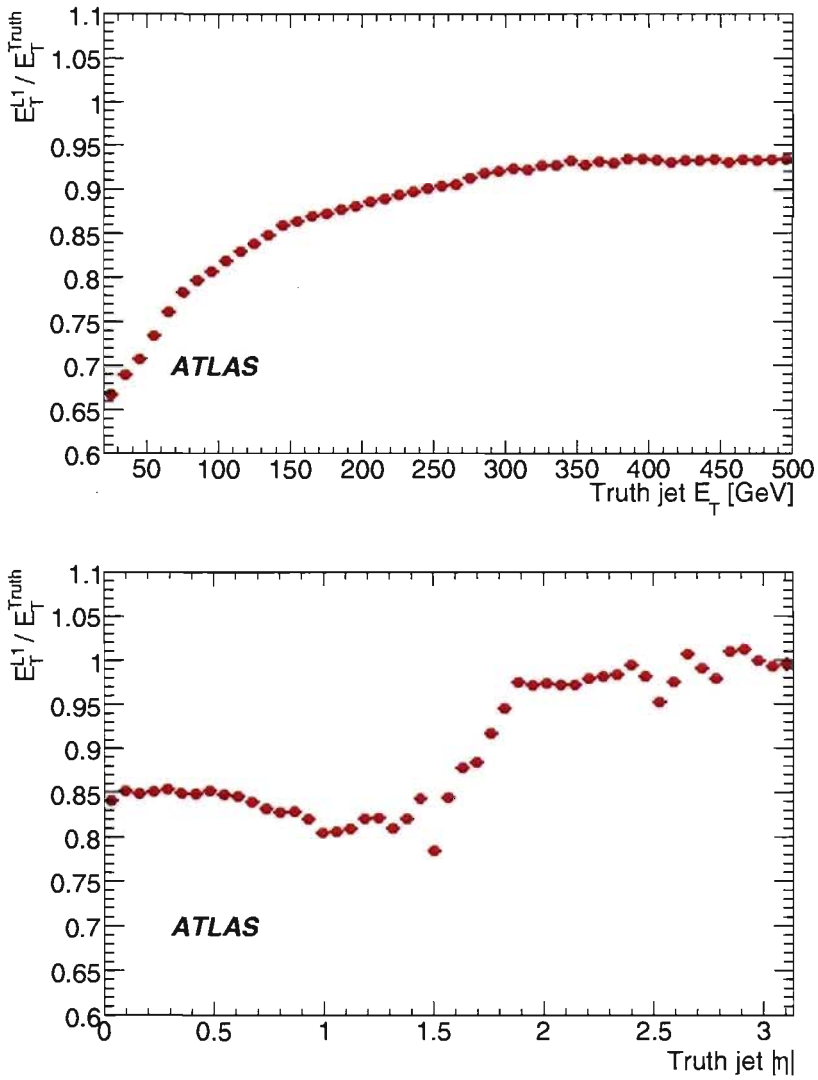

Figure 2.7: The L1 jet transverse energy scale as function of truth jet transverse energy (a) and pseudo-rapidity (b). Taken from [9].

On Fig. 2.7 we see that as a function of the truth jet E_T, the energy scale at L1 varies from about 65% to $\sim$ 95%. This means that we are not able to collect the whole energy of the jets in the L1 trigger, especially for the low energy range. One of the

main reasons is that at low energy, the energy deposited by a particle in the clusters that belong to a given trigger tower can be very small, and a high proportion of towers can fail the application of the noise suppression threshold, contrary to what happens at higher energy. It is important to remark here that the performance values presented on this plots corresponds to an ATLAS software release dated around August 2008. Since then, a lot of improvement has been made in the algorithms and analysis software in general. On Fig. 2.8 we can see the overall efficiency as a function of the offline jet E_T, meaning the E_T obtained from whole calorimeter information by the offline jet reconstruction algorithms. See appendix I for details. We can see that the turn-on of the efficiency curves, happens around the threshold values and rapidly reaches 1 as the energy of the reconstructed jet surpasses the threshold, as it is expected.

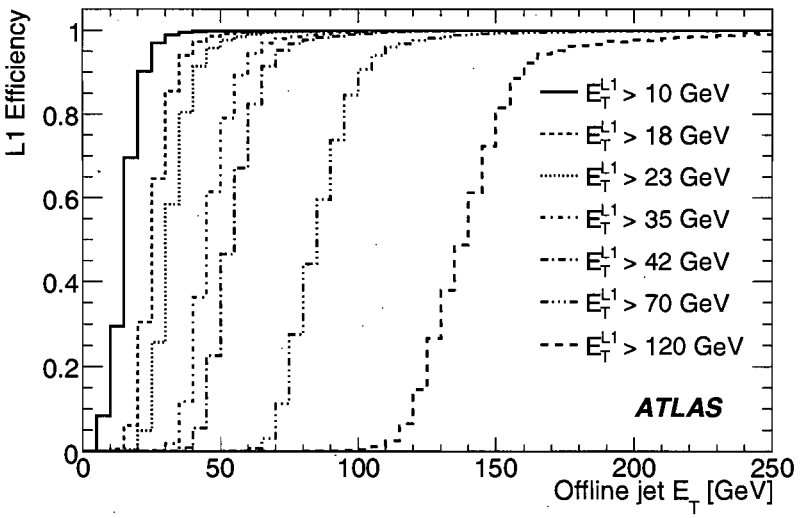

Figure 2.8: L1 jet trigger efficiency as function of the reconstructed jet E_T for different L1 energy thresholds. Taken from [9].

The final result of a L1 trigger, regardless of its nature, i.e: jet, egamma (dedicated to e.m. objects), etc, is the RoI that is given as input to the HLT algorithms. The coordinates of this RoI are updated and refined by the HLT. There are two types of HLT algorithms: The "Feature Extraction algorithms" (FEX) and the "Hypothesis algorithms". In brief the Feature Extraction performs the data extraction and unpacking of the corresponding

detector subsystem required by the HLT algorithm, which is usually limited to a relatively small region around the RoI, and calculates all kind of physics observables used afterwards to take a trigger decision. These algorithms consume most of the available time. The Hypothesis algorithms consider the physics information calculated by the FEX algorithms to validate a given hypothesis if certain predetermined conditions are satisfied, such as a given combination of threshold values on a set of observables.

The separation between FEX and hypothesis algorithms is made due to performance considerations. The data retrieved by a single FEX algorithm can be used to feed several hypothesis algorithms. Separating the two parts, we often avoid multiple data access and unpacking as it turns out to be one of the most time-consuming tasks that the FEX algorithms perform.

2.5 The High Level Trigger

The High Level Trigger (HLT) is the combination of the L2 and EF parts of the trigger. On Fig. 2.9 we can see a summary of the trigger logic for the case of the jet trigger. It works similarly for the other trigger slices. Once the L1 trigger informs the L2 trigger of the presence of an RoI, the L2 trigger attempts to run the rough jet reconstruction described on section 2.5.1 and takes a decision through the hypothesis algorithm. A new jet of coordinates η_{L2} and ϕ_{L2}, usually not too far from the original position of the L1 RoI, is the input of the EF algorithm. The EF algorithm unpacks the data necessary and builds the Towers that are going to be input to the jet reconstruction algorithms (see appendix I.). Finally it reconstructs a Jet with limited calorimeter information and calls the Hypothesis to determine if the jet satisfies a given trigger menu.

2.5.1 The Level-2 trigger

The L2 trigger is a software-based system which runs on a cluster of a few thousand CPU-cores using a multi-thread paradigm in order to reach the desired performance. I will not get into the details of the trigger infrastructure since this subject is heavily software oriented and it is beyond the scope of this thesis work, although I have personally

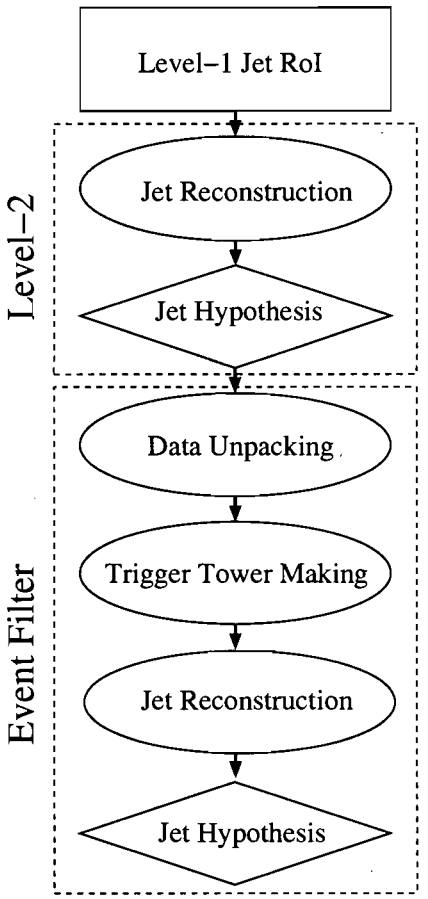

Figure 2.9: The sequence of algorithms for the particular case of Jet objects starting from the L1 trigger up to the HLT (L2+EF). Taken from [9].

been closely involved in the development of this infrastructure.

The L2 trigger has been allocated a budget of about 40 ms processing time per event. In order to meet this timing performance the amount of data that has to be unpacked needs to be kept to a minimum. The L2 retrieves data from the readout drivers (ROD) (as shown on Fig. 2.6) that read the data directly from the front-end boards installed on the detector subsystems. In the case of the L2 Jet trigger, it uses data from the electromagnetic and hadronic calorimeters within the $|\eta| < 3.2$ region and within the range $3.2 < |\eta| < 5$ for the forward region. The L2 jet trigger algorithm accesses data in a region centered on the L1 RoI. The limits of this regions are given by certain values

$\Delta\eta$ and $\Delta\phi$, that are configurable inputs of the L2 jet algorithm. The larger the region is, the more time it takes for the algorithm to run due to data unpacking. At the same time, the granularity chosen to calculate the E_T plays a critical role in the performance. When the granularity is fine, the precision on the determination of the energy is higher, but the process is more time consuming. If we choose a coarser granularity the precision is lower and the time of execution goes down. A final decision on the size of the region and the granularity has not yet been taken at this moment of writing. Performance vs. physics-accuracy tests are still being run and will be run during the first year of data taking in order to determine the best input parameters required for the L2 machine to behave properly.

Once data are unpacked, the L2 jet algorithm has to determine if, in the position of the given RoI, there is indeed a jet, or at least, a good candidate for a jet. Typically a cone algorithm is used: jets are defined as a cone-shaped object in the (η, ϕ)-space within a radius $R_{cone} = \sqrt{\Delta\eta^2 + \Delta\phi^2}$. The value of R_{cone} is an input configuration parameter of the L2 algorithm. The algorithm starts by using the RoI as seed, and at this position, a jet candidate of a given R_{cone} is considered as starting point. Then with the new window defined by the position of the RoI and the parameters $\Delta\eta$ and $\Delta\phi$, the energy of the jet is recalculated, yielding a new jet candidate j_1, for the first iteration of the algorithm. We replace j_0 by j_1 and repeat the recalculation of the energy of the jet. The described algorithm is repeated N times ending up with the jet j_N, where N is another input parameter of the algorithm which determines when the algorithm stops. There is not enough time to wait for the stability of the solution or to choose any other plausible/fancier technique before stopping the iteration procedure. It has been shown, at this level, that it is better to arbitrarily decide when to halt the iterations, and that only a few iterations are enough as I will explain shortly. The energy of the final jet is calculated as the sum of the energy of all the clusters falling within the cone radius. If there is not a good jet near the region pointed by the L1 RoI, the consecutive recalculations of the jet energy $j_{1,\ldots,N}$ will present significant fluctuations. The L2 Hypothesis algorithm can then decide if the final recalculation of the jet j_N is acceptable. In other words, it would be a good moment to stop iterating when we find a stable solution, but fortunately a few

iterations are enough to decide if we have come to a stable point.

On Fig. 2.10 we can see the response of the L2 Jet trigger algorithms as a function of the iteration number. On the top plot we see the variation of the transverse energy recalculated on each iteration. It is expected that a triggering jet object is going to be found in a position very close to the seed given by the L1 RoI. The convergence is very quick. In the mid and bottom plot we see the fluctuations on the ϕ and η coordinates, respectively, when a new jet is built after each iteration. The fluctuation nicely drops to a stable value less than ± 0.5 for both ϕ and η. It shows that not a lot of iterations are required when a good jet object is located close to the L1 RoI.

A calibration at L2 has to be applied [48]. The ATLAS calorimeter response to the electromagnetic component of a hadron shower is not the same as the response due to the non-electromagnetic part of the shower. The hadronic response is in general smaller due to the energy lost in the breakup of nuclei or other nuclear interactions. A correction has to be applied for it and the L2 algorithm does so to correct for the energy of the resulting L2 jet.

We have seen that a number of input parameters determine the behavior and performance of the L2 jet algorithm: the calorimeter window size given by $\Delta\eta$ and $\Delta\phi$, the radius of the cone used to build a jet R_{cone} and the number of iterations N for the energy recalculation. In order to estimate the performance of the L2 jet algorithm, the same hadronic objects spanning the interesting range of energies for hadronic activity used in the L1 algorithm have also been used for the perfomance studies on the L2 algorithm. The input parameters used for this performance exercise are summarized on Table 2.I.

The time needed by the algorithms to run 3 iterations with RoI sizes of 1.0×1.0

Parameter	Standard Jets	Forward Jets
Number of iterations	3	3
Cone radius	0.4/0.4/0.4	1/0.7/0.4
$\Delta\eta$ window size	1.4	$3 < \|\eta\| < 5$
$\Delta\phi$ window size	1.4	1.4

Table 2.I: Parameters used in the L2 jets reconstruction. The value of the cone size radius is defined for each iteration.

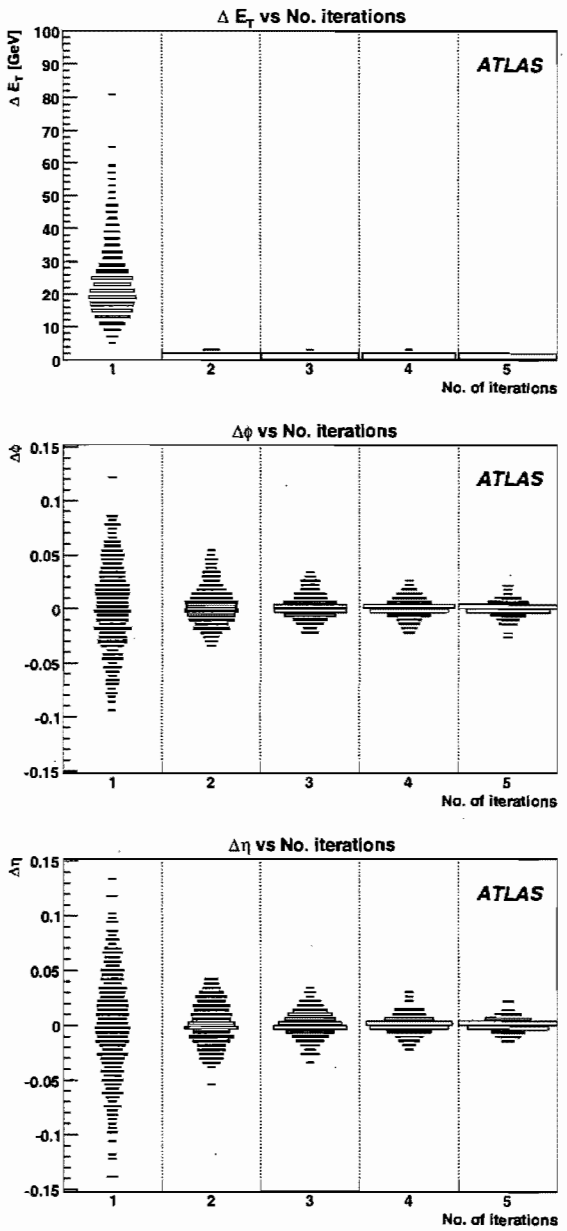

Figure 2.10: Variation in the (a) transverse energy, (b) ϕ position and (c) η position of jets as function of number of iterations performed by the L2 jet reconstruction algorithm. The area of the boxes is proportional to the number of entries in each bin.

(which is slightly bigger than $R_{cone} = 0.4$) and a size of 1.4×1.4 (taken as a limiting case) respect the time budget in both cases, which should be around 10 milliseconds. At the time of writing this thesis, processing time is still a subject of study. In the second case the time is of course bigger, about double, mainly due to unpacking. Furthermore, to understand the performance of the L2 Jet trigger, it is also necessary to study the transverse jet energy scale and jet energy resolution as a function of the jet energy. The transverse jet energy scale is defined as the L2 jet transverse energy, as measured by the L2 Jet trigger, divided by the truth jet E_T. Truth jets are in fact TruthParticle jets (where the jet reconstruction algorithm has been run on Monte Carlo information after hadronization), as used to define the energy scale for the L1 jet trigger. The results of such study are shown on figures 2.11 and 2.12. It is interesting to note that in some cases the energy scale is bigger than one. This is due to an overestimation of the collected energy within the cone of $R = 0.4$, coming from activity that does not corresponds to the actual jet, although this result includes already a proper calibration of the jet energy. According to Fig. 2.11 the transverse energy is correctly measured within 2% for a very wide energy range. The jet energy resolution decreases from 12% at low transverse energy to 4% at energies around 1 TeV as shown in Fig. 2.12 where resolution values were obtained by calculating $\sigma(E)/E$.

If the L2 jet trigger output is stable after a few iterations (as shown in Fig. 2.10), the coordinates in (η, ϕ)-space are passed to the Event Filter as input. The procedure described in this section, according to MC data, seems to be enough to bring the event rate from $\sim$ 100 kHz to a few kHz which is a good input rate for the final step in the trigger system, the Event Filter (EF). Of course these rates still depend strongly on the threshold value for each trigger signature.

2.5.2 The Event Filter trigger

The EF part of the trigger performs a more detailed reconstruction of the event, and has to run fast enough to bring the event rate from a few kHz to 200 Hz. With an infrastructure composed of several thousands of CPU-cores, the time budget to process a single event, which can contain many jets, is around 1 s. In order to satisfy the re-

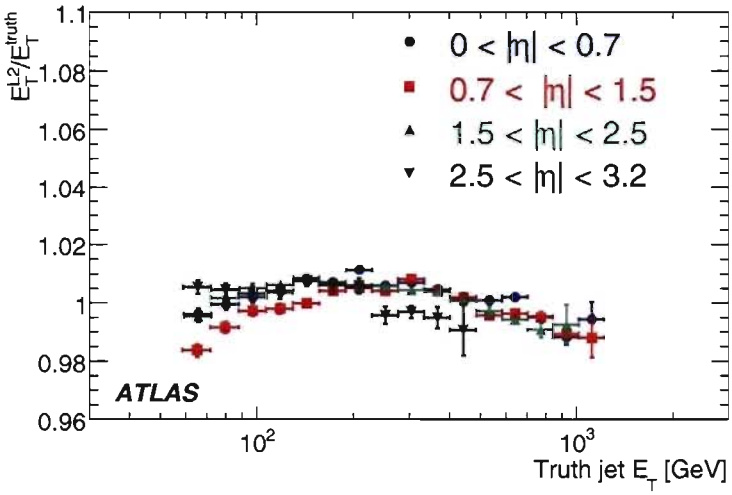

Figure 2.11: Jet energy scale for the L2 jets as a function of the truth jet E_T for four different bins in η.

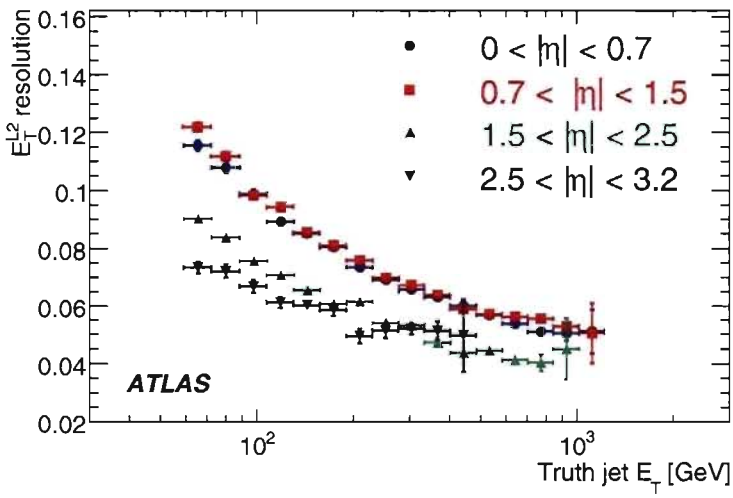

Figure 2.12: Jet energy resolution for the L2 jets as a function of the truth energy of the jet for four different bins in η.

quirement, and in the particular case of the Jet trigger, the EF runs the actual offline jet reconstruction algorithms, modified to run on a small part of the calorimeter data instead of the whole calorimeter information. The so-called on-line environment, meaning the trigger system running while the detector takes data, imposes some technical constraints on the algorithms. Some studies have been carried out to determine whether it is desirable to unpack the whole calorimeter and run the jet reconstruction with more complete calorimeter information in the EF. At the time of writing this thesis such studies are still underway. Again, the first year of data taking will answer these performance questions.

The EF jet algorithm starts when the L2 jet trigger has found a plausible jet candidate. The EF removes towers (or clusters), depending on the input of the algorithm (see appendix I), which have negative energy by combining them with adjacent ones. It also removes jet candidates with energy smaller that a given threshold. Finally it runs an offline jet algorithm (see Appendix I) like fast K_T or Cone algorithm and applies some calibration.

Just as in the L2 jet trigger algorithm, a set of input parameters has to be given to the EF jet reconstruction. The selection of these parameters of course influences the perfomance and the accuracy of the EF output. On Table 2.II, I present a list of the parameters used in the EF performance discussion that follows. The window size in the (η, ϕ)-space is quite wide, a bit wider that in the L2 algorithm. The input objects to the jet reconstruction algorithm are the so called *Towers* and the algorithm *Cone* (see appendix I). A final jet $E_T > 10$ GeV cut is also applied at the very end on the resulting jet.

Parameter	Value
Window size ($\eta \times \phi$)	1.6×1.6
Input objects	towers
jet candidate E_T cut	$E_T > 2$ GeV
Jet finding algorithm	cone
Jet finding parameter	$R_{\text{cone}} = 0.7$
Final jet E_T cut	$E_T > 10$ GeV

Table 2.II: Parameter values for the EF jet reconstruction.

For performance purposes, the same kind of data used for L1 and L2 performance studies were used in the case of the EF. The Jet energy scale and resolution are calculated as described on section 2.5.1. On Fig. 2.13, we see that starting from $\sim$ 10 GeV jets, the energy scale is within 5% and gets to be $\sim$ 2% around 200 GeV. It is important to clarify here that this very low energy activity (jets under 100 GeV) will not make part of the jet trigger menu. These low energy jets are uninteresting for most of the physics programs but understanding the response of the trigger system to low energy signals is still considered to be important since we want the trigger to be usable in the whole energy range of the calorimeter. On the other hand, the rate of low energy jets is huge and the trigger will have to be pre-scaled.

The energy scale shown on Fig. 2.13 clearly shows that the calibration does not completely correct for the energy leakage, even if the cone size used here is known to be sufficiently large for a single jet. However, this performance is considered to be adequate for EF reconstruction. The reconstruction of the accepted event will improve considerably when analysed offline, where the whole calorimeter information is accessible and time limitation is not a serious constraint. The energy resolution has a very similar behavior as for the L2 trigger.

2.6 Benchmark studies on HLT hardware

The choice of a given computer architecture has been one of the highly discussed issues of the trigger infrastructure. As a starting point, the ATLAS collaboration has decided to use, as much as possible, standard technology that can be easily repaired or replaced in an eventual hard-failure scenario. I was involved in the trigger system by the time such a choice was still to be taken and I contributed with the benchmarking and testing of a few different architectures. The LINPACK Benchmarks [49] were used for benchmarking purposes of floating point computing power. The LINPACK are a set of well-known computer programs that are optimized to give a measurement of the power of a given system to perform floating point operations. I chose this benchmark since it is standard and can be easily compared to other tests performed independently

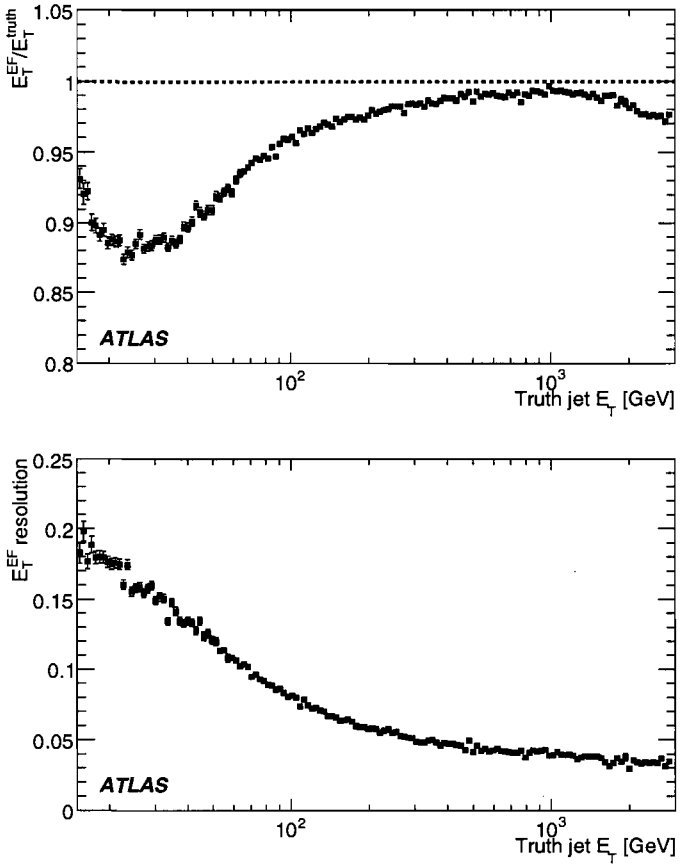

Figure 2.13: The EF jet transverse energy scale and resolution as function of truth jet E_T.

on different architectures. On Fig. 2.14 we see as a function of the matrix size used[4] the total elapsed time (left axis) required for the benchmark to run, and the number of millions of float point operations the machine can perform per second (MFlops, right axis). In this plot the test is done on a AMD™[5] processor. The same benchmark was performed with INTEL™[6] CPU cores and they turn out to be comparable in terms of computing power but AMD™ is known to dissipate much less heat.

[4]The algorithm used gives the solution of a system of equations using linear algebra. The problem gets reduced to matrix manipulation. The multiple $N_{\text{rows}} \times N_{\text{colums}}$ is the value on the x axis.

[5]AMD™ is a trademark of AMD Corporation and is used here only with academic purposes.

[6]INTEL™ is a trademark of Intel Corporation and is used here only with academic purposes.

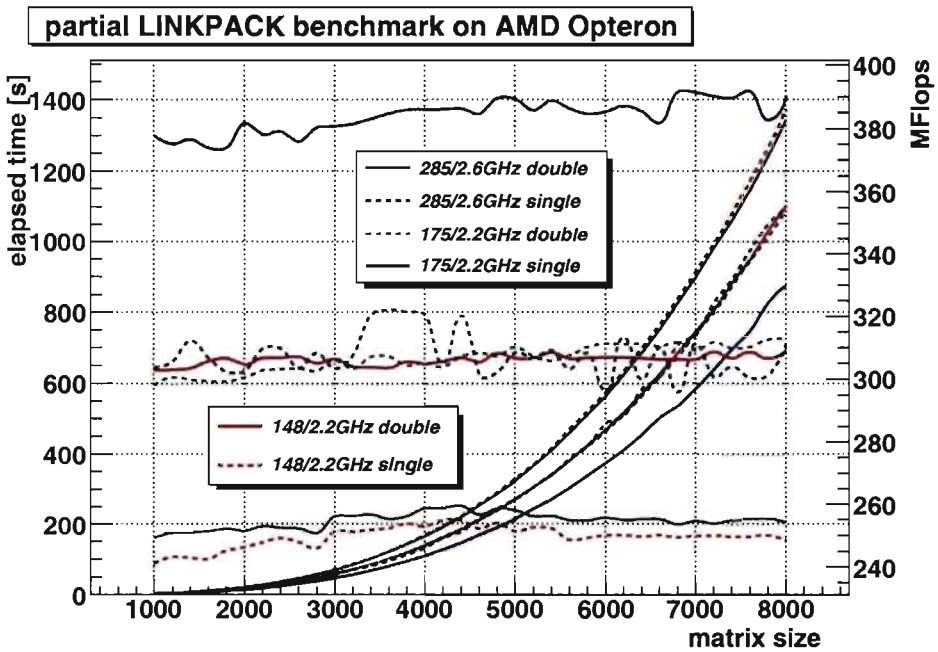

Figure 2.14: Overall Benchmark of a L2 or EF core for AMD infrastructure. Part of the preliminary studies made to select the appropriate hardware to be used in Point1 (where the ATLAS experiments sits in Swiss territory) for the L2 and EF process units farms. The left axis corresponds to the elapsed time and applies to the six curves monotonously increasing. The right axis shows values in MFlops (millions of float point operations per second) and applies to the other six curves (horizontally shaped) presenting fluctuations. In the legend 285, 175 and 148 correspond to the CPU models. The fluctuations are due to the multi-tasking characteristics of the OS. In the case of dual-core (double) CPU, only one core is being used.

2.7 The ATLAS software - ATHENA

ATHENA is a framework for data Generation, Simulation, Reconstruction, Event Selection, and Analysis software for the ATLAS experiment. From the technical point of view, ATHENA is a Python driven application for high-throughput data processing. It is written mainly in C++ in the spirit of generic programming, and meant to make all the software written under certain design constraints and scalable effort. That means that wherever a development is done with ATHENA, any user should be able to easily request an existing tool and use it (as input for example) along with some new algorithm he may

be trying to implement. It uses the power of an Object Oriented Programming (OOP) approach to implement the family of abstractions required by the software design to run a sequence of algorithms necessary to perform a given task. ATHENA has many different functionalities, all driven by the same core, named Gaudi, which could be identified as the kernel of the application. The ATHENA framework is the core application for most of the calculations we make for the ATLAS experiment, and is the unified software scheme that ATLAS researchers use on a regular basis.

2.8 Full simulation with the ATLAS detector

Once the MC data for a given signal are produced with a generator of some sort (in this case, for example, the modified version of PYTHIA as described in section 3.2), the final physical particles, with their 4-vectors, produced by the generator are allowed to interact with the detector material to produce simulated signals. In the particular case of ATLAS, an extremely complex virtual representation of the whole ATLAS detector using the Geant4 (see appendix III for details) radiation-matter-interaction simulation kit has been developed. A full 3D representation of the detector with enough detail to represent the whole geometry of each of the subsystems has been built over the last years. This simulation is the result of an effort by a large group within the collaboration, and the author of this thesis was involved in part of this development as well (details will not be given due to the pure software nature of the contribution in this particular subject).

After all the particles produced by the MC generator have been traced through the detector, leaving *hits* of the deposited energy in the sensitive parts, we obtain simulated signals in the same form as real data (except for additional truth information).

There are several advantages to this full and realistic simulation:

- The first and probably the most evident is that detector effects (particle identification, miss-taging, resolution, etc) can be extremely important in order to evaluate the discovery potential of a given physics process.

- If such a signal looks promising, one must start developing the expertise and the

tools to be able to identify the signatures and perform the analysis. From experience we know that it can be a major task.

- It helps to understand in advance the detector performance. The calibration can be prepared and understood before the detector starts running with the actual LHC beam.

- If a signal turns out to have a potential for discovery in ATLAS one wants to make sure the trigger will be ready for the given physics channel.

Before presenting the results, in the next section I will give a summary of the ATLAS software used to process the data. The software will be able to work either with simulated or real data, vastly enhancing the reach of the work done.

2.9 Offline software and the Event Data Model towards analysis

The *ATLAS offline software* must satisfy certain guidelines. First, it should be able to process the events delivered by the ATLAS trigger and data acquisition system. It must then deliver the processed results to physicists within the ATLAS Collaboration, all over the world. It must provide tools for physicist to analyse the processed information in order to produce physics results. Finally, it must provide tools to simulate physics processes as realistically as possible.

The software is constrained by the processing time and memory consumption per event necessary to meet budgetary limits (number of CPUs necessary to process ATLAS data for example). The complexity and scale of ATLAS requires that it be highly modular and robust, and flexible enough to meet the needs of the experiment throughout its operational lifetime. There will no doubt be changes in the physics goals and even detector hardware during this period and the software must accommodate these, i.e. the software design and implementation ought to constitute a scalable effort.

In this spirit there exists a family of tools and services enclosed in a software package called ATHENA(as discussed in section 2.7). One can follow very different paths of data processing. Let us take first a rather unusual case. If a person is interested in the

performance of the forward calorimeter for single protons of a given energy in the very forward region, the user can setup the Geant4 simulation of the ATLAS detector, send protons of a given energy and study the result of the interaction of the charged particle with the detector material. In the process, a number of services enter the job in an automatized basis to assist the task. To be more precise, when setting up the forward detector for full simulation, the whole Geant4 machinery is put in place to perform the simulation, and the detector geometry and material information is pulled up from the detector geometry data base containing the description of the ATLAS machine. Geometry building is something the user (the physicist) does not want to deal with and it is done automatically as a detector simulation job is started up. Along with the geometry, the data handling structure is also retrieved automatically. The Event Data Model (EDM) governs the handling of data at all stages of the processing, i.e. once the Geant4 simulation is completed, the result is presented in *Hit Collections* which are objects that contain the information from the sensitive materials in the detectors which have responded to the passage of the particles. Particle reconstruction (particle identification) software is then run in order to identify objects out of the hits. The primary data-processing activities that must be supported for all of the detector subsystems are:

- Event generation: Monte Carlo production with generators like PYTHIA , MADGRAPH and many others (see appendix II),
- Simulation: Geant4 simulation of the passage of particles through the detector as described in appendix III,
- Detector reconstruction: Identification of known objects like electrons, muons, jets, E_T miss measurement, etc. The same software will be used for simulated and real data.
- Physics analysis: Final physics analysis has to be assisted by the software infrastructure using advanced tools that allow the physicist to process and interpret the data at the level one wants to do so, i.e. truth information, Geant4 hits, calorimeter details, reconstructed objects, or any other aspect of the detector response.

- Triggering: The software infrastructure has to be able to handle Trigger data in the offline and the online scenario. In the particular case of online running, the infrastructure changes considerably, as was mentioned in the trigger section.

- Online monitoring: Monitoring of the functioning of the whole ATLAS system at *point-1*[7] or remotely is supported by the EDM as well,

- Calibration and alignment processing: Particular data handling for calibration is necessary.

All these tasks are assisted by a handful of services that automatically engage when a given task requires them.

2.10 Radiation environment

The precise evaluation of spectral characteristics and knowledge of the radiation field in the ATLAS detector and cavern is necessary for the understanding of the performance of various detector subsystems and prediction of their useful lifetimes, and provision of quantitative information on the fluxes and flux determination of the main radiation types in the experiment. To perform such measurements we use the MediPix2 device, developed at CERN with the collaboration of several institutions around the world[50]. The MediPix2 device allows real-time measurement of the radiation field. I contributed to the project by establishing the calibration procedure for the ATLAS-MPX (MediPix used in ATLAS) devices now installed in ATLAS. I also designed and implemented part of the analysis software infrastructure meant for high-throughput data handling. Both implementations are currently being used for the ATLAS-MPX measurements. A brief discussion of these two contributions is presented in the following sections.

[7]Site where the ATLAS detector operates in Swiss territory.

2.10.1 The ATLAS-MPX (MediPix2) detector

The ATLAS-MPX detector is using the MediPix2 chip [8]. It consists of a semiconductor detector bonded to a photon counting readout electronics. These position sensitive modules are successfully used in spectroscopic radiation measurements[50].

The Medipix2-pixel detector consists of a silicon layer (active part) 300μm thick bonded to the readout chip Medipix2. The Medipix2 readout chip consists of a matrix of 256×256 identical readout chains. They are bonded to respective rectifying diodes so defining a structure of pixels, each measuring $55\mu\text{m} \times 55\mu\text{m}$ on the silicon chip (sensor). The use of 0.25μm CMOS process has allowed this small pixel size. The detector is fully controlled by the Universal Serial Bus (USB) [51], which is presently the most widespread PC interface, that converts ATLAS-MPX into a small, portable, PC controlled particle detector. The ATLAS-MPX offers the possibility of energy threshold adjustments, thus creating an energy window, which allows a selection of an energy interval for detecting radiation. A network of ATLAS-MPX devices is installed within the ATLAS detector and cavern [52]. Four devices are located between the moderator shielding and Liquid Argon (LAr) calorimeter (two on each of the two sides of the ATLAS detector). Similarly, two devices on each side, are installed along the TileCal (scintillator/iron hadronic calorimeter). A total of four devices are located near the ATLAS muon chambers and two devices are located near the very forward shielding. These devices allow real-time measurement of the fluxes composition and the spectroscopic characteristics of the radiation within the detector and its cavern.

In Fig. 2.15 one can see a picture of an ATLAS-MPX device similar to those used in the ATLAS-MPX project. As shown in the picture, the left side of the device (the green PCB[9]) contains the actual 65 K (256×256) pixels matrix which corresponds to the little gray square at the very left of the picture. This square has an area of about $14\text{mm} \times 14\text{mm}$. The remaining components in the board are the read-out electronics. The right hand side of the device (the blue box) corresponds to the USB interface that works as a bridge between the read-out electronics and the USB port of a standard PC.

[8] MediPix2 stands for the second generation of these devices

[9] Printed Circuit Board.

Figure 2.15: The ATLAS-MPX device.

As an illustration of the regular operation of the device, I am going to take the example of a ATLAS-MPX being irradiated with a source of Am-241 which emits α-particles and X-rays. The pixel matrix delivers a direct image of the striking radiation. In Fig. 2.16 you can see in the left-top side, a blob[10] with a round shape that corresponds to an alpha particle. The very small dots in black, correspond to photons. The type of radiation can be very well differentiated by the shape of the blobs and dots. Photons are of particular interest here since they are to be used for the energy calibration of the device. Photons can make hits in one pixel or a few pixels depending on the type of interaction that they undergo in the pixels material. Radiation interacting by photoelectric effect will produce electrons that will most likely deposit their whole energy within a single pixel. On the other hand, a photon interacting by Compton effect close to the surface of the detector will produce an electron with enough energy to traverse about 55μm (one pixel) and beyond, possibly activating more than one pixel. Photons making

[10]Blob is a general term used in imaging to describe a group of active pixels.

blobs of more than 5 pixels are rare. In general, the recognition of isolated structures of 5 or less pixels is already a good way of identify photons in a frame. Photons activating a single pixel are called *single hits* and are used for calibration purposes as shown in the following section.

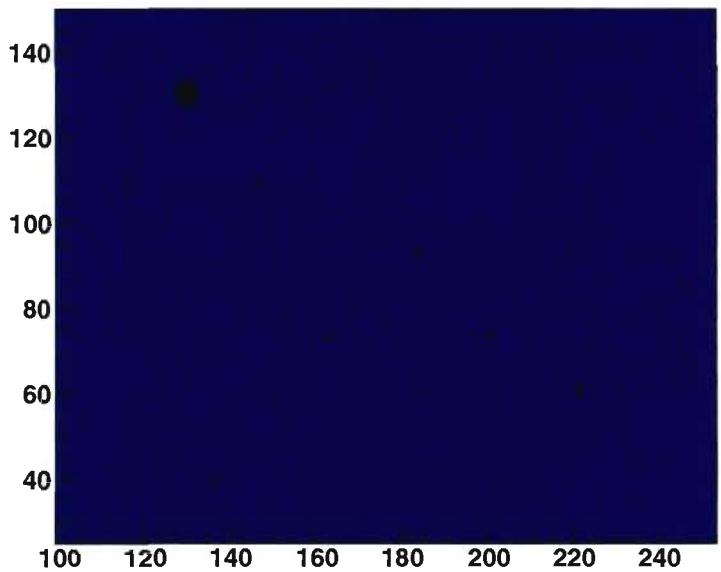

Figure 2.16: Frame of Am-241 radiation taken with a ATLAS-MPX device.

2.10.2 Threshold calibration of an ATLAS-MPX device for use in the ATLAS experiment

A threshold calibration procedure for the ATLAS-MPX device was developed. A calibration protocol was implemented using only a source of Am-241. The calibration is performed establishing a direct relation between the peaks identified in the measured spectra from Am-241 and some specific ATLAS-MPX-DAQ values which are those associated with the energy threshold acceptance of deposited energy in a given pixel. There is one variable, called THL, in the system to set up the threshold. When one changes the THL value, the energy threshold changes. THL is an arbitrary value coming

from the data acquisition software and the correspondence between every THL value and energy needs to be known. There is also a second energy-related parameter called THL-FBK (Threshold-Feedback, where feedback stands for some internal voltage in the electronics. Further detail on the functioning of the read-out system electronics is not necessary for this discussion). The relation between THL and THL-FBK is well known and is linear. Then, if for a given device we know the relation between energy and THL, or energy and THL-FBK, we can establish the correspondence between an energy threshold and a given DAQ setup. In such a case, we say to have calibrated the device.

This protocol considers the use of a source of Am-241 which, according to the nudat2[11] software from BNL (Brookhaven National Laboratory), gives a number of (most important) emissions of X-ray spectra as shown in Table. 2.III.

Within this energy range (from 14 to 60 keV) the most relevant interactions of photons in silicon will be mainly via the photoelectric effect and via Compton scattering, less probable but still present. The scattered electrons in silicon will deposit all their energy in the medium and, depending mainly on the direction of incidence, it is very likely to happen in a single pixel in this energy range. Making this assumption, we can consider that all single hits (single isolated pixels illuminated as shown in Fig. 2.16) in the ATLAS-MPX, will correspond to an energy deposition very close to the energy of the incident photons. This is why it is possible to implement a quite direct calibration procedure where a simple peak identification in the spectra will give us the relation between the ATLAS-MPX-DAQ values (THL and THL-FBK) and the energy. For this threshold calibration only single hits are considered.

Using ATLAS-MPX data, in figures 2.17 and 2.18, one can perform the peak iden-

[11] see http://www.nndc.bnl.gov/nudat2/

Energy (keV)	Intensity (%)	Dose (MeV/Bq-s)
13.9	37 % 3	0.0051 5
26.3446 2	2.27 % 12	6.0E-4 3
59.5409 1	35.9 % 4	0.02138 22

Table 2.III: Am-241 most important X-Ray emissions.

tification for 60 keV and 14 keV respectively. The top figure corresponds to the flux of photons (in units of number of single hits per second) as a function of the THL value, and the bottom figure is the differential of the flux which produces the spectra. According to other measurements, for several different energies between 14 and 60 keV (shown in the next section), the relation between THL-FBK (or THL) is proved to be linear since they fall on the linear function predicted by the 60 keV and 14 keV peaks. In this way we show that these two points are sufficient to perform a calibration.

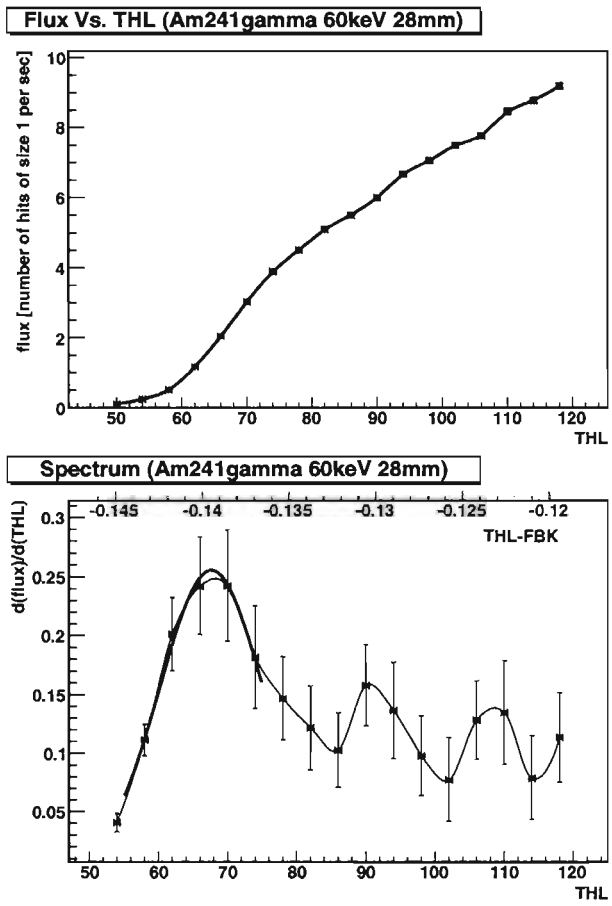

Figure 2.17: Response of ATLAS-MPX to an Am241 source at a distance of 28mm. In this range of THL(THL-FBK) we identify the 60 keV peak. The top plot shows the number of counts (single hits) per second as a function of THL and the bottom plot corresponds to the spectrum.

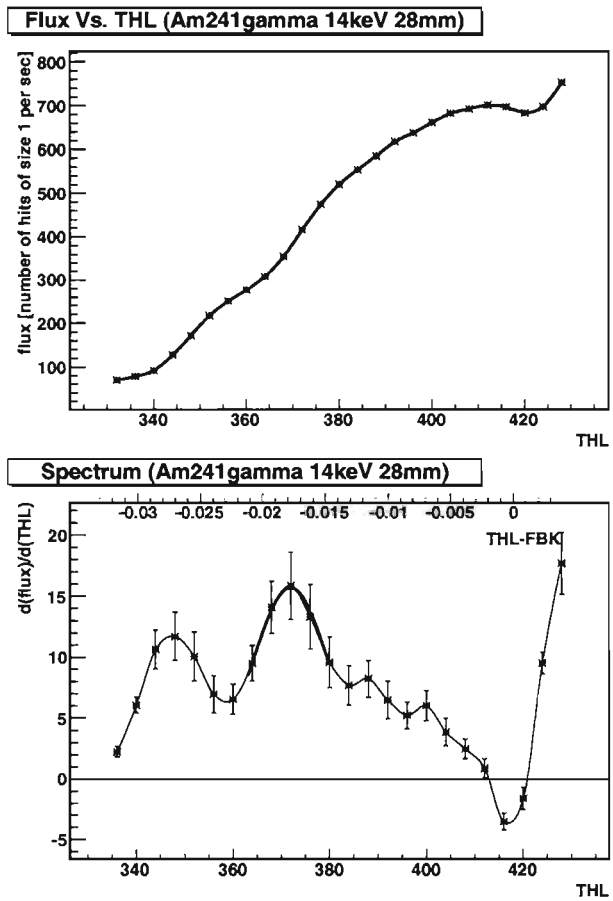

Figure 2.18: Response of ATLAS-MPX to an Am-241 source at a distance of 28mm. In this range of THL(THL-FBK) we identify the 13.9 keV peak. The top plot shows the number of counts (single hits) per second as a function of THL and the bottom plot corresponds to the spectrum.

2.10.3 Test of the calibration with 33keV X-Rays and weak 26keV emission from Am241

To test the linear relation between THL (or THL-FBK) and Energy, two more spectroscopy measurements were performed for Am-241 (26keV) and X-rays (33keV). In Fig. 2.19 the spectrum measured with ATLAS-MPX for 33keV X-Rays is shown. This measurement was taken at the Czech Metrology Institute using X-Ray tubes (The Kerma rate was $3.3481 \times 10^{-7} Gy/s$). Also a measurement for the very weak emission of Am-241 at 26 keV is shown in figure 2.20. Despite the fact that the 26keV peak measurement

lacks statistics, its identification was possible and its position in the Threshold-Energy calibration shown on figure 2.21 falls into the straight line dictated by the points at 14keV and 60keV. The calibration proves to be successful for these two cases.

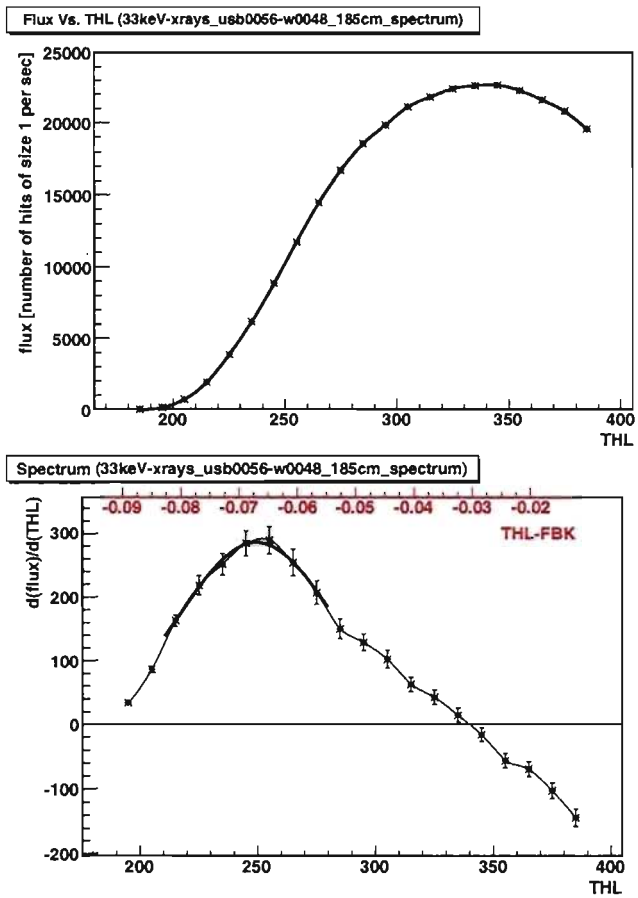

Figure 2.19: Response of ATLAS-MPX to X-Ray radiation (XRay tube). In this range of THL(THL-FBK) we identify a 33 keV peak. The first plot shows the number of counts per second as a function of THL and the second plot corresponds to the spectrum.

A fit of the form $ax + b$ including the four points shown in figure 2.21 gives the following results:

$$\begin{aligned} a &= -2.69 \times 10^{-3} \pm 1.1 \times 10^{-4} \\ b &= 2.06 \times 10^{-2} \pm 4.3 \times 10^{-3}. \end{aligned}$$

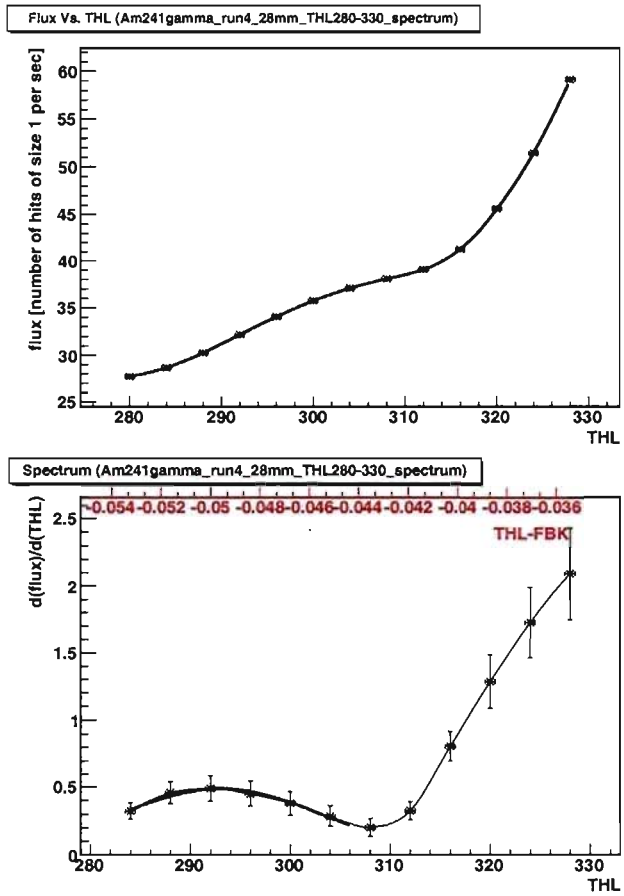

Figure 2.20: Response of ATLAS-MPX to an Am-241 source at a distance of 28mm. In this range of THL(THL-FBK) we identify the 26 keV peak. The top plot shows the number of counts per second (single hits) as a function of THL and the bottom plot corresponds to the spectrum.

Only the points for 14 keV and 60 keV are used to perform the linear fit and produce a threshold calibration for a given device. It is worth stressing the applicability of the work described in this section. The following conclusions can be drawn:

- The threshold-calibration procedure described, can be used to calibrate the ATLAS-MPX devices installed in the ATLAS detector and cavern. At the time of writing this thesis all the ATLAS-MPX devices installed in ATLAS were calibrated using this procedure.

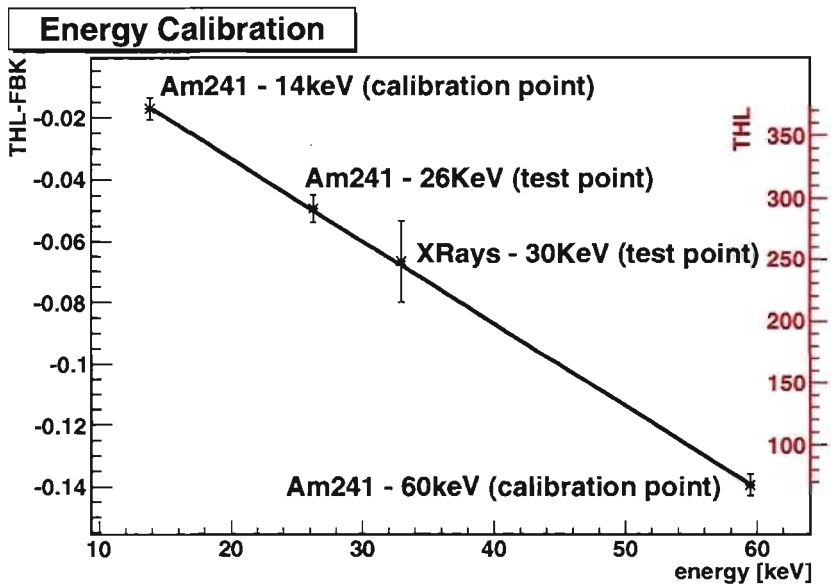

Figure 2.21: Linear relation between the DAQ parameters (THL-FBK and THL) of a ATLAS-MPX device and the Energy. Two calibration points (14keV and 60keV) plus two test points (26keV and 33keV) are shown in the plot.

- The relation between the ATLAS-MPX-DAQ values such as THL or THL-FBK and the energy was proven to be linear in the 14keV to 60keV range.

2.10.4 The MediPix Analysis Framework (MAF) and the MediPix data model (MDM)

The ATLAS-MPX project introduces new requirements in terms of data accessibility which dictates a natural path for the implementation of: firstly, a data model that allows storage of MediPix data in a convenient way, and secondly an analysis framework that is meant to be a workbench for the physicist who wants to study the MediPix data.

Currently the DAQ system of MediPix delivers data in a format that is a bit inconvenient for high through-put applications. The MDM based on the ROOT framework, provides a convenient data structure to hold data and allows very fast access to it. Such development was found to be necessary for a number of other future developments with MediPix devices and it is, as a matter of fact, already being used by other groups within

the MediPix collaboration for different implementations. On the other hand, a common-core data analysis framework for MediPix was also developed. Analysis of MediPix data has been quite heterogeneous over the years since each group has had to find its way through the data analysis and up to now, no effort in terms of the scalability of the solutions for analysis had been performed.

The author of this thesis designed and implemented an analysis framework that supports the MDM and delivers the functionality needed to perform all types of calculations with frames, giving total freedom to the user to implement anything he may imagine. The design of the framework obliges the user to write software in a way that his solution can be very easily used in combination with other algorithms implemented separately. The results previously presented were obtained with a very early version of the MAF software. At the time of writing of this thesis the implementation of the MAF has already progressed a lot and is being widely used by several groups. No details on the design nor the implementation of such a software development is pertinent in this work due to its strong computing science orientation. But it is worth saying that all the results presented in this section rely (in terms of software) on the MAF, and that this effort has been useful for a number of people.

CHAPTER 3

PHENOMENOLOGY

As mentioned in the introduction, one of the principal reasons for building the LHC and its detectors is to understand the origin of electroweak symmetry breaking (EWSB). The search for the Higgs boson has only yielded lower bounds but its discovery is still possible (see Fig. 1.4 right). Alternatively, we have seen that VB scattering becomes a strong interaction at high energy. It is therefore important to investigate some general strongly interacting symmetry-breaking scenario. Here, we consider this process in the framework of the ChL model described in Chapter 1. It is an effective model which describes electroweak physics at low energy, and includes higher order momentum terms for extrapolation to higher energy. A regularization method insures that amplitudes are properly unitarized.

As was discussed in chapter 1, we expect to have some sensitivity to this process at the LHC only in the presence of resonances. One possible scenario, of course, is that the scattering is non-resonant. In that case, we expect that the sensitivity at the LHC will be quite poor since this kind of signal will be very hard to identify without an excellent understanding of the continuum background in the high energy region. Non-resonant studies do not represent a suitable scenario for the LHC except, perhaps, with very high luminosity, and we will not present any results on this work, as discussed in Chapter 1. Fortunately, from the phenomenological point of view, a resonant scenario results from unitarisation by the Inverse Amplitude Method (IAM), as described and implemented in [4]. It yields poles for certain values of α_4 and α_5 (previously defined in chapter 1), that can be interpreted as resonances. Hence, in the Chiral Lagrangian + IAM formalism, resonances can be mapped in a 2-D space of parameters respecting the Chiral Lagrangian symmetry and unitarity. This scenario has been studied first in [53], [54] and [55].

3.1 Characteristic Signatures of Vector Boson Scattering

On Fig. 3.1 we see schematically the signal which we will be considering. Vector bosons are radiated from the incoming quarks in the pp collision. They interact through a resonance, and the decay of this high mass ChL resonance will produce two highly-boosted vector bosons in the central rapidity region of the detector. For transverse momenta greater than about 250 GeV, a hadronically decaying vector boson will begin to be seen as one single wide and heavy jet which will be important to distinguish from background QCD jets. Algorithms for reconstructing composite heavy jets will therefore need to be developed.

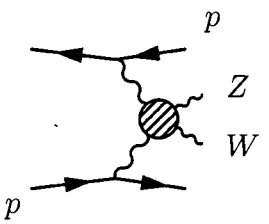

Figure 3.1: The jets arising from the incident partons (solid lines) which have emitted the vector bosons are the common characteristic to all the VBF studies.

A characteristic signature of vector boson scattering is the presence of two high rapidity and high energy "tag" jets [56, 57, 58], arising from the quarks which radiate the incoming vector bosons. As we will show later in section 3.2.2 the two initial quarks that radiate the VB have very high rapidity (see Fig. 3.13(a)). Such forward jets are expected to be much less prominent in processes involving gluon or electroweak boson exchange with bremsstrahlung of vector bosons. In the latter case, these vector bosons are mostly transverse and have a harder p_T spectrum than in $W_L W_L$ scattering. Correspondingly, the outgoing primary quarks have a harder p_T and are therefore less forward. On Fig. 3.2 we show the η distribution of the initial quarks in WW scattering. The VBS process can thus be efficiently distinguished from contributions to the production of (mostly transversely polarized) final state vector bosons due to bremsstrahlung of these vector bosons from the quarks. In that latter case, the accompanying jets are softer and more central.

A further component of the signature is the suppression of QCD radiation in the rapidity interval between the tag jets due to the fact that no colour is exchanged between

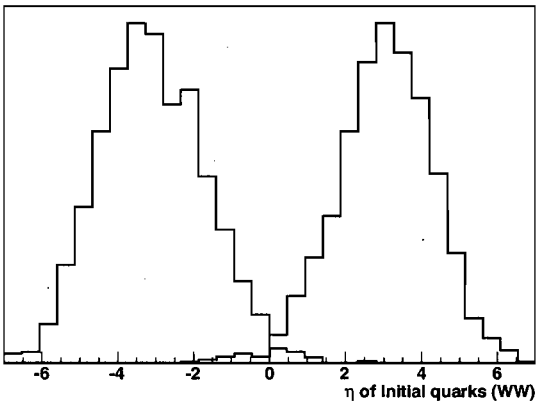

Figure 3.2: Pseudorapidity of the initial quarks in signal events $qqWW$, $m = 800$ GeV.

the interacting quarks in these processes [59]. Indeed, the Z and W in the central region are color-neutral. This characteristic feature should allow for efficient use of a central jet veto to suppress backgrounds.

In the particular case of the SM, the processes contributing to the $WZ \to WZ$ production are those on Fig. 3.3, including the Higgs exchange diagram (last one of the figure, where h stands for the SM Higgs particle). The Higgs diagram actually plays an important role, guaranteeing regularization of the amplitude. In the ChL scenario, the diagrams contributing are basically the same but of course the Higgs diagram is absent and replaced by a new s-channel resonance (let us call it ρ).

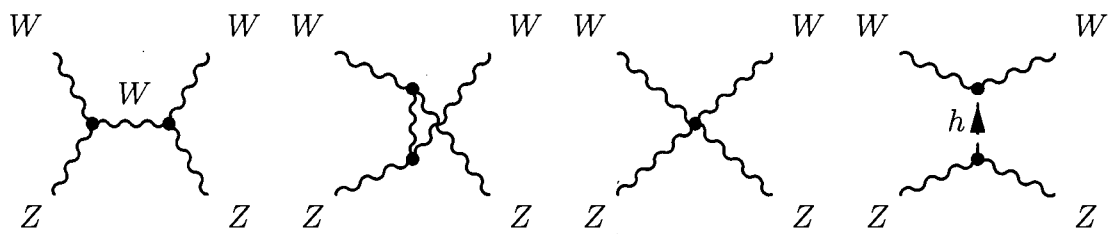

Figure 3.3: $WZ \to WZ$ production diagrams in the SM scenario including Higgs exchange. In the ChL model the diagrams contributing are basically the same except for the Higgs exchange that will be replaced by a vector (or scalar) resonance.

The high QCD background at the LHC naturally leads us to focus on "semi-leptonic"

vector boson events; that is, those events where one W or Z boson decays leptonically, and the other decays hadronically. These channels represent the best compromise in that there is only at most one neutrino, so the diboson mass may be reconstructed with reasonable resolution, and the backgrounds can be reduced to a manageable level by the requirement of leptons and/or missing transverse energy ($\not\!\!E_T$). Fully-leptonic events are also useful in cases where clear resonances are present, where a kinematic edge may be visible and the backgrounds may be reduced even further. The case of resonant $ZZ \to \ell^+\ell^-\nu\bar{\nu}$ can also lead to a clean signature. Fully hadronic events may be useable at very high diboson energies, but this possibility is not considered further here. Thus, the study of vector boson scattering events will also require a good understanding of detector performance for electrons, muons and $\not\!\!E_T$.

There is also the case of $WW/WZ \to l^{\pm}\nu jj$ analysed by the UCL[1] group [10]. In this case the $\not\!\!E_T$ of the event plus the lepton from the decay of the W are used to determine the z component of the neutrino and therefore, allow the reconstruction of the mass of the leptonically decaying W. The Z decays hadronically and its reconstruction is done in a similar way as for the hadronic W channels. These have also proven to be suitable processes for discovery at high luminosity ($\sim 100\text{fb}^{-1}$).

3.2 List of samples

Table 3.I lists the Monte Carlo samples, produced with full detector simulation, used in the present analysis. Also listed are the cross sections and normalization factors for $\sim 100\text{fb}^{-1}$.

3.2.1 Signals

As discussed in Chapter. 1, the dimension-4 terms in the ChL of anomalous couplings describing vector boson scattering can be written simply as two terms with coefficients α_4 and α_5. On Fig. 3.4 we can see the α_4, α_5 parameter space for vector resonances

[1]University College London. These channels were part of the CSC exercise (see section 3.2), but they are not discussed here because they were mostly performed by the UCL group. The corresponding MC samples are not included in Table. 3.I

Sample name	Dataset	(a_4, a_5)	Generator	$\sigma \times Br$, fb	N_{events}	Norm 100fb^{-1}
Signals						
$qqWZ \to qqjj\ell\ell$, $m = 500$ GeV	5674	–	PYTHIA-73	25.2	5000	0.50
$qqWZ \to qq\ell\nu jj$, $m = 500$ GeV	5675	–	PYTHIA-73	83.9	3250	2.58
$qqWZ \to qq\ell\nu\ell\ell$, $m = 500$ GeV	5676	–	PYTHIA-73	8.0	4850	0.16
$qqWZ \to qqjj\ell\ell$, $m = 800$ GeV	5677	$(0.009, -0.009)$	PYTHIA-ChL	10.5	5000	0.21
$qqWZ \to qqjj\ell\ell$, $m = 1.1$ TeV	5671	$(0.00875, -0.00125)$	PYTHIA-ChL	3.7	4500	0.08
$qqWZ \to qq\ell\nu\ell\ell$, $m = 1.1$ TeV	5673	$(0.00875, -0.00125)$	PYTHIA-ChL	1.18	2000	0.06
$qqZZ \to qq\nu\nu\ell\ell$, $m = 500$ GeV	5691	$(0.009, 0.009)$	PYTHIA-ChL	4.0	3500	0.001
Backgrounds						
$jjWZ \to jj\ell\nu\ell\ell$	5955	–	MADGRAPH	132.5	21850	0.61
$jjZZ \to jj\nu\nu\ell\ell$	5959	–	MADGRAPH	45.5	16750	0.27
Z + 4 jets, $(\alpha_s^4, \alpha_{ew}^1)$	5166	–	MADGRAPH	2394.0	15122	15.83
Z + 4 jets, $(\alpha_s^2, \alpha_{ew}^3)$	5167	–	MADGRAPH	33.6	17700	0.19
Z + 4 jets, (α_{ew}^5)		–	MADGRAPH	2.4	2000	0.12
Z + 3 jets, $(\alpha_s^3, \alpha_{ew}^1)$	6667	–	MADGRAPH	104.6	5000	2.09
Z + 3 jets, $(\alpha_s^1, \alpha_{ew}^3)$	6666	–	MADGRAPH	4.3	3750	0.11
$t\bar{t}$	5200	–	MC@NLO	833 ± 100*	543800	67.40

Table 3.I: Table of samples and generators used. The (a_4, a_5) column does not apply for the samples marked with $-$. The column labeled as **dataset** corresponds to an internal ATLAS official MC production identification number for the given signature. It is included here in case the reader is familiar with the software organization of the CSC exercise and would like to fetch the data we used, to reproduce the studies presented in this work. * The cross section value for the $t\bar{t}$ sample does not contain a branching ratio and is given in pb.

(left) and scalar resonances (right). Here we will study, as benchmarks, three points in this parameter space (only for vector resonances). The first one is exactly $P2$ (marked on Fig. 3.4) which gives a resonance close to 1.15 TeV, the second one is $(a_4 = 0.009, a_5 = -0.009)$ (not marked in the figure) which gives a resonance around 800 GeV and a third point which gives a resonance at 500 GeV. The second and third give a narrower peak, and have a higher cross section than the 1.15 TeV case making them a priori more suitable for discovery but at the same time, as we will see, they are more exposed to the background. The resonance at $P2$ is still expected to have a good discovery potential but will certainly have to wait for at least 100 fb^{-1} as we will see later in the final results.

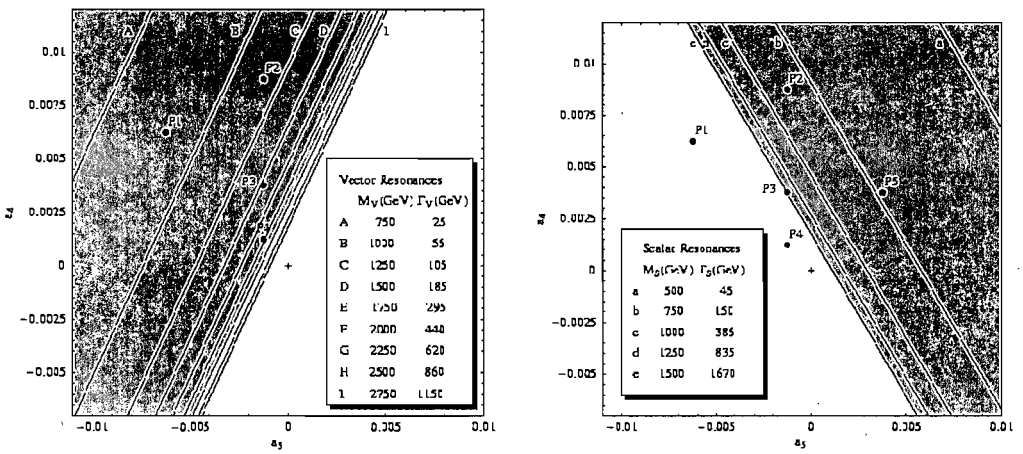

Figure 3.4: Possible resonances in the a_4, a_5 parameter space. The points P2 and $(a_4 = 0.009, a_5 = -0.009)$ for vector resonances are tested in this work. The white areas represent a region where no resonances within the applicable energy range show up. These plots have been taken from [4].

Three resonances predicted by the ChL model with the selected sets of parameters α_4, α_5 are shown in Fig. 3.5 at parton level. They are relatively narrow, and stand out well above the VB scattering continuum. This only illustrates the power of the ChL theory to predict resonances in the VBF channels that we will later study with the ATLAS detector. In this particular case the PYTHIA generator has been used (further details are given in the appendix II).

The first set of samples shown in Table 3.I represents different reference cases of

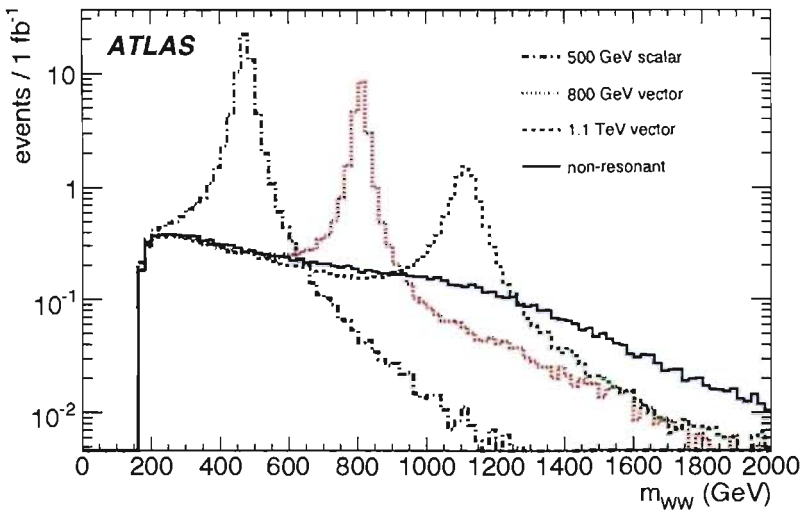

Figure 3.5: Number of events per fb^{-1} as a function of the di-boson invariant mass for different resonance masses studied here [10].

vector boson scattering signals:

- PYTHIA-73: For the samples labelled "PYTHIA-73", the process 73 (longitudinal WZ scattering) was selected, with MSTP(46)=5 (QCD-like model of [60] with Padé unitarisation). All other switches were left as default. This is meant to represent a generic narrow WZ resonance. The signals for 500 GeV in Table. 3.I were produced with this PYTHIA process. They give the same cross section as a ChL resonance of this mass, within a 1% error. Therefore, they can also be interpreted also as ChL resonances.

- PYTHIA-ChL: samples with generator labelled "PYTHIA-ChL" in the table use a modified version of PYTHIA routine PYSGHG. The modification involves replacing the scattering amplitudes calculated for processes 73–77 by those given by Dobado et al [4] with parameters α_4 and α_5 as explained in section 1.7.2. This modification to the PYTHIA generator was implemented by G. Azuelos and was connected to the PYTHIA interface to ATHENA (see section 2.7). The interface was validated by a number of people in the ATLAS Exotics Physics group and

later used officially for VBF studies by the ATLAS collaboration [10].

3.2.1.1 Definition of signal

In order to have a gauge-invariant set of diagrams for the background, in spite of a Higgsless scenario, a low mass Higgs will be assumed. A resonance signal will be defined here as an excess of events in the resonance mass region over the number expected from the Standard Model continuum when the Higgs boson mass is set at 100 GeV. This ensures that longitudinal vector boson scattering will contribute negligibly to the process. This definition follows the prescription of [6].

3.2.2 Backgrounds

The background is composed of all those other processes that can occur and mimic the signal. It is important to understand well these backgrounds and find selection criteria to suppress them with respect to signal events. These background samples include events with two vector bosons and two jets in the final state, arising from gluon or electroweak vector boson exchange between incoming quarks. As mentioned above, the vector bosons are here mostly transverse and emitted more centrally than in the case of longitudinal vector boson pair scattering.

- $jjWZ \rightarrow jj\ell\nu\ell\ell$, where j is a quark or gluon:
  This process was produced with MADGRAPH, but the decay of the vector bosons was performed in PYTHIA. Note that the semi-leptonic cases are already included in samples W+jets and Z+ jets (see below). Only the purely leptonic cases make use of this background. Additional preselection cuts were applied in this case as follows:

  - $E_T(W) > 45$ GeV and $E_T(Z) > 45$ GeV. On Fig. 3.6, the E_T distribution of the Z at parton level is shown for the signal $qqWZ \rightarrow qqjj\ell\ell$, $m = 500$ GeV. It is clear that the preselection cut does not have any impact at all and we can safely use it. In the case of the resonances at 800 GeV and 1.1 TeV the cut is also safe, since vector bosons have even higher energy.

An example Feynam diagram involved in the matrix element calculation is shown in Fig. 3.7.

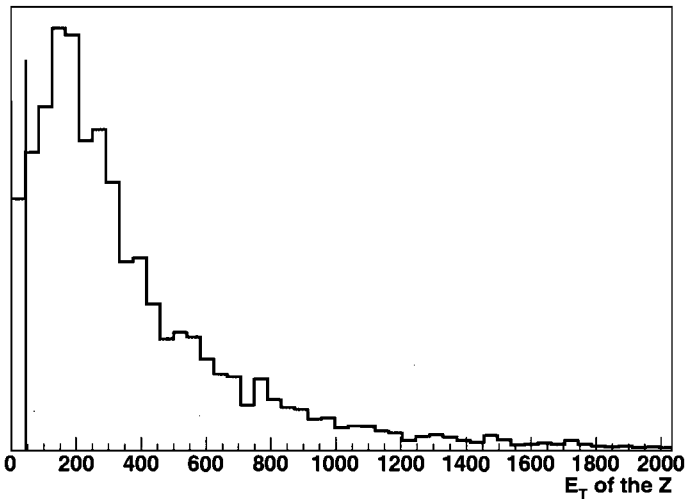

Figure 3.6: Impact of the preselection cut $E_T > 45$ GeV on the signal $qqWZ \rightarrow qqjj\ell\ell$, $m = 500$ GeV. On this plot we see the E_T distribution of the Z at parton level.

- $jjZZ \rightarrow jj\nu\nu\ell\ell$ with a pair of jets (quark or gluons):
  This process was produced with MADGRAPH, but the decay of the vector bosons was performed by PYTHIA. The cross section shown in Table 3.I is for non-hadronic decay of the Z's, with the following filter:
  - We require two leptons with $p_T > 5$ GeV and $|\eta| < 2.8$. The filter is applied at the PYTHIA step which deals with the decay of the vector bosons. Whenever a decay of a Z has taken place, not respecting these filter cuts, then the given event is not sent to the subsequent steps of simulation, digitalization and reconstruction.

  Additional preselection cuts were applied in this case as follows:
  - $E_T(W) > 45$ GeV and $E_T(Z) > 45$ GeV. These preselection cuts are the same as those applied on the background $jjWZ \rightarrow jj\ell\nu\ell\ell$. The distribution

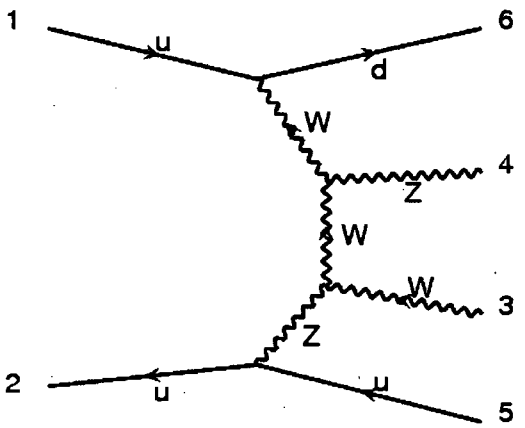

Figure 3.7: Sample of typical Feynman diagram for $jjWZ$ final state. This one corresponds to one of the 5176 SM diagrams that have to be included for this process. One can identify the two vector bosons in the final state that can mimic the signal plus the two partons that will become jets.

shown in Fig. 3.6 applies here as well.

An example of a Feynman diagram involved in the matrix element calculation is shown in Fig. 3.8.

- $W/Z + 3$ jets and $W/Z + 4$ jets:

  They constitute backgrounds for the cases of high mass and lower mass resonances respectively since, in the former case, we expect that most of the vector bosons which decay hadronically will be reconstructed as a single jet. This process was produced with MADGRAPH setting $m_h = 100$ GeV as explained in section 3.2.1.1. We required $\Delta R_{jj} > 0.4$ (where $\Delta R = \sqrt{\Delta\Phi^2 + \Delta\eta^2}$) in order to have well separated jets. This will reduce phase space overlap with parton shower. It was verified that $W \rightarrow jj$ is not affected by this requirement for the resonance cases studied here. Only $W^+ + n$ jets were simulated (where $n = 3, 4$). To take into account $W^- + n$ jets, we evaluated its cross section (also with MADGRAPH) and applied a correction factor of 1.38 to the W^++jets cross sections. The decay of the vector bosons was performed with PYTHIA.

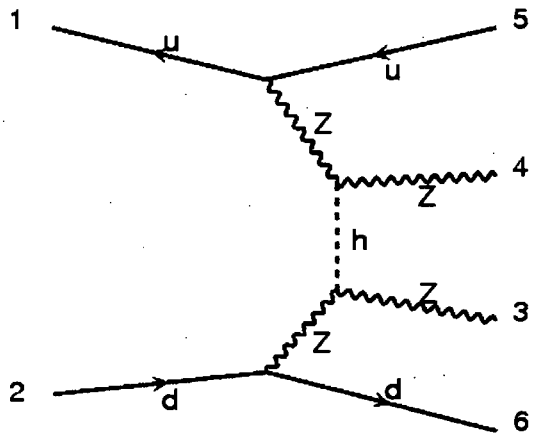

Figure 3.8: Sample of typical Feynman diagram for $jjZZ$ final state. The total number of SM diagrams for this process is 6616.

These datasets include all tree-level diagrams leading to W+4j, Z+4j, W+3j and Z+3j, with the vector bosons decaying leptonically, but due to MC production issues (huge amount of CPU time specially for $W, Z + 4$ jets) we separated them into different groups of diagrams.

In the case of $W/Z + 4$ jets, we produced separately diagrams containing vertices of the type $(\alpha_s^4, \alpha_{ew}^1)$ as shown in Fig. 3.9(b). We also produced diagrams containing $(\alpha_s^2, \alpha_{ew}^3)$ and (α_{ew}^5) as shown in Figures 3.9(a) and 3.9(c) respectively. The sample diagrams shown were selected to demonstrate that these processes include $WZjj$ in the final state.

In the case of $W/Z + 3$ jets, we find diagrams with $(\alpha_s^3, \alpha_{ew}^1)$ as shown in Fig. 3.11(b) and diagrams with $(\alpha_s^1, \alpha_{ew}^3)$ as in Fig. 3.11(a).

To keep the cross-section manageable, preselection cuts were applied at MADGRAPH level.

For the $W, Z + 4$ jets case we used the following cuts:

- We tagged the highest rapidity jet (fjet), backward jet (bjet) and 2 central jets by requiring that $|\eta_{fjet}| > 1.5$, $|\eta_{bjet}| > 1.5$. The rapidity of the partons from

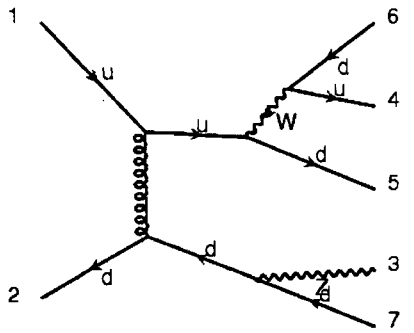

(a) $Z + 4$ jets $(\alpha_s^2, \alpha_{ew}^3)$. Total of 157008 diagrams.

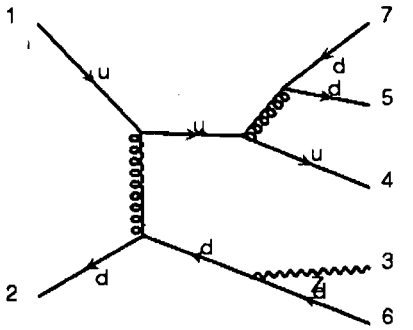

(b) $Z + 4$ jets $(\alpha_s^4, \alpha_{ew}^1)$. Total of 46392 diagrams.

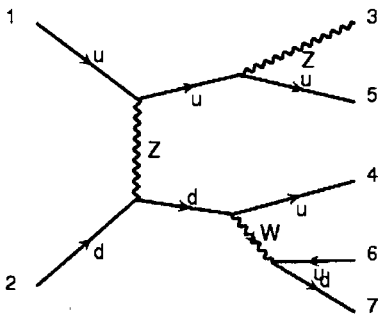

(c) $Z + 4$ jets (α_{ew}^5). Total of 50284 diagrams.

Figure 3.9: $Z + 4$ jets background. Sample of typical Feynman diagrams.

the initial state which will produce the forward jets is shown in Fig.3.13(a) for the signal $qqWZ \rightarrow qqjj\ell\ell$, $m = 500$ GeV.

- The forward and backward jet candidates were required to be in different hemispheres: $\eta_{\text{fjet}}\eta_{\text{bjet}} < 0$. This ensures that we are preferentially selecting jets coming from the initial state, to find the couple (fjet, bjet). In Fig. 3.13(b) we can see that most of the tagged forward jets are separated in different hemispheres.
- At least one forward jet must have energy $E > 300$ GeV. In Fig. 3.13(c) we show the energy of the forward and backward tagged partons from the initial state. We also require that the invariant mass of the combined forward jets

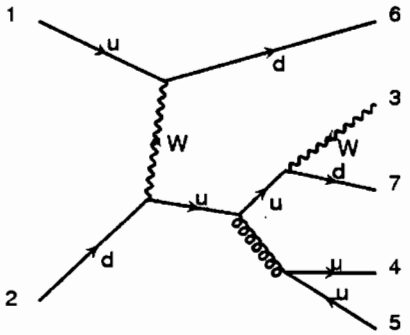

(a) $W + 4$ jets $(\alpha_s^2, \alpha_{ew}^3)$. Total of 102208 diagrams.

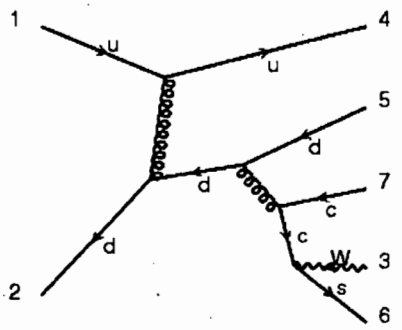

(b) $W+4$ jets $(\alpha_s^4, \alpha_{ew}^1)$. Total of 25664 diagrams.

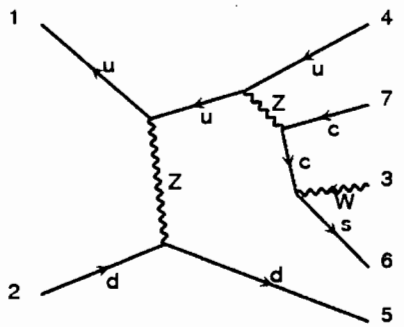

(c) $W + 4$ jets (α_{ew}^5). Total of 38048 diagrams.

Figure 3.10: $W + 4$ jets background. Sample of typical Feynman diagrams.

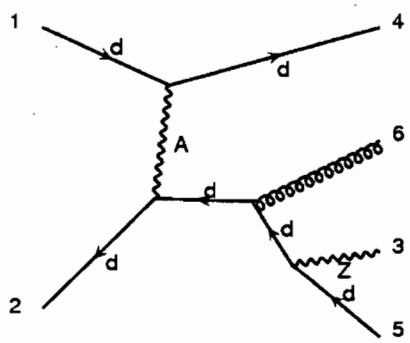

(a) $Z + 3$ jets $(\alpha_s^1, \alpha_{ew}^3)$. Total of 7424 diagrams.

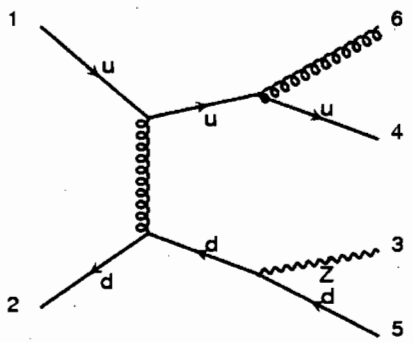

(b) $Z + 3$ jets $(\alpha_s^3, \alpha_{ew}^1)$. Total of 3252 diagrams.

Figure 3.11: $Z + 3$ jets background. Sample of typical Feynman diagrams.

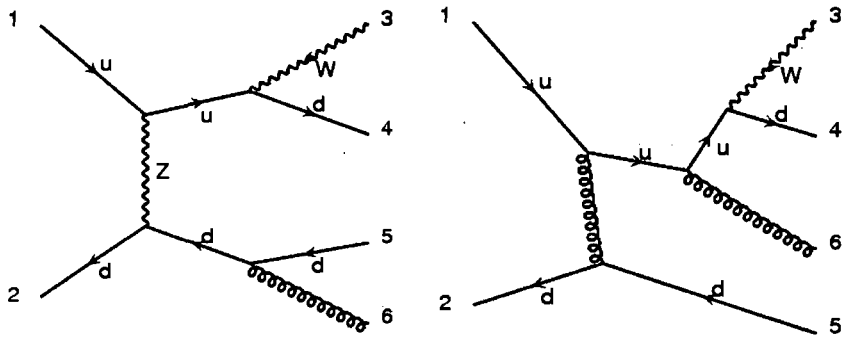

(a) $W+3$ jets $(\alpha_s^1, \alpha_{ew}^3)$. Total of 5148 diagrams.

(b) $W+3$ jets $(\alpha_s^3, \alpha_{ew}^1)$. Total of 1848 diagrams.

Figure 3.12: $W+3$ jets background. Sample of typical Feynman diagrams.

be $m_{jj} > 250$ GeV. In Fig. 3.13(d) the combined mass of the two tagged forward and backward partons is shown.

With these preselection cuts on forward and backward jets, the background cross section was reduced by a factor 3.5, which is significant because of the very large cross section.

We applied also:

- p_T of at least one of the central jets to be $p_T^j > 50$ GeV. See Fig. 3.14(a).
- p_T of the vectorial addition of the central jets to be $p_T^{jj} > 60$ GeV. Fig. 3.14(b).
- The invariant mass of the combined central jets $m_{jj} > 60$ GeV. Fig. 3.14(c).

For the case $W, Z + 3$ jets we added the requirements:

- p_T of the W or Z boson > 200 GeV as shown in Fig. 3.15(a) for the case $qqWZ \rightarrow qqjj\ell\ell$, $m = 1.1$ TeV.
- $|\eta_{W/Z}| < 2$. Fig. 3.15(b).
- p_T of one jet (central) > 200GeV. Fig. 3.15(c).
- $|\eta_j| < 2$. Fig. 3.15(d).

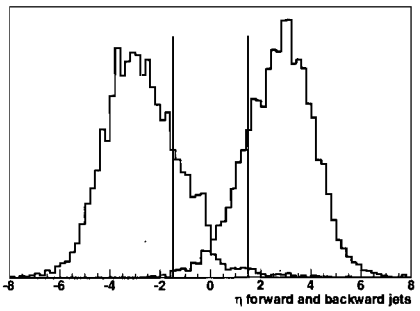

(a) Pseudo-rapidity for the initial quarks in signal events after they radiate the vector bosons. Obtained from PYTHIA before any showering or fragmentation.

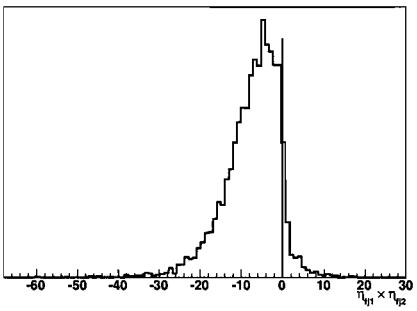

(b) $\eta_{\text{forward}} \times \eta_{\text{backward}}$ partons. Forward and backward jets must be found in different hemispheres.

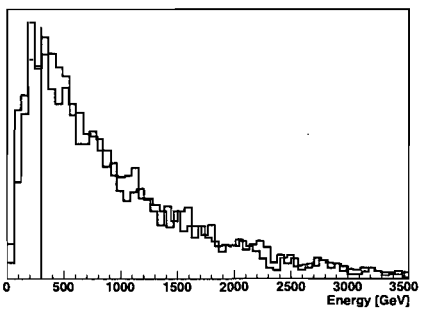

(c) Energy of tagged forward and backward initial quarks.

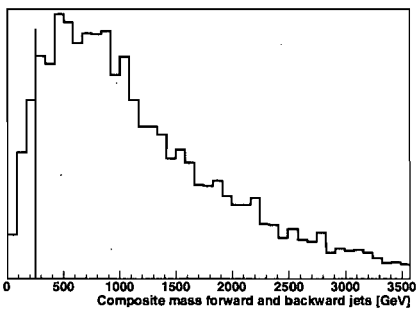

(d) Combined mass of tagged forward and backward initial quarks.

Figure 3.13: Forward and backward jets preselection cuts for $W/Z + 4$ jets background. Plots done with the signal $qqWZ \rightarrow qqjj\ell\ell$, $m = 500$ GeV.

The data produced for this work and used in the analysis studies were generated in the context of the CSC (Computing Software Challenge) exercise of the ATLAS collaboration. The CSC exercise was designed to be a joint effort of the whole collaboration to test the data production chain (see sections 2.8 and 2.9) and the analysis tools. The CSC exercise had, as a first goal, the intention to prepare the implementation of the ATLAS software to be ready before the first collisions. Between the summer of 2006 and summer 2008, all the physics groups in the collaboration requested and analyzed MC simulated data having in mind that the experiment will start at some point between 2007 and 2008 as a deadline. The data production proved to be a very complicated and painful

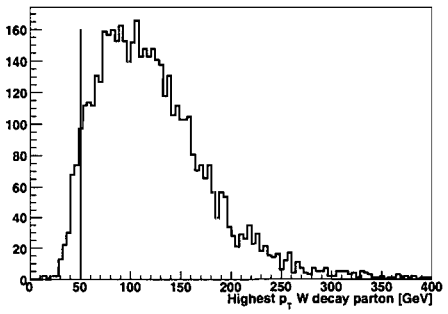

(a) Highest P_T of W decay partons.

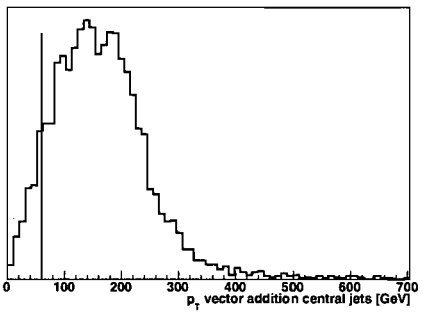

(b) p_T of the vectorial addition of the central W decay partons.

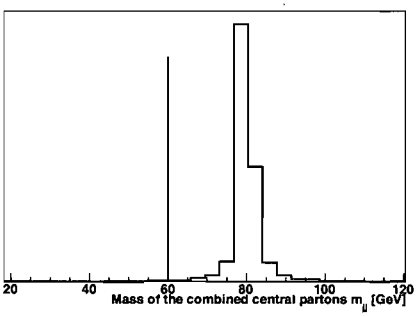

(c) Invariant mass of the combined central partons m_{qq}

Figure 3.14: Central jets preselection cuts for $W/Z+4$ jets background. Plots done with the signal $qqWZ \rightarrow qqjj\ell\ell$, $m = 500$ GeV.

effort due to the fact that the development of the production and reconstruction software lasted during all this period (and it is at the moment of writing of this thesis, still work in progress). The different stages through which our data production had to go in order to be considered official ATLAS data, were always rigorous and we contributed to the development and debugging of the software at each stage. The author of this thesis contributed to the data production as *production manager* for the Exotics Physics Group of the ATLAS collaboration.

The physics goal was to study suitable signals with the ATLAS detector, before real data would come available. CSC data are, of course, simulated data, and for this purpose full Geant4 simulation of all signals and backgrounds (see appendix. III) has been per-

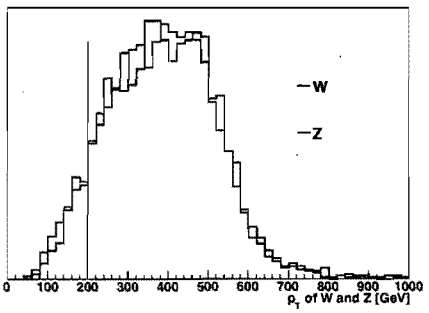

(a) P_T of W and Z.

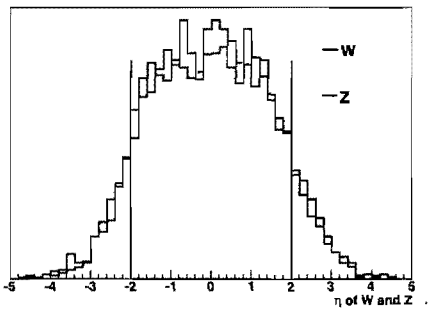

(b) η of W and Z.

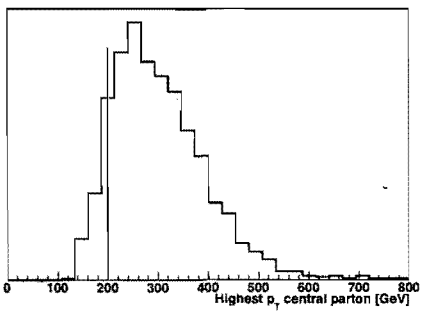

(c) Highest p_T central parton.

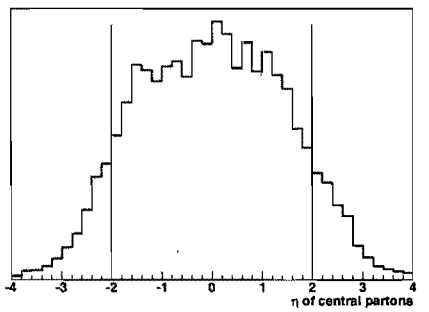

(d) η of central partons.

Figure 3.15: Preselection cuts for $W/Z + 3$ jets background. Plots done with the signal $qqWZ \rightarrow qqjj\ell\ell$, $m = 1.1$ TeV.

formed. The amount of CPU power needed for full simulation of the thousands of events used in this thesis is enormous, and were a major limitation for the statistics obtained here, specially in the case where the cross sections are quite large.

About 600000 events were full simulated for this analysis (the $t\bar{t}$ sample was common to many analyses). With an average processing time (for Geant4 simulation and particle reconstruction) of $\sim$ 20 min per event (taking into account the inhomogeneity of the different computing setups we used), this gives about 8300 CPU-days ($\sim$ 23 years with 1 CPU core !). Of course many computers where used to perform the calculation in several institutions around the planet. Part of the tests for full simulation of these data was performed in one of the clusters of the *Réseau Québécois de Calcul de Haute*

Performance at Sherbrooke[2], where we can count on about 100 machines at a time, and a virtually unlimited amount of CPU time over the year.

This CPU usage only accounts for the Geant4 simulation of the signals and the reconstruction of the calorimeter objects. The MonteCarlo production done with MADGRAPH was completely in our hands. To do so, we used exclusively the cluster (mentioned above) at Sherbrooke. We used for more than 3 months (in total) an average of 100 machines, which gives about half million CPU-hours ($\sim$ 25 years with 1 CPU core !). Additionally, there was considerable CPU time used only to run tests before the actual production finally took place.

Even with this enormous amount of events which we managed to produce, the statistics for some of the samples are insufficient. Let us take for example the case of Z+4 jets $(\alpha_s^4, \alpha_{ew}^1)$ where about 15000 events where fully simulated for this analysis (see table 3.I). The cross section times branching ratio of the Z decaying into l^+l^- $(l = e, \mu)$, for this sample, is about 2.4 pb. The number of events required for a given luminosity $\mathcal{L}$ is

$$N = \mathcal{L} \times \sigma \times Br, \tag{3.1}$$

so putting $\mathcal{L} = 100 fb^{-1}$ (about 1 year of data taking at high luminosity) gives about a quarter of a million events, only for this sample. The full statistics needed for this study are effectively impossible to reach, and in particular it was not possible within the CSC exercise due to the enormous amount of CPU time needed. In the case of the signals, which have quite low cross section, the number of events produced are sufficient. In spite of the lack of statistics for the backgrounds we expect that this study should give a good and realistic idea of what can be expected. It allows us to develop the analysis techniques needed for the search of ChL signals of VBS at high energy with ATLAS.

The study presented in this thesis is the first to be done entirely with fully simulated data, accounting for $Z + 4$ jets QCD diagrams. It constitutes a starting point for searches with real data in the years to come.

[2] `https://rqchp.ca`

3.3 Comparative studies of generators

3.3.1 Parton shower matching to matrix elements

Here, MADGRAPH was used to generate the W+jets background. A better evaluation of this background would be obtained using a generator for which W+n partons, n=0, 1, 2, 3 or 4 inclusive, are combined in a manner which avoids double counting of jets produced by the parton shower in PYTHIA. ALPGEN is one such generator (and in fact such matching is now implemented in more recent versions of MADGRAPH. See appendix II). However, due to time constraints, and in order to have a manageable size of background samples, it was not practical to use this technique. In order to validate the use of MADGRAPH, a comparison was made of the $W + 4$jets sample with an appropriate ALPGEN sample, with the same preselection cuts applied. The ALPGEN samples are not used in the final analysis since they lack sufficient statistics (samples common to all the analyses were produced with low P_T cuts).

Distributions of the vector bosons and jets were compared. As an example, the distributions for the forward jets are shown in Fig. 3.16. The overall conclusion is that the shapes of the distributions are in reasonable agreement, and therefore no great error is made in the description of the event topology by neglecting the effect of parton-shower double-counting. To the extent that such an error is made, the tag jets in the ALPGEN sample have a lower energy (leading to a depletion with respect to the MADGRAPH samples at high energies of a few %) so the backgrounds in this analysis can be considered to be conservatively over estimated.

There was a difference in the Q^2 scale used in MADGRAPH and ALPGEN. In the first case the default value of the factorization scale $Q^2 = M_W^2$ is used, and for ALPGEN $Q^2 = M_W^2 + \sum p_T^{j\,2}$. This difference leads to about a factor two in cross the section. This was confirmed by running MADGRAPH on a small sample with the same scale as ALPGEN, yielding cross-sections smaller by factors 2.05 and 1.77 for the QCD and QED processes respectively. These factors will be applied in the present analysis. Previous studies where the sensitivity to the factorization scales has been evaluated for background production have been done for example in [11, 12]. In Fig. 3.17 we see, for example, how the cross

section for $t\bar{t}j$ background changes as the factorization scale is chosen differently. Here C_1 to C_4 are different choices for the definition of Q^2. Details on the particular way of defining the scales can be found in [11]. A suitable choice may be for example $Q^2 = M_W^2$ or $Q^2 = M_W^2 + \sum p_T^{j\,2}$ as in the case of the MC generators compared in this section. We obtain the different cross sections as a function of ξ, the scale factor for the four different renormalization scale choices $\mu_R = \xi\mu_R^0$ for each C_i. The exact values of ξ, and the reason why they where chosen in this way, is not relevant for this discussion. I am only interested about showing that the cross section is sensitive to the renormalization and factorization scales, justifying why we needed to revise the MADGRAPH cross sections.

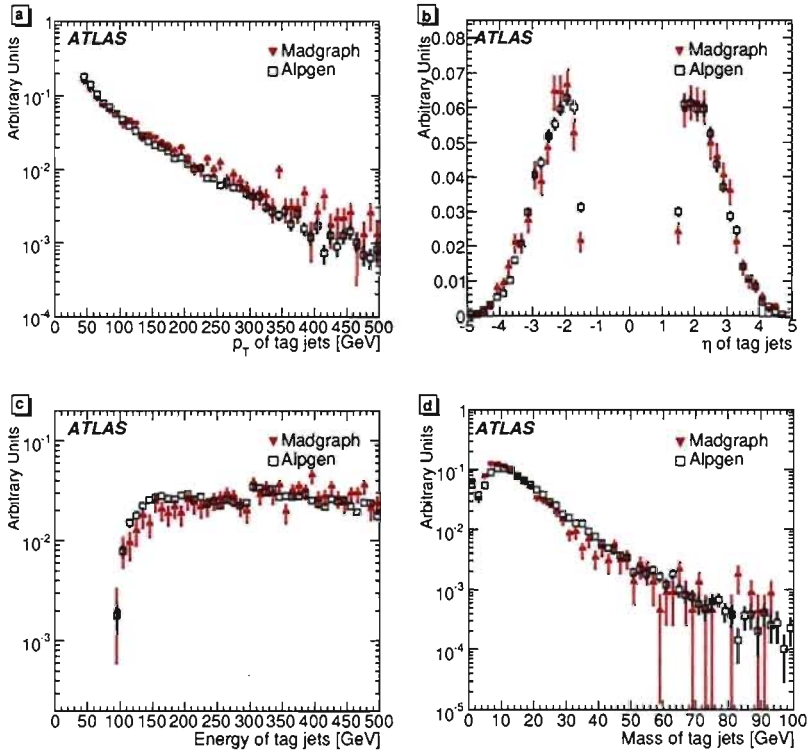

Figure 3.16: Distributions of the forward jets in the W + 4jet background for MADGRAPH (red) and ALPGEN (black) samples (area normalised). The error bars show the statistical error in each sample. Plots taken from [10].

To illustrate directly by which factors we can possibly change the cross section depending on the choice of factorization scale we show Fig. 3.18 [12]. We see for example,

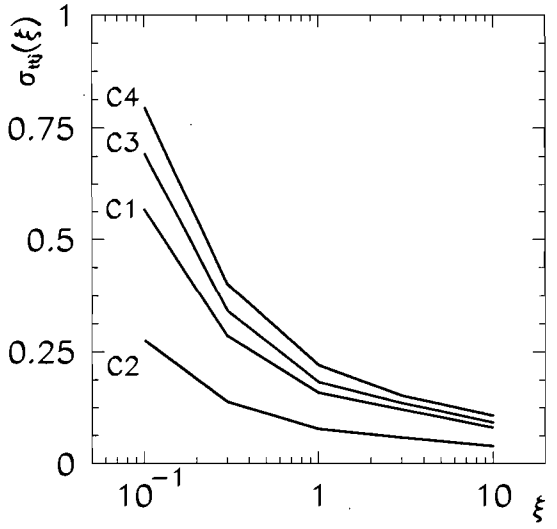

Figure 3.17: Cross section for $t\bar{t}j$ as a function ξ for four different choices of the factorization and renormalization scale [11].

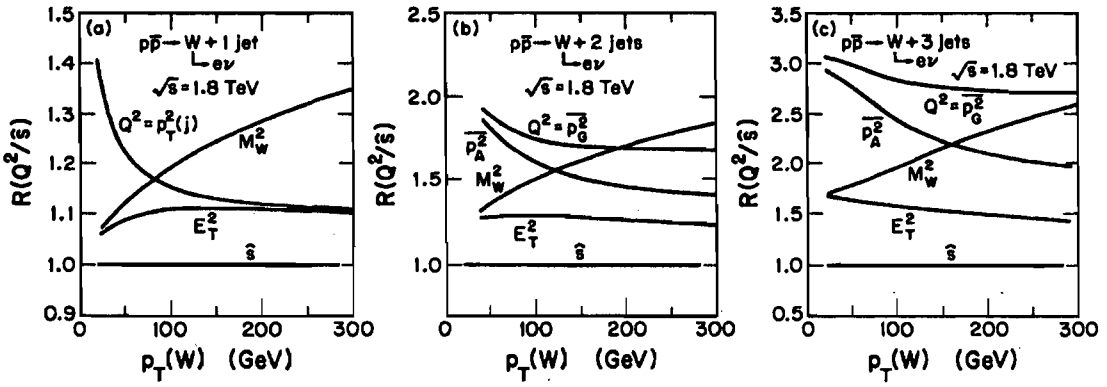

Figure 3.18: $p_T(W)$ distributions for different choices of the renormalization scale for $pp \rightarrow W + n$jets at the Tevatron [12].

for $W + 3$ jets (right plot) at the Tevatron energies, as a function of the P_T of the W, that the cross section may change by a factor up to ~ 3 when $Q^2 = \bar{p_G^2}$ (it corresponds to the geometrical average squared of the p_T of all jets in the final state). When $Q^2 = M_W^2$ the cross section increases monotonously with the $p_T(W)$.

CHAPTER 4

DISCOVERY POTENTIAL AT THE LHC

In this chapter, I present the results of an analysis, using full simulation for the ATLAS detector, of the ChL signals described previously. It should give a realistic estimate of the discovery potential of such signatures with ATLAS. The study was performed in the period between summer 2004 and summer 2008 within the Exotics Physics Group of the ATLAS collaboration. Contact with many other physics groups was also necessary involving exchange with the rest of the collaboration. The study resulted in the production of two ATLAS notes, one in 2006 [61] and another in 2008 [10].

4.1 Trigger

As a first step in the analysis, it is important to evaluate the efficiency of the basic trigger menus. Although we are going to need $10^{34}\text{cm}^{-2}\text{s}^{-1}$, we had access only to low luminosity trigger (10^{33} $\text{cm}^{-2}\text{s}^{-1}$) conditions at the moment this analysis was performed. The triggers chosen were based on an early menu [62] and the real physics menu is likely to be very different. However, since the signal is at relatively high p_T, and triggering on vector bosons is a high priority, this is not likely to have a large impact.

To evaluate this efficiency, we query the trigger flag in the EDM (see section 2.9) to know if the event was accepted by the trigger or not. We apply the following cuts: for electrons and muons we require single leptons to have p_T greater than the value corresponding to the threshold dictated by the trigger signature and $|\eta| < 2.5$; similarly for jets, but the pseudorapidity cut applied is $|\eta| < 3.2$. This is necessary because trigger signatures for forward jets exist separately, but unfortunately that trigger information was not available in the simulation version used for this study.

The trigger efficiency is defined as the number of times the trigger passed (with the corresponding cuts applied) divided by the number of truth events in the samples (with the same cuts applied). Here, truth jets are particle jets reconstructed with the same

algorithm as for fully simulated events.

In Table 4.I we present a detailed list of efficiencies for the signals $qqWZ \to qqjj\ell\ell$ ($m = 1.1$ TeV). The poor efficiency of the `e22i` (see Fig. 4.1, left) and `2e12i` triggers is understood to be due to the isolation criterion, which was not optimised for high energy electrons. This was common to many other analyses, and an optimised definition is now under development.

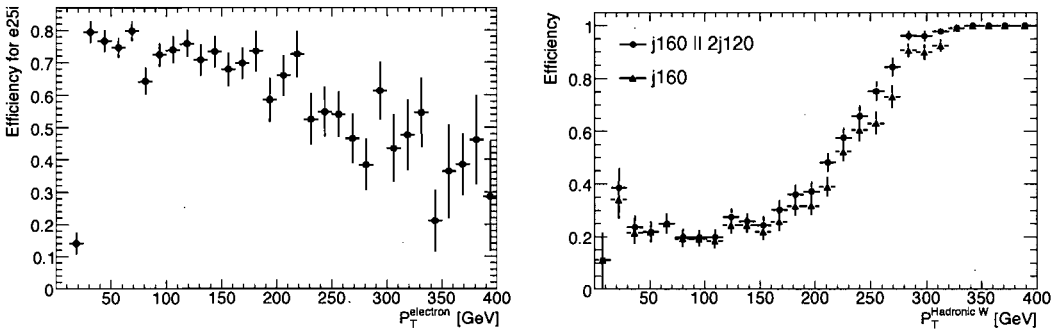

Figure 4.1: Left: efficiency of the `e22i` trigger as a function of the p_T of electrons from the true leptonically-decaying W boson. Right: efficiency of the `j160` trigger (black triangles) as a function of the p_T of the true hadronically-decaying W boson. Also shown with blue circles is the efficiency when the `j160` and `2j120` triggers are logically OR'ed.

It is worth mentioning that the efficiency for the `2j120` trigger (Fig. 4.1, right), which requires two jets with $p_T > 120$ GeV suffers partly from the fact that the two jets from the vector boson decay are merged due to the boost as described in Section 4.2.1. It is also significantly higher for events with true electrons than for those with true muons, probably because the electrons themselves are also reconstructed as jets in the calorimeter.

Finally, various combinations of the trigger signatures might be explored in the future to improve the efficiency. For instance, the `e60` trigger might be used in conjunction with the `e22i` to compensate the low efficiency of the latter for high-momentum electrons (Fig. 4.1). Likewise, the `2j120` trigger might be used together with `j160`, since the efficiency of the latter drops significantly when the hadronically-decaying vector boson has $p_T < 300$ GeV and decays into two distinctly resolvable jets.

	WZ signal	
Trigger Signature	**Cut Loss**	**Efficiency**
Electrons		
`2e12i`	13%	36%
`e22i`	1%	78%
`e60`	5%	82%
Muons		
`mu6`	5%	95%
`mu20`	5%	92%
Jets		
`2j120`	67%	73%
`j160`	34%	96%

Table 4.I: Table of high-level trigger efficiencies for $qqWZ \rightarrow qqjj\ell\ell$ ($m = 1.1$ TeV). The "Cut Loss" columns indicate the fraction of true events that would be lost by applying the p_T requirements of each trigger signature on the true electrons, muons and jets. Since such events are unlikely to satisfy the trigger conditions, they are not taken into account when the trigger efficiencies are evaluated.

For all the signals studied in this thesis, the trigger efficiency after the event selection procedure was found to be essentially 100% in all cases, meaning that the trigger system will respond to the events we are able to select using the cut-based analysis proposed in this work.

4.2 Reconstruction Challenges

In this section, we focus on those parts of the reconstruction which are most particular to vector boson fusion at high masses. We discuss the following:

- Reconstruction of hadronically-decaying vector bosons. In our regime these typically have high p_T and the decay products are very collimated.
- Leptonically decaying vector bosons. These require good lepton and $\not{E}_T$ measurement, but the challenges here are not unique to these channels.
- Forward 'tag' jets. Measuring jets close to the edge of the detector rapidity ac-

ceptance is a challenge in common with low mass Higgs searches in vector boson fusion.

- Central jet veto. Since the vector boson scattering process involves no colour exchange between the protons, a suppression of QCD radiation is expected. This can be used to distinguish between signal and background, but is sensitive to underlying event and pile-up.

4.2.1 Hadronic Vector Boson Identification

At lower masses and p_T, the hadronically decaying vector bosons are identified as dijet pairs. However, for events where a hadronically decaying vector boson is highly boosted, the decay products are often collimated into a single jet. Cuts such as a dijet invariant mass window are no longer applicable in this scenario, but a single jet mass cut can be used.

The single jet mass is defined as the invariant mass evaluated from the 4-vectors of the constituents of the jet. In the ATLAS detector, these constituents are at present calorimeter objects, either topologically defined clusters with some local hadronic calibration, called here *topoclusters*, or calorimeter towers (see appendix I for details). For jets containing the decay products of a boosted vector boson, this single jet mass is near the mass of the parent boson. For light quark and gluon jets this mass is generally much lower. Since the background for hadronic vector boson identification is so severe, further cuts may be applied on the subjet structure of the candidate jet.

In addition, the transition between the dijet and single jet case as p_T increases needs to be dealt with. One can proceed dynamically selecting the appropriate method. To do this, we first look at the highest p_T jet. If this passes the mass window cut, then the single jet selection is applied, as described below. If it does not, then combinations of jet pairs in the event are considered. The vector boson is still expected to be the highest p_T hadronic system, so the p_T of all jet pairs is evaluated, and the highest p_T pair is taken to be the vector boson candidate. A mass window cut (dependent upon the jet algorithm) is then applied to this pair. For the analysis presented in this work we looked separately

at both cases, jet-pair and single jet W-hadronic decay. It was not used in the end for the cone jet analysis (see below), as it was found that better statistical precision could be achieved by analysing both cases separately before combining the results. However a dynamical selection, combination of both searches is suitable thinking about the future when studying real data. In section 4.3.1.5 we discuss the results using the $k_\perp$ algorithm and dynamical analysis performed by the UCL group [10], compared to our results with a cone algorithm. We find that the approaches are compatible.

4.2.1.1 $k_\perp$ Algorithm

Although the jet algorithm used for jet identification, in my personal contribution to this work, is the *Cone* algorithm (as explained in Appendix I), vector boson scattering including WW resonances and leptonic channels on WZ resonances, was performed in collaboration with the UCL group (as mentioned in section 3.1) who used the $k_\perp$ algorithm. We present here briefly the main characteristics of that analysis.

The $k_\perp$ algorithm is run with an R-parameter (which determines the "jet size") of 0.6 where a variation in R, i.e. ΔR, is defined as $\sqrt{\Delta\Phi^2 + \Delta\eta^2}$. The algorithm basically merges pairs of constituents (groups of calorimeter cells for example) to build up a jet. It is described in [63][64][65] and briefly summarized in Appendix I.

The $k_\perp$ analysis uses the dynamic selection technique described above (previous section) to decide whether to use a dijet or a single jet for the vector boson candidate. The fraction of vector bosons reconstructed as a single jet, as a function of p_T of the vector boson candidate, is given in Fig. 4.2. The transition between dijet and single jet takes place between $p_T = 200$ and 300 GeV for this algorithm.

Single jets

The resolution of the single jet mass for the $k_\perp$ algorithm has been evaluated for both detector simulations (full and fast. See appendix III.) for several samples. For the sample with a resonance at $m = 1.1$ TeV (Fig. 4.4 left) for example, the W boson singlet jet mass resolution was found to be $9.2 \pm 0.2\%$.

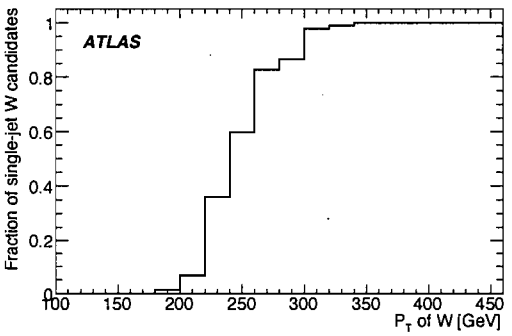

Figure 4.2: Fraction of W boson candidates reconstructed from a single jet, as a function of the transverse momentum of the reconstructed vector boson, for the WW $m = 1.1$ TeV signal sample.

The $k_\perp$ merging is intrinsically ordered in scale, making the final merging the hardest. The algorithm provides a y value for this final merging, which is a measure of the highest scale at which a jet can be resolved into two subjets. The y value can be converted into a "Y scale" in GeV using the relation Y scale $= E_T \times \sqrt{y}$, where E_T is the jet transverse energy. This Y scale is expected to be $\mathcal{O}(m_V/2)$ (where m_V is the mass of the vector boson) for boosted vector boson jets, and much lower than E_T for light jets [66]. At the truth and fast-simulation levels this variable has been shown to have discriminating power even after a single jet mass cut [13, 15, 66, 67]. The splitting scale ("Y scale") and the y value distribution are shown in Fig. 4.3. We see the separation between QCD jets and W jets for PYTHIA SUSY events, PYTHIA $W+$ jets and ALPGEN $W + 3$ jets. A cut on the jet mass at $75 < M < 90$ GeV and $p_T > 250$ GeV is applied to all jets.

The resolution of the ATLAS detector for this "Y scale" variable is presented in Fig. 4.4 (right). The resolution, for the same sample as above, is $12.3\% \pm 0.3\%$ with full detector simulation.

A mass cut around the window from $m = 68.4$ GeV to 97.2 GeV will be applied to W boson candidates, and from $m = 68.7$ GeV to 106.3 GeV for hadronic Z boson candidates reconstructed in the single jet mode. This mass window is determined by considering the resolution, the tails, and the background contamination.

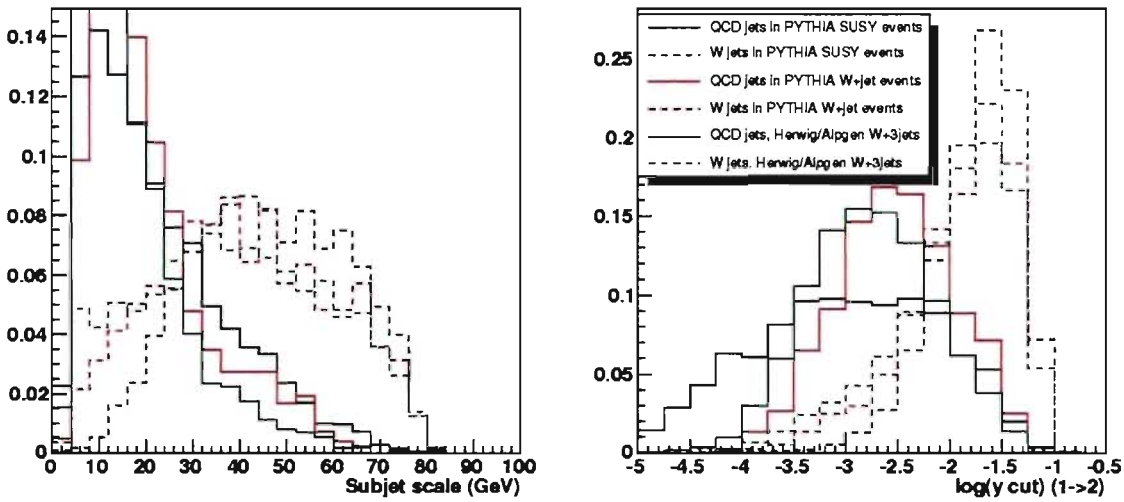

Figure 4.3: Distributions for the splitting scale (left) and the y distribution (right) for the same type of jets [13]. The histograms are normalised to unity.

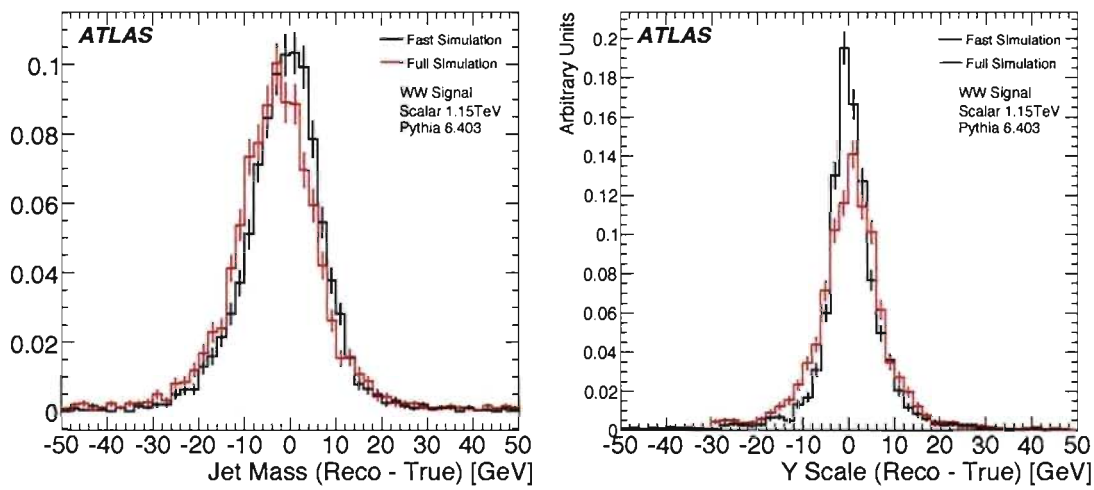

Figure 4.4: Single jet mass resolutions (left) and Y scale resolutions (right) from different detector simulations, using the $k_\perp$ algorithm. The truth is defined by running the jet algorithm on the hadronic final state of the MC generator.

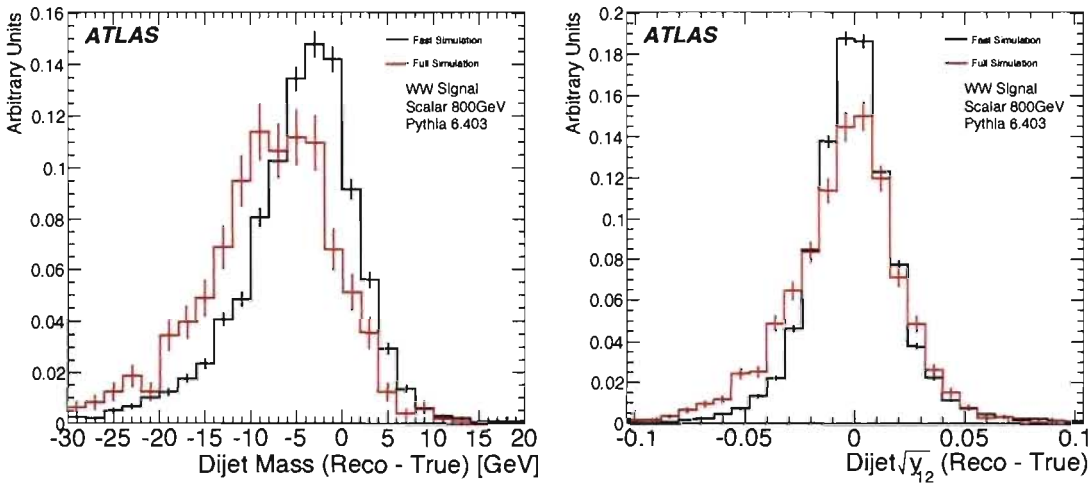

Figure 4.5: Dijet mass resolutions (left) and y resolutions (right) from different detector simulations, using the $k_\perp$ algorithm. The truth is defined by running the jet algorithm on the hadronic final state of the MC generator.

Based on the resolution, the tails, and the background contamination, a Y scale cut around the window from 30 GeV to 100 GeV will be applied to W and Z boson candidates reconstructed in the single jet mode. To evaluate the benefit of cutting on Y scale, a sample of single-jet vector boson candidates was selected in signal and background by applying a $p_T > 300$ GeV cut, motivated by Fig. 4.2, and a mass window cut. Starting from this sample, the efficiency of the Y scale cut is given in Table 4.II for full simulation. The numbers suggest that for the W+jets background, an additional rejection factor of approximately 2 is provided by the Y scale cut even after a single-jet mass cut has been applied. This is achieved with a signal efficiency of approximately 80%.

	1.1 TeV Vector Resonance	W+4 jets	$t\bar{t}$
Jet Mass	68%	14%	28%
Y Scale	77%	29%	63%

Table 4.II: Efficiency of the Y-scale cut in the 1 jet case for full simulation.

	800 GeV Scalar Resonance	W+4 jets	$t\bar{t}$
Jet Mass	17%	6%	14%
Y Scale	79%	48%	84%

Table 4.III: Efficiency of the Y-scale cut in the 2 jet case for full (fast) simulation.

Dijet mode

A variable analogous to y may be calculated, using the relative p_T of the dijets. This variable is required to be in the range $0.1 < \sqrt{y} < 0.45$. The efficiency is shown in Table 4.III.

A mass cut around the window from $m = 62$ GeV to 94 GeV will be applied to W boson candidates, and from $m = 66.6$ GeV to 106.2 GeV for hadronic Z boson candidates reconstructed in the dijet mode.

The mass and y windows are again determined by considering the resolution, the tails, and the background contamination.

The resolution of the dijet mass and the y variable for dijet vector boson candidates are shown in Fig. 4.5. The resolution for the full simulation is found to be approximately 5% for the mass and 5% for the y variable.

4.2.1.2 Reconstruction of hadronic W with Cone algorithm

The problem of the two jets from a boosted hadronically decaying vector boson merging into a single jet has also been studied for jets reconstructed using the cone algorithm (see appendix I for details). With this algorithm, jet reconstruction starts from *seeds* i.e. constituents (clusters) with $p_T > 1$ GeV. The algorithm collects all constituents around a seed within $\Delta R = \sqrt{(\Delta\eta)^2 + \Delta\phi)^2} < R_0$ (where R_0 can be, for instance 0.4) and adds their momenta vectorially. Then it repeats the procedure over the collection around the direction of the sum, and computes a new sum. It continues repeating this operation until the resulting sum direction is stable.

Figure 4.6 shows an example of W boson reconstruction using this algorithm for the jet-pair case ($m = 500$ GeV resonance) and single jet case ($m = 800$ GeV resonance). A cone size of 0.8 is used for selecting a single jet W boson and 0.4 for the case of a jet

pair. There is a small difference in the W boson mass peak reconstruction for the two cases. The jets chosen for this selection have a minimum p_T cut of $p_T > 20$ GeV, and those overlapping with electrons have been removed. The low-mass tail, for the case of reconstruction with a single jet (800 GeV) is due to the fact that in this sample there are also cases where the W can be reconstructed as two jets. In those cases we are not testing if such reconstruction is better and an incorrect candidate, with a single jet, is selected. This tail will be, of course, cut off before reconstructing the resonances. Additionally, the case of 800 GeV with double jet reconstruction is also presented in this work.

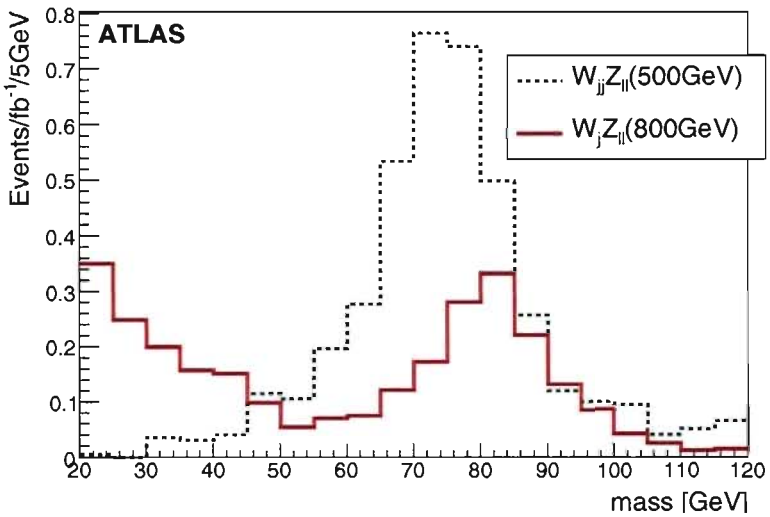

Figure 4.6: Reconstructed W boson for cases where it forms two separated jets (500 GeV) and a single jet (800 GeV). The samples used are the $m = 500\,\text{GeV}$ resonance (in green) and $m = 800\,\text{GeV}$ resonance (in red).

Single jet hadronic W boson candidates are identified with the highest p_T object in the central region, after having removed overlaps with all electrons in the event within a ΔR of 0.1 (electrons can fake jets). A mass cut in a window around the reconstructed W boson mass will be applied.

The exploration of the substructure of a wide jet (typically of size 0.8) is done by searching for 2 narrow jets (size $\sim$ 0.2) fitting within the big jet. Various variables can then be studied, among which are the energy ratio of the narrow jets, their invariant mass,

the distance ΔR between the leading narrow jet and the wide jet, or the momentum component of this narrow jet transverse to the wide jet direction. The latest variable, called $p_{T\text{nj}}$, is illustrated in Fig. 4.7 where we show schematically a couple of narrow jets fitting inside a wide jet. The discriminating power is illustrated for the $WZ \to \ell\ell jj$ channel (1.1 TeV resonance) and its principal background in Fig. 4.8, which shows the latter variable (called here 'p transverse') versus the invariant mass reconstructed from two narrow jets. Cutting in the (p_T, invariant mass) plane gives results comparable to those obtained with the Y scale method above, as illustrated in Table 4.IV. Similarly, Fig. 4.9 shows the p_T versus ΔR between the leading narrow jet and the wide jet.

4.2.2 Leptonic Vector Boson ID

All the signals studied in this thesis involve at least one leptonic vector boson decay. This is essential because of the very large QCD background.

4.2.2.1 Electron identification

Electron objects are selected according to the *medium* definition [68]. Two algorithms are used to reconstruct electrons. The main (or standard) one is dedicated mostly to high p_T isolated electrons. It is seeded by a cluster (group of activated cells overcoming a certain threshold) reconstructed in the electromagnetic calorimeter. The second is dedicated (mostly) to low p_T electrons. It is seeded by a track in the Inner Detector. Both algorithms reconstruct the same "Electron" object. For each electron candidate, we require it to pass a series of cuts based on the shower shape properties in different

	Signal 1.1 TeV	Z+3 jets (QED)	$t\bar{t}$, high p_T
Input events	27750 (100.0%)	8750 (100.0%)	20000 (100.0%)
$p_T(\text{leadingjet}) > 150$ GeV	10052 (36.2%)	1006 (11.5%)	1911 (9.6%)
Subjet selection	6913 (68.8%)	169 (16.8%)	726 (38.0%)

Table 4.IV: Comparison of efficiencies for the jet sub-structure selection for a typical signal and backgrounds. The jet is required not to overlap with an electron, and in the subjet selection, we require 2 small jets with $p_T > 15$ GeV and invariant mass > 60 GeV (see text).

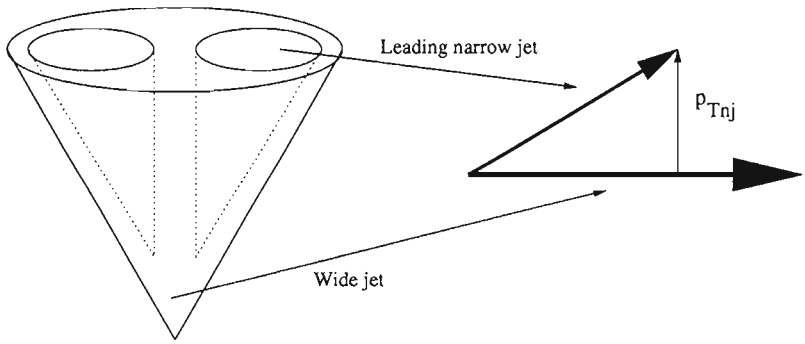

Figure 4.7: Scheme (not to scale) of two narrow jets fitting inside a wide jet. The observable: momentum of the leading narrow jet orthogonal to the wide jet direction, is tagged as p_{Tnj} in the figure.

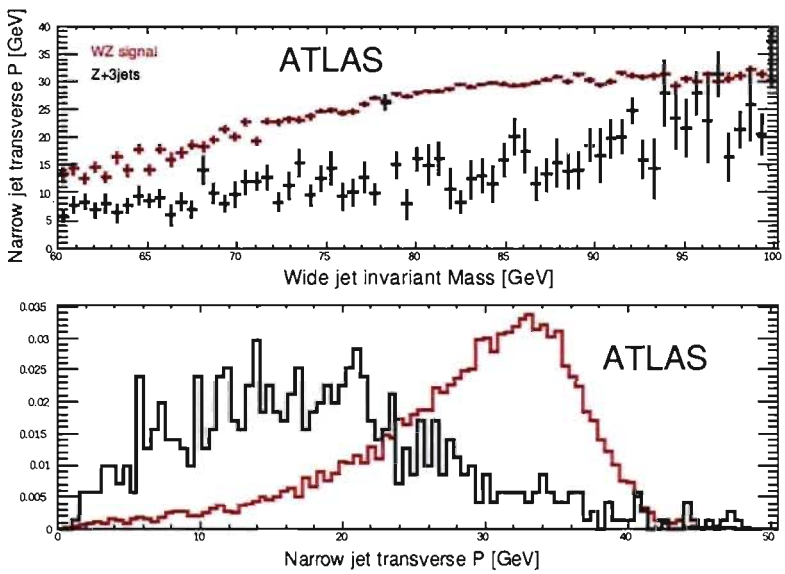

Figure 4.8: Profile histogram of the momentum of the narrow jet orthogonal to the wide jet direction vs the invariant mass of the wide jet, for W boson hadronic decay of the resonance signal $qqW_{jj}Z_{\ell\ell}$ of $m = 1.1$ TeV (red) and for Z+3 jets sample (black). Lower graph : normalized distributions of narrow jet orthogonal momentum.

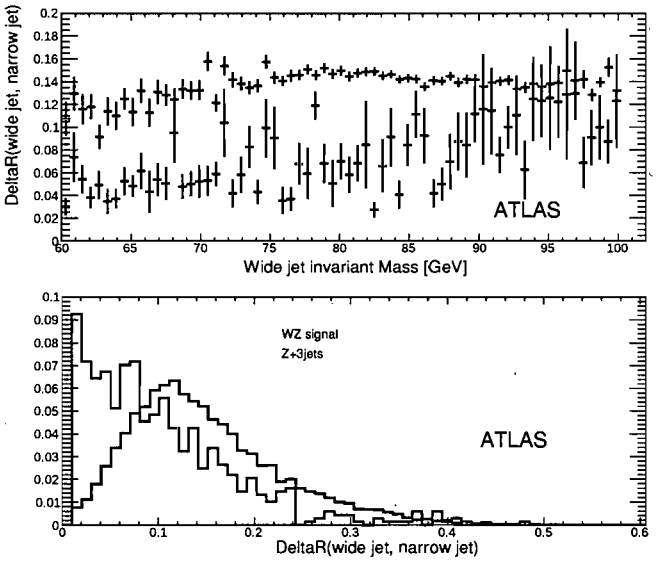

Figure 4.9: Profile histogram of the distance (narrow jets, wide jet) versus the invariant mass of the wide jet, for W boson hadronic decay of the resonance signal $qqW_{jj}Z_{\ell\ell}$ of $m = 1.1$ TeV (red) and for Z+3 jets sample (black). Lower graph : normalized distributions of distance (narrow jets, wide jet).

compartments of the calorimeter as well as variables combining ID and Calorimetry information. If a cut passes, then a bit is set in a flag called `isEM`. This variable is a means of representing all together a number of criteria to evaluate the quality of reconstruction of an electron candidate. It is possible to make certain definitions by choosing which cuts one requires an electron to satisfy. In table 4.V, I present a list of properties in the `isEM` variable and three standard definitions adopted by the ATLAS collaboration: *loose*, *medium* and *tight* electrons. In table 4.V the properties are as follows:

- Cluster η range is a cut in pseudorapidity: $|\eta| < 2.47$.
- Cluster hadronic leakage: a cut in the energy deposited in the hadronic calorimeter for a particular track.
- Cluster isolation: when it is required, a given track needs to be isolated in a certain ΔR distance to other objects in the calorimeter.
- Track in Pixel or SCT: when it is chosen we require the particle to leave a track in

the inner detector.

- Track matching η in Calo: here we force the direction of the track in the inner detector to match the direction of the energy deposition in the calorimeter.
- Track matching ϕ: ID track matches ϕ direction in the calorimeter.
- Ratio of the energy threshold and momentum: E/p should be close to 1.
- TRT identification.

4.2.2.2 Muon identification

Muons are selected according to the *STACO* [68] reconstruction algorithm. The STACO method is the statistical combination of two independent measurements done in the inner detector and the muon spectrometer. Initially, a track combination is tried only for pairs of tracks that show a reasonable matching in the (η, ϕ) plane. Then the track combination is accepted only if the global χ^2 (of a fit between the two tracks) is below a maximal value. When different combinations are possible, a simple algorithm has been applied to solve the ambiguities. The pair giving the best combined χ^2 is retained and the corresponding tracks are removed from the initial samples of the tracks to be combined. The same procedure is then applied until no more combination is possible.

Property	*loose*	*medium*	*tight*
Cluster η range	1	1	1
Cluster hadronic leakage	1	1	1
Cluster isolation	0	0	1
Track in Pixel or SCT	0	1	1
Track matching η in Calo	0	1	1
Track matching ϕ	0	0	1
Ratio E/p	0	0	1
TRT	0	0	1

Table 4.V: Summary of variables for electron identification. 1 means a given electron candidate satisfies the property, and 0 means it did not.

4.2.2.3 Lepton reconstruction efficiencies

Fig. 4.10 and Fig. 4.11 show the efficiency for W daughter leptons. The results for different electron selection criteria are given. The loss of efficiency occurs in the forward regions, near the limits of the tracking detectors and at p_T values close to the applied cut, due to migrations over the cut between trigger and offline reconstruction. The efficiencies for the leptonic Z channels have been found to be similar. It is important to say here that the efficiencies presented are substantially low, and a better electron and muon identification is expected from the ATLAS detector. At the time of writing this thesis, already a lot of improvement was done in the identification and analysis software. It is therefore likely that the results obtained in the subsequent analysis are conservative.

4.2.2.4 Leptonic Z Reconstruction

The Z candidates are reconstructed from pairs of e^+e^- or $\mu^+\mu^-$. For the case of a WZ resonance of mass 800 GeV, taken as reference here, in the electron case, the resolution is about 2.7 GeV as is shown in Fig. 4.12a, suggesting a mass window selection between 85 GeV and 97 GeV for m_{ee}. In the case of muons, the resolution for the Z mass reconstruction is 3.6 GeV (see Fig. 4.12b), so the mass requirement is loosened to be between 83 GeV and 99 GeV. Furthermore, to reduce the backgrounds (particularly the background from $t\bar{t}$ events, the P_T of one of the leptons is required to be at least 50 GeV, and the other to be at least 35 GeV. In the unlikely case that more than one combination of leptons satisfy all these requirements, we choose the composite $Z_{l^+l^-}$ with the mass closest to the actual Z mass.

4.2.2.5 Leptonic W Reconstruction

The W boson reconstruction uses the transverse components of the missing 3-momentum of the highest-P_T lepton (e or μ) in the event. For the signal, after reconstruction of the hadronic vector boson candidate, the highest p_T lepton corresponds to the lepton from the W decay in 96% of cases. Attributing the missing momentum to the neutrino, and taking the nominal W mass (80.42 GeV) as a constraint, a quadratic equation is obtained

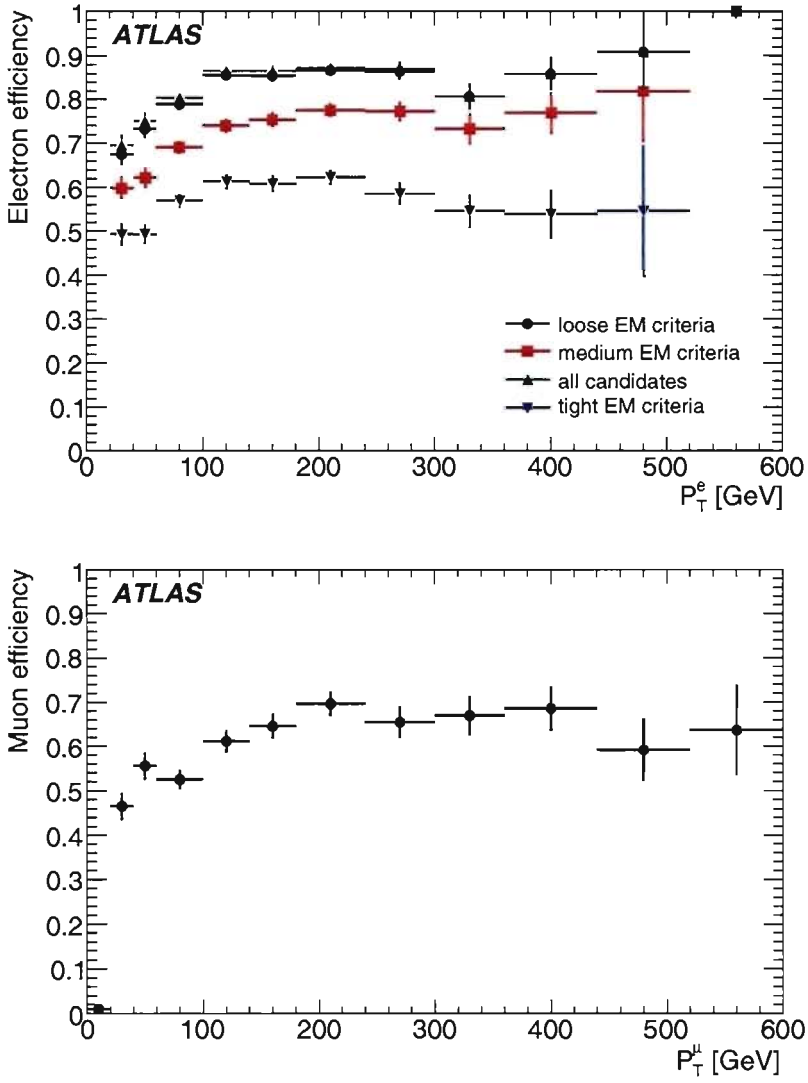

Figure 4.10: Efficiency of reconstructing and identifying W-daughter electrons (top) and muons (bottom) as function of true lepton momentum. The electron plots show the efficiency for 4 different electron selection criteria: All electron objects (green), isEM loose (black circles), isEM medium (red squares), isEM tight (blue triangles).

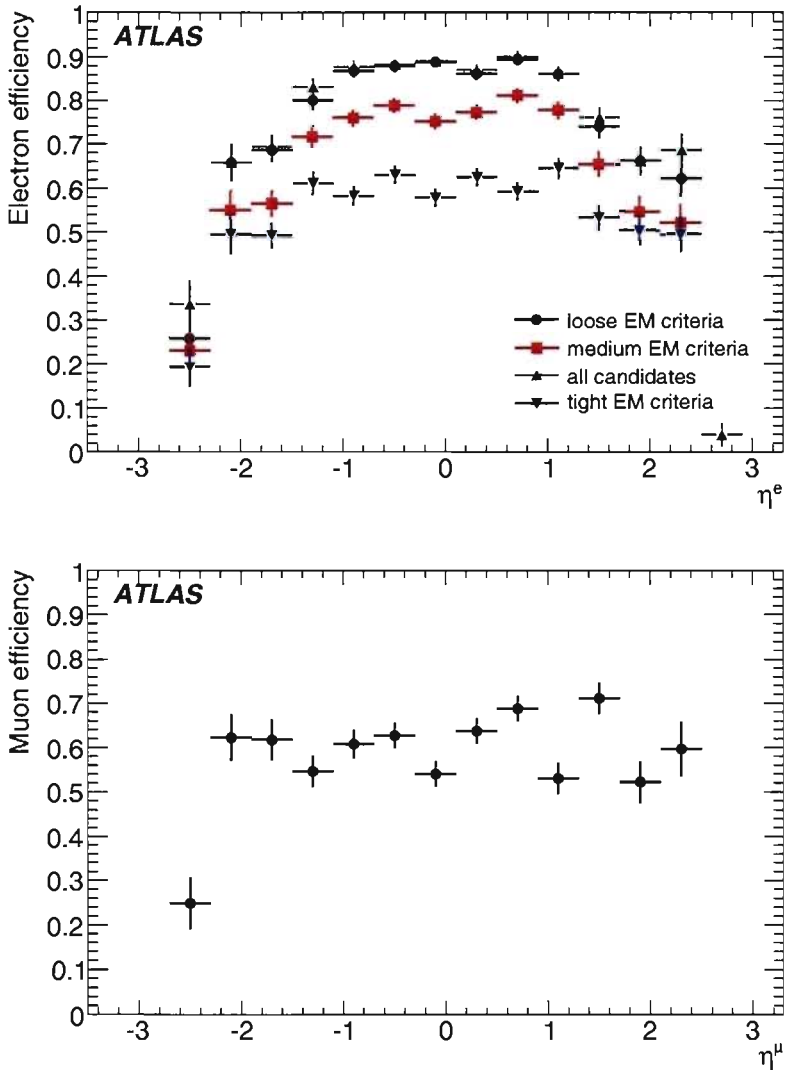

Figure 4.11: Efficiency of reconstructing and identifying W-daughter electrons (top) and muons (bottom) as function of true pseudo-rapidity. The electron plots show the efficiency for 4 different electron selection criteria: All electron objects (green), isEM loose (black circles), isEM medium (red squares), isEM tight (blue triangles).

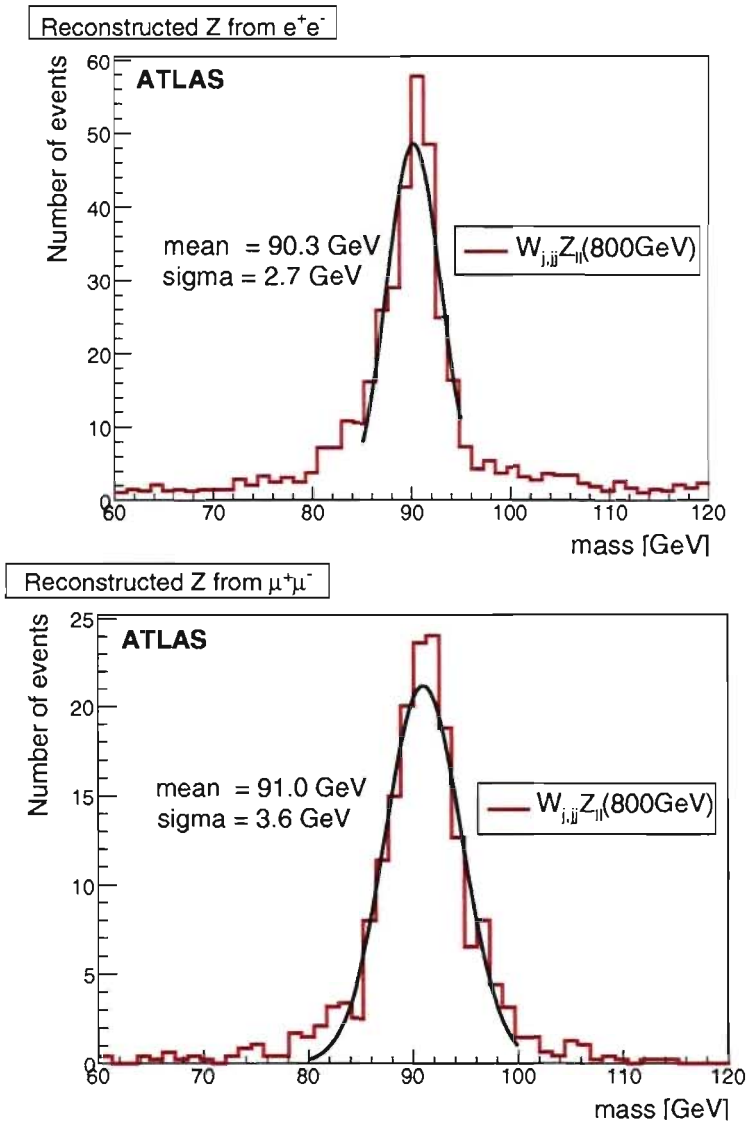

Figure 4.12: Reconstructed Z from electron pairs (top) and muon pairs (bottom).

for the z-component of the neutrino's momentum. The z component is required in order to reconstruct the diboson mass in the final analysis. Only events for which at least one real solution exists for this quadratic equation are retained. When there are two possible solutions, the W reconstructed with the higher p_T is chosen.

4.2.3 Tagged Forward Jets

Many different strategies are possible for implementing a tag-jet selection. A number of these were compared, and the best rejection factors for a given efficiency were obtained as follows:

1. Require two jets with
   - $|\eta(jet)| > \eta_{\text{cut}}$ and $p_T(jet) > p_{T\text{cut}}$ GeV.
   - opposite signed rapidity
   - at least one of them has an energy greater than a critical value E_{cut} GeV
2. If more than one jet with the same sign rapidity satisfies the above cuts, choose the most energetic, labelled FJ1. The next one is labelled FJ2.
   - Require the tag-jet with the opposite sign of rapidity to satisfy $\Delta\eta(FJ1, FJ2) > \Delta\eta_{\text{cut}}$ and $E(FJ2) > E_{2\text{cut}}$ GeV.

In addition a dijet mass cut is currently applied in the cone algorithm analyses. The specific values of the cuts in each case are to be optimised depending upon the kinematic region under study. The exact cut values will be presented in the section 4.3.

Other prescriptions to tag forward jets can be used as done for example in the $H \rightarrow \tau\tau$ channel [69] with SM higgs, where they use a simpler definition, by requiring

- Leading jet $p_T > 40$ GeV, $|\eta| < 5$.
- No overlap with taus.
- Forward and backward jets in different hemisphere $\eta_{j1} \times \eta_{j2} < 0$.
- They further require $|\eta_{j1} - \eta_{j2}| > 4$.

4.2.4 Central jet veto

As mentioned earlier, a useful analysis strategy to suppress backgrounds such as $t\bar{t}$ is to apply a central jet veto [46, 59, 70, 71, 72, 73]. For vector boson scattering, one expects little QCD radiation in the central region since only colourless electroweak vector bosons are produced and the forward jets are not colour connected. Given the forward jet cut definition, we unambiguously define the central region of the event as the η region between them. The central jet veto then simply requires that no other high p_T jet (here taken as $p_T > p_{T\text{cut}}$) other than those resulting from the hadronically decaying vector boson lie in the central region.

Specifically in these analyses, where it is applied the central jet veto rejects events if there are any additional jets with a chosen maximum value for $|\eta|$ and minimum value for p_T.

4.3 Event Selection

Using the tools outlined in the previous section, we now characterise the samples and outline the specific cuts applied for each final state considered.

4.3.1 $W^{\pm}Z \to jj\,\ell^{+}\ell^{-}$

This channel benefits from a very good resolution on the Z boson leptonic reconstruction, which allows good suppression of the $t\bar{t}$ background.

For the $m = 1.1\,\text{TeV}$ WZ resonance, only the case of a single heavy jet from the W boson decay will be considered as it constitutes the majority of the events. For the $m = 800$ GeV resonance, not all W bosons are boosted sufficiently to produce a single jet. We therefore consider separately the cases of a W boson from a single heavy jet and from a jet pair. Finally, for the $m = 500\,\text{GeV}$ resonance, we only consider the jet pair case. In this section, the cone algorithm will be used and compared with an analysis using the $k_\perp$ jet algorithm.

4.3.1.1 W boson from a single jet

The main backgrounds here will be Z+ 3 jets and $t\bar{t}$. Later in section 4.3.1.3 we consider the impact of Z+4jets in this analysis.

Table 4.VI shows the cut flow for the electron-based and the muon-based analyses for the ChL WZ resonances of mass $m = 1.1$ TeV and $m = 800$ GeV. The $m = 500$ GeV case is not considered here since the W and Z bosons will not be sufficiently boosted, in general, to produce a single jet. The $Z \rightarrow e^+e^-$ and $Z \rightarrow \mu^+\mu^-$ selections are shown, which correspond each to about 50% of the sample events. We make the selection in the following way

- Apply electron quality cuts (*medium* electrons) and muon quality (STACO).
- We select the two highest p_T leptons which should satisfy respectively: $p_T(e,\mu) > 50$ GeV and $p_T(e,\mu) > 35$ GeV.

The low efficiency of the lepton pair cut is approximately consistent with the expected selection efficiency per lepton, as shown in Fig. 4.10, as well as the detector acceptance. As can be seen in Fig. 4.13, the p_T cut suppresses mostly the $t\bar{t}$ background. A leptonic $Z_{e^+e^-}$ or $Z_{\mu^+\mu^-}$ is afterwards reconstructed as described in Section 4.2.2.4, almost eliminating completely this background.

Using the cone algorithm, size 0.8, the hadronic W boson candidate is identified as a heavy single jet having a mass between 70 and 100 GeV, and separated in azimuthal angle from the Z boson candidate by $\Delta\phi(W,Z) > 2$, as described in Section 4.2.1 (see Fig. 4.14). It can be seen that $WZjj$ background (included in α_s^2,α_{ew}^3) is negligible. At this stage, considering that the fraction of single jet W bosons becomes important for $p_T > 250$ GeV (see Fig. 4.2), and in order to be consistent with the preselection cuts on the $Z + 3$ jets background, we apply the following cuts to the reconstructed W and Z bosons: $p_T^{W,Z} > 250$ GeV and $|\eta^{W,Z}| < 2.0$.

After a forward jet selection, (see Section 4.2.3, $p_{T\text{cut}} = 20$ GeV, $E_{\text{cut}} = E_{2\text{cut}} = 300$ GeV, $\eta_{\text{cut}} = 1.5$, $|\eta_{fjet}| > \eta_{\text{central jet}}$, $\Delta\eta_{\text{cut}} = 4.5$), the invariant mass of these two jets is required to be greater than 700 GeV. In Fig. 4.16 we show the distribution of the

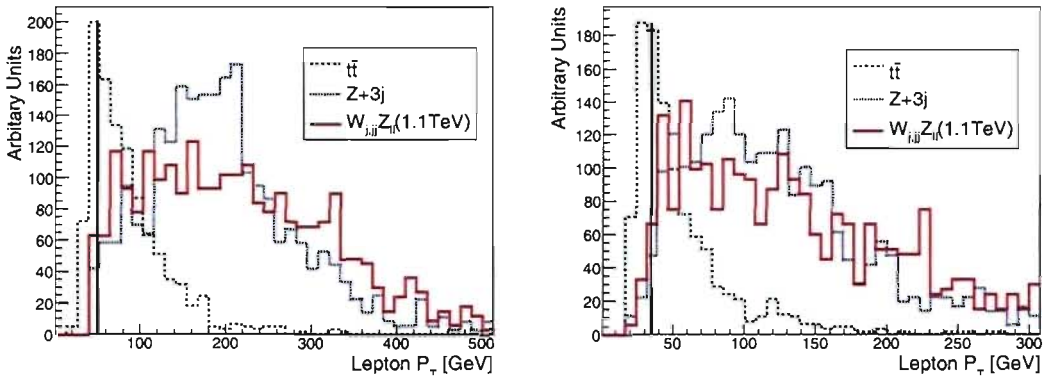

Figure 4.13: p_T of the highest p_T (left) and second highest p_T (right) electrons from reconstructed Z bosons in the $m = 1.1$ TeV resonance sample. Distributions are arbitrarily normalised. The line indicates the cut value.

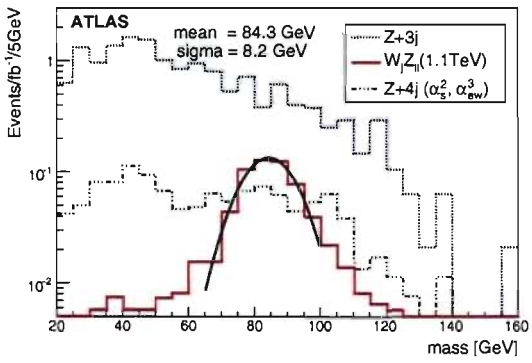

Figure 4.14: Mass of the heavy jet for the $m = 1.1$ TeV ChL resonance and corresponding backgrounds. No $t\bar{t}$ event is left.

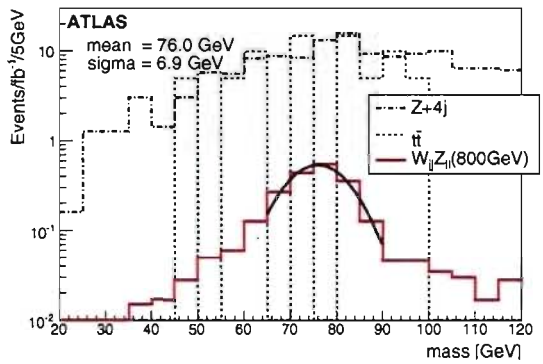

Figure 4.15: Reconstructed W boson mass from a jet pair for the $m = 800$ GeV resonance.

last variable in the case of the 1.1 TeV sample and $Z + 3$ jets background. We set the cut where the plateau starts at 700 GeV. Note that the efficiency of the forward jet cuts appearing in Table 4.VI and in Fig. 4.16 appears artificially good for the background because a preselection was already applied. As mentioned in section 3.2.2, the preselection cuts on jet tagging already suppressed the W+jets background by a factor 3.5

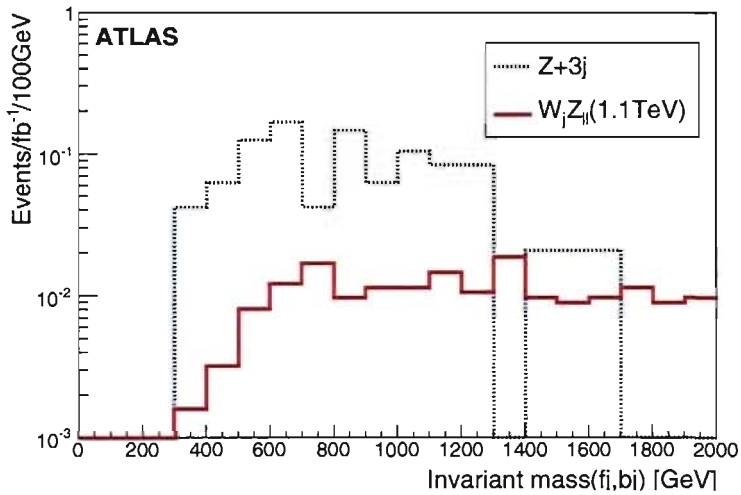

Figure 4.16: Invariant mass of the tagged forward and backward jets.

A central jet veto was found to be unnecessary, as no $t\bar{t}$ event survived the selection. Because of the lack of statistics for the $t\bar{t}$ sample, it is not possible to exclude completely a contribution from this background. The normalisation factor is 4.9, meaning that $t\bar{t}$ is excluded, over the whole mass range, at the level of 11.3 fb at 90% C.L. To have an estimate of the efficiency of the last two cuts at rejecting this background, the mass window for the cut on the Z boson mass was loosened: $60 < m_Z < 120$ GeV, allowing 44 events (215 fb) to pass for the $Z \rightarrow ee$ channel and 38 events (185 fb) for the $Z \rightarrow \mu\mu$ channel. The W boson mass cut alone is found to have an efficiency of 12% and the forward jet cut alone lets no event survive. Assuming that the cuts are independent, the overall efficiency of the heavy jet mass cut and forward jet tagging combined is higher than 0.15%. The exclusion limit at 95% C.L. (1.64 σ) for the $t\bar{t}$ background is shown in Table 4.VI and it will be assumed that this is negligible in the mass window

of the resonance. The Z+4 jets background was not included here because it may be double-counting with Z+3 jets with parton shower. In order to evaluate the level of this background, an average over the high mass region was taken because of the relatively poor Monte Carlo statistics, yielding about 0.03 fb/100 GeV.

For the $m = 1.1$ TeV case, it was found that the trigger efficiency, based on the OR of `e60, mu20` and `j160`, was 100% at the end of the selection.

Figure 4.17 shows the resonance mass resulting when the Z boson has been reconstructed from electrons or muons and the W boson from a single jet of size 0.8.

4.3.1.2 Considering jet inner structure

In the case of very boosted vector bosons in the final state (which is the case particularly for the $m = 1.1$ TeV resonance), as discussed before, the W decay looks like a single wide jet in the calorimeter. In such case, an inner structure was found to be still realizable, as described in section 4.2.1.2 through the observable 'p transverse' (also called $p_{T\text{nj}}$) sketched in Fig 4.7.

Comparing the resonance in Fig. 4.17 (left) to the resonance in Fig. 4.18 where an extra cut of 'p transverse' $>$ 23 GeV was applied (Fig. 4.8 justifies this cut), we see clearly that the discrimination power of this variable has an important impact in the $Z + 3$ jets background. Fig. 4.18 can be compared to the results from the UCL group using the $k_\perp$ algorithm (see section 4.3.1.5). Their analysis for the same resonance is shown in the bottom left plot in Fig. 4.21.

The 'p transverse' has proved to be a powerful tool and certainly a good evidence of inner structure in boosted vector boson hadronic decay.

4.3.1.3 Considering $Z + 4$ jets and $Z + 3$ jets together

When producing the background $Z + 4$ jets and $Z + 3$ jets one has to be aware of the fact that some double counting is present between the two backgrounds. If ever we want to use both backgrounds in the same analysis we need to be aware of this. When performing the fragmentation and hadronization [74], PYTHIA may produce 4 jets in the

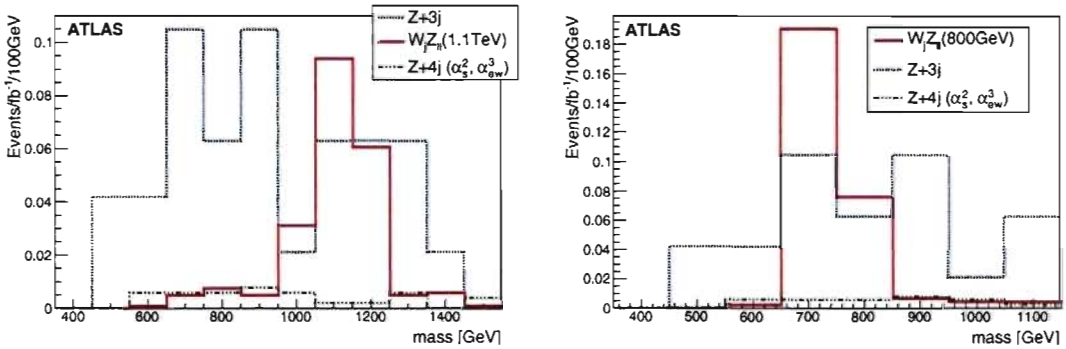

Figure 4.17: Reconstruction of ChL resonance at $m = 1.1$ TeV (left) and $m = 800$ GeV (right) in the channel $qqW_jZ_{\ell\ell}$ (with $\ell = e, \mu$), where a single jet cone 0.8 has been used to reconstruct the W. No $t\bar{t}$ events survive the selection

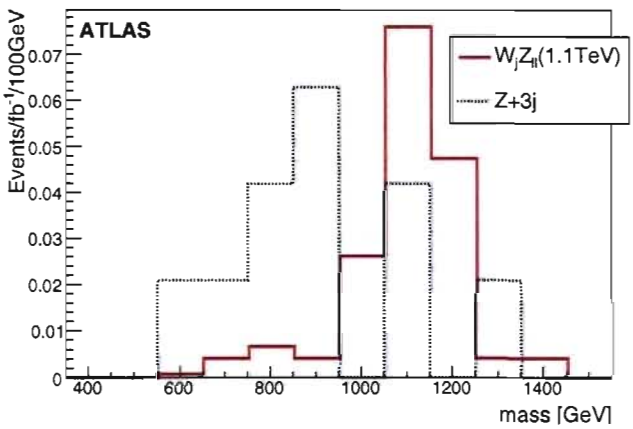

Figure 4.18: Resonance for the $W_jZ_{\ell\ell}$, $m = 1.1$ TeV case, considering 'p transverse' cut as described in section 4.2.1.2.

	$m = 1.1$ TeV		$m = 800$ GeV		$m = 500$ GeV		$Z + 3j$		$Z + 4j$		$t\bar{t}$	
	σ (fb)	eff.	σ (fb)	eff.	σ (fb)	eff.	σ (fb)	eff.	σ (fb)	eff.	σ (fb)	eff.
$Z \to e^+e^-$												
$p_T(e1) > 50$ GeV, $p_T(e2) > 35$ GeV	0.79	22%	2.14	20%	4.15	16%	22.2	20%	195	7.9%	1055	29%
85 GeV $< m_Z <$ 97 GeV	0.63	80%	1.69	79%	3.34	80%	18.5	87%	176	90%	39	3.7%
$Z \to \mu^+\mu^-$												
$p_T(\mu_1) > 50$ GeV, $p_T(\mu_2) > 35$ GeV	0.60	16%	1.67	16%	3.11	12.4%	17.2	16%	170	7.0%	821	22%
83 GeV $< m_Z <$ 99 GeV	0.48	81%	1.40	84%	2.68	86%	15.8	90%	163	95%	64	7.8%
$Z \to e^+e^-$ and $Z \to \mu^+\mu^-$												
W_jZ_u												
Heavy jet mass $W \to j$	0.57	51%	0.75	24%	–	–	2.99	8.7%	–	–	0	0%
Forward jet tagging	0.22	39%	0.29	39%	–	–	0.67	22%	–	–	< 0.25	–
$W_{jj}Z_u$												
65 GeV $< m_{jj} <$ 90 GeV and $\Delta\phi(W_{jj}, Z) > 2.0$	–	–	1.51	25%	2.21	37%	–	–	37.6	11%	9.8	9.5%
Forward jet tagging	–	–	0.62	41%	0.68	31%	–	–	9.57	25%	–	–
Central jet veto	–	–	0.29	47%	0.32	47%	–	–	4.85	51%	–	–

Table 4.VI: Cut flow for the $W_{jj}Z_{\ell\ell}$, $m = 1.1$ TeV, 800 and 500 GeV signals. For each process, the cross-section (fb) surviving the successive application of the cuts is shown, as well as the efficiency of each cut. The upper limit for $t\bar{t}$ in the last lines is for 95% C.L.

final state out of the $Z + 3$jets sample. Those extra jets might be double counted when we introduce the $Z + 4$ jets background. On the other hand, as discussed in chapter 3, the cuts used to produce both backgrounds are quite different, and they cannot really be added, or used in the same analysis (except perhaps in the tightest combinations of cuts). Still, despite the double counting that may appear, we do an analysis using the case $W_j Z_{\ell\ell}$, $m = 800$ GeV, combining both backgrounds, to prove that in the case where we consider reconstruction with W decaying in single jet, the $W + 4$ jets background will be manageable.

The analysis includes the following additional requirements. For every single event, we reconstruct $W \rightarrow j$ also as dijet, exactly as in section 4.3.1.4. If the W is well reconstructed as dijet, we reject the event. In Fig. 4.19 we have both $Z+4$ jets and $Z+3$ and no contribution from $Z + 4$ jets remains. We must remember, however, that we lack sufficient statistics to exclude it completely.

If one wants to be able to mix $Z+4$ and $Z+3$ in the same analysis safely, the double counting ought to be avoided. To do so we can use the procedure called *matching* of parton shower and matrix element, available in the latest version of MADGRAPH. By the time this work was done, such *matching* technique was not available. Matching is also available in ALPGEN (see appendix II) but we could not use ALPGEN samples (already available by the time) because of the lack of statistics. We decided to produce the backgrounds as described in chapter 3. The reader should therefore be aware of the limitations of such approach.

The selection proposed in this section, sets the path towards a dynamical selection between single jet and double jet W reconstruction. When analysing real data, such a selection technique will have to be used. We will need to be able to dynamically select which is the best reconstruction scenario in a given event. This selection was already implemented [10] in the analysis based on the $k_\perp$ algorithm, when reconstructing WZ resonances. Our results, obtained separately for single jet and dijet cases, are compatible with that analysis as shown in section 4.3.1.5.

The same study was done including both $Z + 3$ jets and $Z + 4$ jets with the 1.1 TeV signal. Here one event remains which happens to be close to the resonance region.

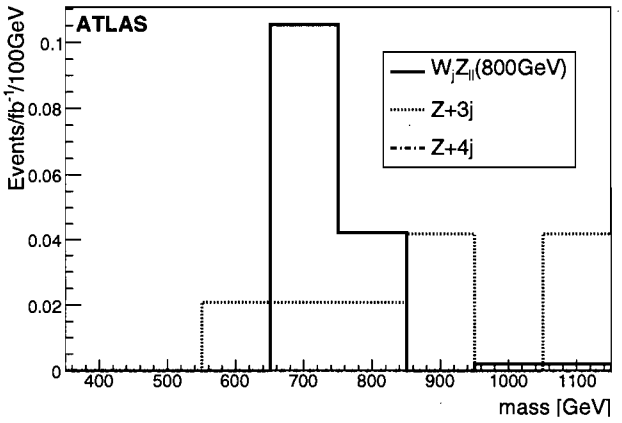

Figure 4.19: Resonance for the $W_j Z_{\ell\ell}$, $m = 800$ GeV case, considering 'p transverse' cut as described in section 4.2.1.2.

4.3.1.4 W boson from a jet pair

As above, after applying electron quality cuts, the lepton transverse momenta are required to satisfy

- $p_T(e_1, \mu_1) > 50$ GeV and $p_T(e_2, \mu_2) > 35$ GeV,
- A Z boson is reconstructed as $Z_{e^+e^-}$ ($Z_{\mu^+\mu^-}$) having a mass between 85 and 97 GeV (83 and 99 GeV).

Considering all pairs of jets with $p_T > 30$ GeV in the central region ($|\eta| < 3.0$) not overlapping with the electron jets from the Z decay, the one yielding an invariant mass closest to the mass of a W boson will be the W boson candidate (see Fig. 4.15). The low efficiency of this cut can be explained in part by the fact that a good fraction of events are constituted of a single jet W boson. Forward and backward jet selection proceeds as in 4.3.1.1. A central jet veto is also applied: we exclude events with an extra jet, having a $p_T > 30$ GeV, not corresponding to the jets from the W boson or the forward and backward jets and we require the W and Z directions to be in the central region $|\eta| < 2$. Figure 4.20 shows the resulting reconstructed resonance masses. Table 4.VI summarizes the cut flow for this analysis. Here, by using the technique of widening the

Z boson mass window as in Sect. 4.3.1.1, it is estimated that the $t\bar{t}$ background could be approximately 0.13 fb and it will be assumed that this is negligible in the mass window of the resonance.

4.3.1.5 Dynamic selection (comparative analysis)

The UCL group presented in [10] a study of signals $qqW_{jj}Z_{\ell\ell}$ for $m = 500\,\text{GeV}$, $m = 800\,\text{GeV}$ and $m = 1.1\,\text{TeV}$, using the $k_\perp$ algorithm for jet reconstruction. They did not separate the study of the hadronic W decay into single jet case (see section 4.3.1.1) and jet pair case (see section 4.3.1.4), as we did in this work.

In Fig. 4.21 we see the final result of this analysis for the three resonance masses. The top left plot shows the 500 GeV case where a quite low signal is present. It results from the fact that the preselection cuts applied to the $Z + 3$ jets background needed to be applied here as well. Let us consider now the top right plot in Fig. 4.21 where we get a significance of 7.4 ± 1.1. In our study we looked separately at the single jet case and jet pair case which can be seen on Fig. 4.17(right) and Fig. 4.20(left). The significances are 4.9 ± 1.1 and 3.9 ± 1.5 (see table 4.IX) respectively. To compare we need to combine the two results first. If we add both analysis and calculate the significance we get a value of 6.2 ± 1.9, which is in reasonable agreement with the $k_\perp$-based analysis.

Finally the bottom left plot in Fig. 4.21 gives a significance of 4.5 ± 1.2, and it can be compared to Fig. 4.17(left) where we get a significance of 3.6 ± 1.0 (see table 4.IX). Again, in this analysis we are not considering at all the jet pair case for W reconstruction, and the significance value should be higher.

This rough, but still conservative comparison of the dynamical and non dynamical W decay selection, lets us conclude that both analyses are consistent. It is not possible to conclude at this point if $k_\perp$ could give a better overall result than the cone analysis or vice versa. We can only say that both deliver roughly the same results. On section 4.3.1.3, we showed a simple approach to dynamical selection (with cone algorithm) with the purpose of showing that combining both $Z + 3$ jets and $Z + 4$ jets would not be an issue. We learned that mixing both, single jet case and jet pair analysis helps obtaining a better significance.

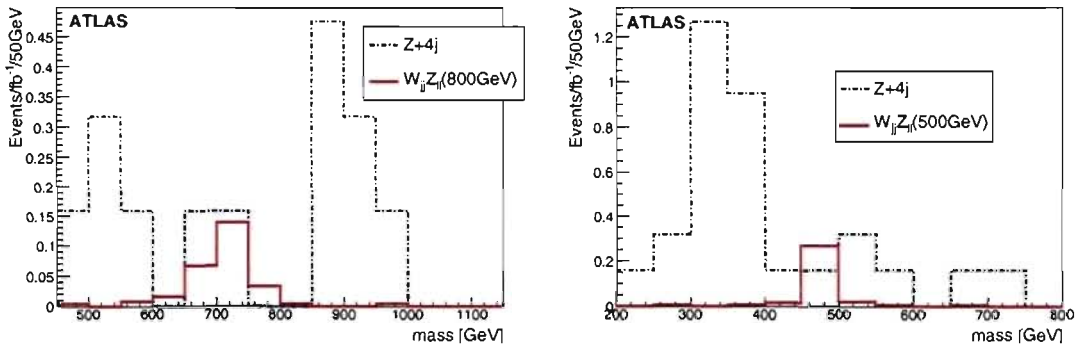

Figure 4.20: Reconstructed ChL resonance at $m = 800\,\text{GeV}$ (left) and $m = 500\,\text{GeV}$ (right) in the channel $qqW_{jj}Z_{\ell\ell}$ (with $\ell = e, \mu$) where two jets of cone size 0.4 have been used to reconstruct the W boson. No $t\bar{t}$ events survive the selection.

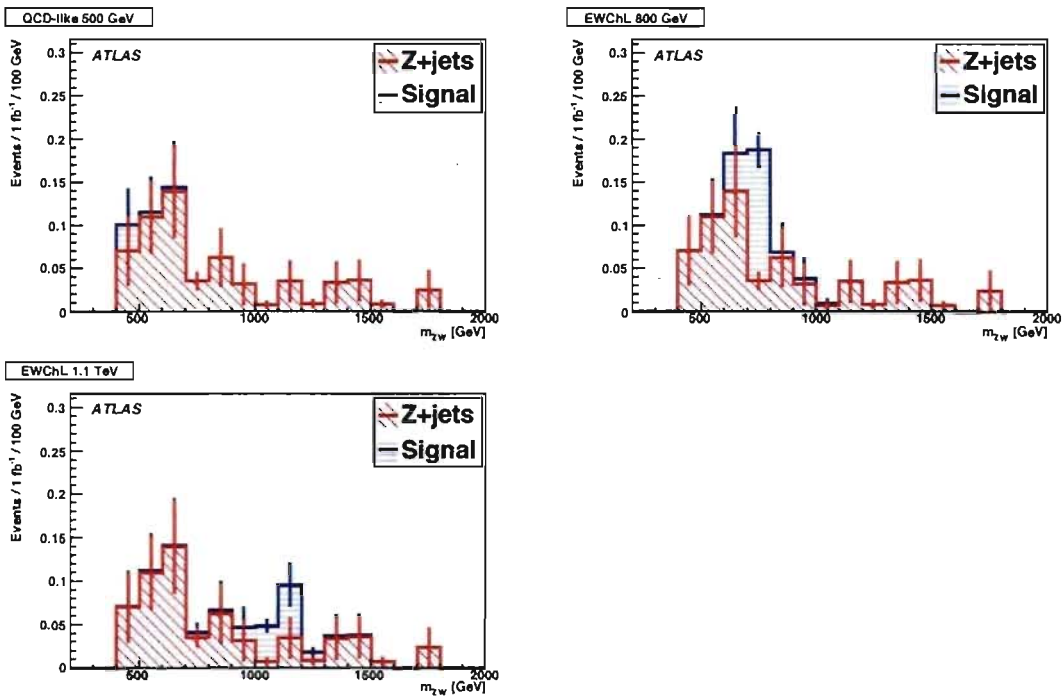

Figure 4.21: Reconstructed ChL resonance at $m = 500\,\text{GeV}$ (top left), $m = 800\,\text{GeV}$ (top right) and $m = 1.1\,\text{TeV}$ (bottom left) in the channel $qqW_{jj}Z_{\ell\ell}$ (with $\ell = e, \mu$) where the $k_\perp$ algorithm has been used to reconstruct jets. In this study a dynamic selection between $W \to j$ and $W \to jj$ has been performed. This results have been delivered by the UCL group and can be found in [10]. $t\bar{t}$ background was found to be negligible.

4.3.2 $W^{\pm}Z \rightarrow \ell^{\pm}\nu\ \ell^{+}\ell^{-}$

This purely leptonic channel consists of four different signatures: $W_{\ell^{\pm}\nu}Z_{\ell^{\pm}\ell^{\mp}}$ with $\ell = e, \mu$. The main background will be $WZjj$ production from the Standard Model. The $ZZ \rightarrow 4l$ background can also mimic the signal when one of the leptons, for example, goes undetected in the forward region, but the cross section and Br are very small compared with the WZ signal and can be considered negligible here. The analysis starts by identifying leptonic $Z_{e^+e^-}$ ($Z_{\mu^+\mu^-}$) bosons as described in Section 4.2.2.4, after requiring two leptons with p_T greater than 50 and 35 GeV.

As a second step, we proceed to reconstruct the W boson from the highest p_T lepton among those remaining in the event, if there is one, and the measured missing transverse energy (which we required to be > 60 GeV), as described in Section 4.2.2.5. The solution which yields the highest p_T W boson is kept.

The forward and backward jet selection follows the prescription of the Section 4.2.3 ($p_{T\text{cut}} = 20$ GeV, $E_{\text{cut}} = E_{2\text{cut}} = 300$ GeV, $\eta_{\text{cut}} = 1.5$, $|\eta_{fjet}| > \eta_{\text{central jet}}$), $\Delta\eta_{\text{cut}} = 4.5$).

In Table 4.VII we present the cut flow of the reconstruction of the resonances for 1.1 TeV and 500 GeV. Also in Fig. 4.22 and Fig. 4.23 we present the reconstructed resonance and the background $WZjj$ for the same resonance mass.

4.3.3 $ZZ \rightarrow \nu\nu\ \ell^{+}\ell^{-}$

This scalar resonance can be interpreted as a Standard Model Higgs boson produced by vector boson fusion. At leading order, the cross-section times branching ratio would

	$W_{\ell\nu}Z_{\ell\ell}$ ($m =$ **500 GeV**)		$W_{\ell\nu}Z_{\ell\ell}$ ($m =$ **1.1 TeV**)		$W_{\ell\nu}Z_{\ell\ell jj}(SM)$	
	σ (fb)	eff.	σ (fb)	eff.	σ (fb)	eff.
Z_{ee}	1.47	18%	0.23	20%	20.7	16%
$Z_{\mu\mu}$	1.09	14%	0.18	15%	16.7	13%
W reconstruction	1.43	56%	0.25	61%	18.9	51%
Forward jet tagging	0.63	44%	0.14	56%	1.6	8.5%

Table 4.VII: Cut flow for the $W_{\ell\nu}Z_{\ell\ell}$ ($m = 500$ GeV and 1.1 TeV) signals. All the cuts are described in detail in this section.

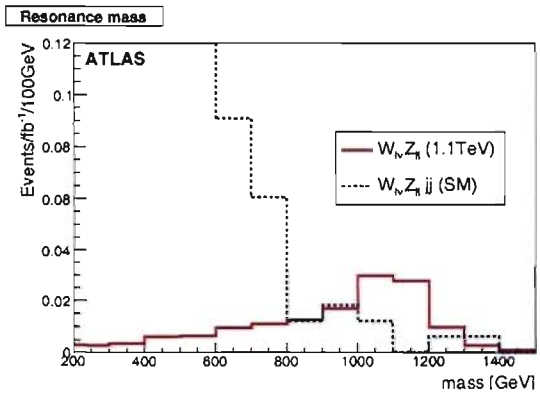

Figure 4.22: Full reconstruction of ChL resonance $m \sim 1.1$ TeV ($W_{\ell^{\pm}\nu}Z_{\ell^{\pm}\ell^{\mp}}$).

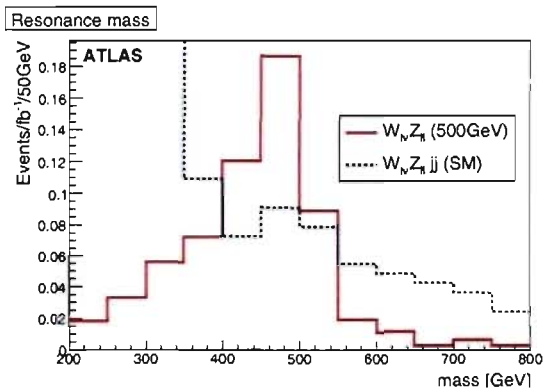

Figure 4.23: Full reconstruction of QCD-like resonance $m \sim 500$ GeV ($W_{\ell^{\pm}\nu}Z_{\ell^{\pm}\ell^{\mp}}$).

be 6 fb, compared to 4 fb obtained for the ChL model. This signal is characterised by a leptonic Z boson accompanied by large $\not{E}_T$, yielding a large transverse mass.

The backgrounds considered are: $ZZjj \rightarrow \ell\ell\nu\nu jj$ and $WZjj \rightarrow \ell\nu\ell\ell jj$. Other background can result from Z+jets production, where the tail of the missing transverse energy distribution can fake a signal.

After selecting the leptonically decaying $Z_{e^+e^-}$ ($Z_{\mu^+\mu^-}$) boson as usual, with mass between 85 and 97 GeV (83 and 99 GeV), a minimum $\not{E}_T$ of 150 GeV is required. For this high value of $\not{E}_T$, Z+jets background is expected to be negligible for a Standard Model Higgs boson signal [46]. The forward jet selection is applied (see Section 4.2.3, $p_{T\text{cut}} = 20$ GeV, $E_{\text{cut}} = E_{2\text{cut}} = 300$ GeV, $\eta_{\text{cut}} = 1.5$, $\Delta\eta_{\text{cut}} = 4.5$).

The transverse mass, defined as:

$$m_T^2 = (\sqrt{p_T(Z)^2 + m_Z^2} + \not{E}_T)^2 - (\vec{p}_T(Z) + \vec{\not{p}}_T)^2 \tag{4.1}$$

is shown in Fig. 4.24 and the cut flow can be found in Table 4.VIII.

4.4 On the QCD and QED background

As shown in table 3.I and presented in section 3.2.2 the background Z+jets was divided in several parts for MC production purposes. In Fig. 4.25 we present the analysis

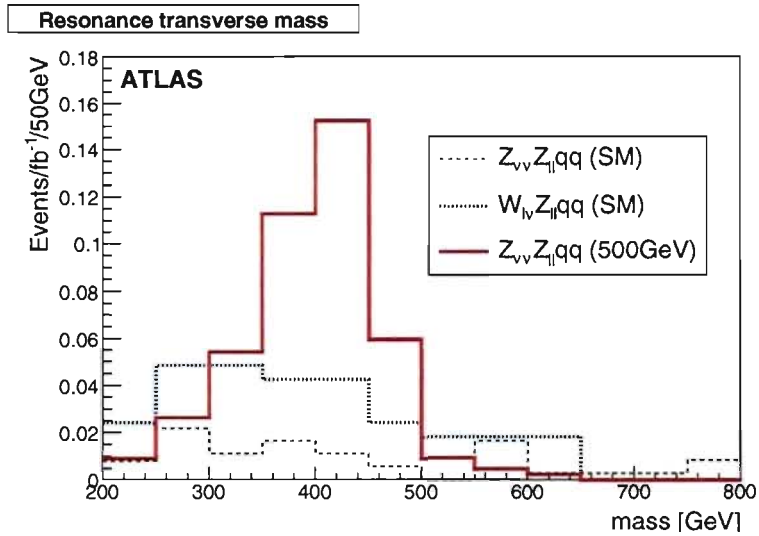

Figure 4.24: Transverse mass of the $m = 500$ GeV resonance $Z_{\nu\nu}Z_{\ell\ell}$.

	$Z_{\nu\nu}Z_{\ell\ell}qq$ ($m =$ **500GeV**)		$W_{\ell\nu}Z_{\ell\ell}jj$ **(SM)**		$Z_{\nu\nu}Z_{\ell\ell}jj$ **(SM)**	
	σ (fb)	eff.	σ (fb)	eff.	σ (fb)	eff.
Z_{ee}	0.72	17.6%	20.78	22%	9.1	20%
$Z_{\mu\mu}$	0.58	15%	16.7	17%	6.6	15%
Forward jet tagging	0.58	45%	3.2	8.6%	0.47	3%
$\not{E}_T > 150$ GeV	0.44	75%	0.46	14%	0.12	26%

Table 4.VIII: Cut flow for the $Z_{\nu\nu}Z_{\ell\ell}qq$ ($m = 500$ GeV) signal. All the cuts are described in detail in this section.

of the signal $W_jZ_{\ell\ell}$, $m = 1.1$ TeV, with the $Z + 3$ jets background explicitly divided into its $(\alpha_s^3, \alpha_{ew}^1)$ and $(\alpha_s^1, \alpha_{ew}^3)$ components. We see that $(\alpha_s^1, \alpha_{ew}^3)$ is completely negligible. It is the case also for $Z + 4$ jets where the $(\alpha_s^2, \alpha_{ew}^3)$ and (α_{ew}^5) have a negligible contribution to the total background after the analysis.

4.5 Trigger efficiency after event selection

As was mentioned in section 4.1, the trigger efficiency is almost 100% in all the analyses presented in section 4.3. This is the expected response from the trigger system since these signals are cased by very high energetic objects in the detector subsystems, and/or a noticeable $\not{E}_T$ value. It is also due to the fact that the HLT uses essentially the same reconstruction algorithms for leptons and jets. We stress this point since it is considered to be of crucial relevance if one wants to study these signals with real data in the near future. We want to make sure the trigger system responds properly to VBS at high energy.

4.6 Results

The significance of the signals and the luminosity required for a possible discovery are estimated here. From the reconstructed resonance mass distributions in Section 4.3 one can evaluate the size of the signal and background in the resonance mass window. In order to calculate the asociated errors, the statistical uncertainty is considered and calculated from the number of events within the window selected around the resonance. The errors presented come in the form $N_{events} \pm$ MCError $\pm$ StatError. Where MCError stands for the error implicit in the amount of MC events obtained, and the StatError is the actual statistical error in the events present in the peak region.

Table 4.IX summarises the approximate cross-sections expected after the analyses described above. The table also gives the luminosity required to observe a significant excess over the background, showing the uncertainty, and the significance of a signal for an integrated luminosity of 100 fb^{-1}. Because of the large statistical and systematic uncertainties (see Section 4.7), the numbers given here must be taken as an approximate

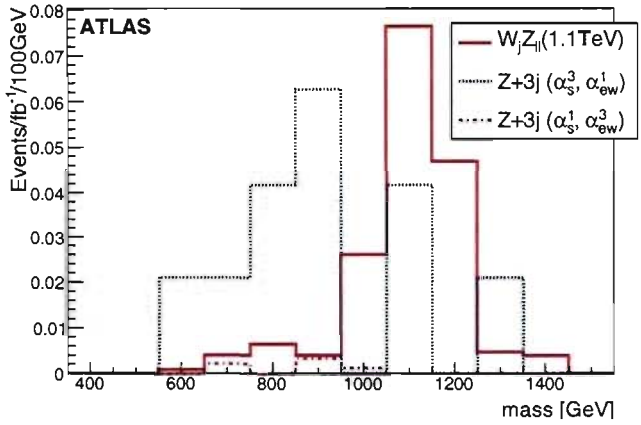

Figure 4.25: Resonance for the $W_j Z_{\ell\ell}$, $m = 1.1$ TeV case, with $Z + 3$ jets background divided into $(\alpha_s^3, \alpha_{ew}^1)$ and $(\alpha_s^1, \alpha_{ew}^3)$ (see table 3.I).

indication of the reach of the LHC for such resonances.

The significance is calculated as [75]

$$\text{significance} = \sqrt{2((S+B)\ln(1+S/B) - S)} \quad , \tag{4.2}$$

where S (B) is the number of expected signal (background) events in the signal *peak* region, which is defined as the three consecutive bins (of size given in the figures, chosen to represent the resolution), with the highest total number of signal events. The background is averaged over this region.

For each of the WZ resonances, results of the different channels, $W_{\ell\nu} Z_{\ell\ell}$, $W_{jj} Z_{\ell\ell}$ and $W_{\ell\nu} Z_{jj}$ can, in principle, be combined. From Table 4.IX, one can conclude that for two of three mass regions, $m = 500$ GeV and 800 GeV, a chiral Lagrangian vector resonance can be discovered with less than 100 fb^{-1}. The expectations with the alternative $k_\perp$ analysis described in Section 4.3.1.5 are not far from the values in Table 4.IX. As an example, the integrated luminosity needed for 3σ observation of the $m = 800$ GeV signal is 63 fb^{-1}, and of the $m = 1.1$ TeV signal is 81 fb^{-1}.

A scalar resonance at $m = 500$ GeV will require about 60 fb^{-1} to be seen in the

Process	Cross-section (fb)		Luminosity (fb^{-1})		Significance for 100 fb^{-1}
	signal	background	for 3σ	for 5σ	
$W_{jj}Z_{\ell\ell}$, 500 GeV	$0.28 \pm 0.04 \pm 0.05$	$0.20 \pm 0.18 \pm 0.04$	30	90	5.3 ± 2.1
$W_{\ell\nu}Z_{\ell\ell}$, $m = 500$ GeV	$0.40 \pm 0.03 \pm 0.06$	$0.25 \pm 0.03 \pm 0.05$	20	60	6.6 ± 1.1
$W_{jj}Z_{\ell\ell}$, 800 GeV	$0.24 \pm 0.02 \pm 0.05$	$0.30 \pm 0.22 \pm 0.05$	60	160	3.9 ± 1.5
$W_jZ_{\ell\ell}$, $m = 800$ GeV	$0.27 \pm 0.02 \pm 0.05$	$0.23 \pm 0.07 \pm 0.05$	40	110	4.9 ± 1.1
$W_jZ_{\ell\ell}$, $m = 1.1$ TeV	$0.19 \pm 0.01 \pm 0.04$	$0.22 \pm 0.07 \pm 0.05$	70	190	3.6 ± 1.0
$W_{\ell\nu}Z_{\ell\ell}$, $m = 1.1$ TeV	$0.070 \pm 0.004 \pm 0.026$	$0.020 \pm 0.009 \pm 0.014$	70	190	3.6 ± 1.4
$Z_{\nu\nu}Z_{\ell\ell}$, $m = 500$ GeV	$0.32 \pm 0.02 \pm 0.06$	$0.15 \pm 0.03 \pm 0.04$	20	60	6.6 ± 1.3

Table 4.IX: Approximate signal and background cross-sections expected after the analyses. An approximate value of the luminosity required for 3σ and 5σ significance, and the expected significance for 100 fb^{-1} are shown. The uncertainties, are due to Monte Carlo statistics and the statistical error of the counting of events in the peak region for each process.

$ZZ \rightarrow \nu\nu\ell\ell$ channel.

We also show, for completion, $WW/WZ \rightarrow l\nu jj$ analysis results performed mostly by the UCL group, in Table 4.X.

4.7 Systematic Uncertainties

A number of large systematic uncertainties affect the signals studied here. Because of the small cross-sections and the important backgrounds, it is difficult to estimate them with precision from Monte Carlo simulations. Data-driven tests will be required to understand better the systematic effects. Some discussion of the most significant effects is given here.

4.7.1 Background Cross-sections

The renormalization and factorization scale, Q^2, which should be approximately related to the transverse momentum of the propagator of the vector bosons, are selected differently in various MC generators. In our case we use two different choices of Q-scale. For MADGRAPH $Q^2 = M^2_{\mathrm{VB}}$ and in ALPGEN $Q^2 = M^2_{\mathrm{VB}} + \sum p^2_T(j)$. This selection can affect the cross-section by as much as a factor of two. This is especially true at high centre of mass energies, where the degree of virtuality of partons and choice of scale for α_s are quite critical [11, 12]. At present this represents a theoretical uncertainty on the current sensitivity estimate. While the predictions may improve in future, in an eventual analysis, the backgrounds would have to be measured from data and the eventual size of the associated systematic uncertainty has not been studied here.

Another consideration is that for the analyses which dynamically move between the dijet and single jet reconstruction technique for the hadronically decaying vector boson (see Section 4.2.1), to evaluate the background with the samples available both W+3 jet and W+4 jet samples must be used. This implies some double-counting due to the lack of parton-shower matching in these samples, so the background will be overestimated. This is in addition to the fact that as shown in Section 3.3.1, the MADGRAPH samples used overestimate slightly the energy of the tag jets. The effect is expected to be at the

Process	Cross section (fb)		Luminosity (fb^{-1})		Significance for 100 fb^{-1}
	signal	background	for 3σ	for 5σ	
$WW/WZ \to \ell\nu\, jj$, $m = 500$ GeV	0.31 ± 0.05	0.79 ± 0.26	85	235	3.3 ± 0.7
$WW/WZ \to \ell\nu\, jj$, $m = 800$ GeV	0.65 ± 0.04	0.87 ± 0.28	20	60	6.3 ± 0.9
$WW/WZ \to \ell\nu\, jj$, $m = 1.1$ TeV	0.24 ± 0.03	0.46 ± 0.25	85	230	3.3 ± 0.8

Table 4.X: Approximate signal and background cross sections expected after the $WW/WZ \to l\nu jj$ analyses performed mostly by the UCL group [10]. An approximate value of the luminosity required for 3σ and 5σ significance, and the expected significance for 100 fb^{-1} are shown. The uncertainties are due to Monte Carlo statistics only.

few per cent level.

4.7.2 Monte Carlo Statistics

We are limited by the very large size of the background samples required. Fast MC simulation was shown to be in good agreement with full simulation and was used to evaluate $t\bar{t}$ background for the WW signals (this analysis was performed by the UCL group [10] and is not shown in this work). In some cases, only upper limits on the backgrounds can be given, although it is expected that these limits will be very conservative. Again, this represents a systematic uncertainty on the current sensitivity estimates, but will not be present in a final data analysis, assuming sufficient simulated data were eventually available.

4.7.3 Pile-up and Underlying Event

The cross-section for inelastic, non-diffractive pp interactions at the LHC is expected to be around 67 mb. At design luminosity ($10^{34}cm^{-2}s^{-1}$), the average number of minimum-bias events is around 23 per bunch crossing. Any collision recorded in the ATLAS detector therefore contains a superposition of particles coming from several events. In general the particles from a single *interesting physics* event will have triggered the readout, and additional particles will come from other uninteresting pp collisions. The

hits from these other uninteresting interactions are not related to the physics event, represent a serious background and are known as pile-up. The number of interactions that will occur when the beams cross, follows a Poisson distribution with an expected mean value of 23 interactions at design luminosity. Many previous bunch crossings, as much as 20 for the calorimeter, can contribute to the signal observed at any given bunch crossing because of the long underfoot of the electronic signal shape. The Poisson distribution has a long tail above the most probable value, so a substantial fraction of the bunch crossings will have more than the average number of interactions. Pile-up is not well understood yet for the ATLAS detector. Studies of this effect are ongoing.

Fully simulated samples with pile-up at low luminosity ($10^{33}\text{cm}^{-2}\text{s}^{-1}$) were available, but with much lower statistics: we restricted the analysis to one signal and one background samples. However pile-up effects should be approximately independent of the underlying physics sample, and we assume we can safely generalise the results obtained here.

We compared the same events of the $W_{jj}Z_{\ell\ell}$ at $m = 1.1\,\text{TeV}$ sample reconstructed with and without pile-up simulation. This allows computation of the fraction of events with pile-up having tagged forward jets with respect to corresponding non-pile-up events which fail the tagged jet criterion, thus defining a 'fake' rate. The reciprocal fraction defines a 'miss' rate. The effect of pile-up increases with increasing jet radius and decreasing energy threshold, as would be expected. We found that both 'fake' and 'miss' effects are essentially due to the degradation of energy resolution in presence of pile-up and that their combination contributes to an uncertainty on the efficiency of the order of 5%.

Pile-up and underlying event are related effects which have potentially similar and crucial impact on the efficiency of the forward jet cuts, the central jet veto and the jet mass resolution. Of particular concern is the fact that the initial minimum p_T cut in the WZ analysis uses jets down to $p_T = 20\,\text{GeV}$, expected to be strongly affected by these effects [76]. Raising the cut to any higher values admits significantly larger background. Some of this can be removed for the higher mass resonances by raising the p_T cut on the vector boson. However, a more promising approach is likely to be to exploit b-tagging

and improved jet mass reconstruction.

Current simulations use underlying event models tuned to Tevatron and other data [77], but there is a large extrapolation needed to 14 TeV. The underlying event would have to be measured in LHC data, and its level is not currently known.

4.7.4 Other Systematic Effects

Systematic effects, such as uncertainties in the luminosity, in efficiencies and resolutions, jet energy scale, fake rates, etc. are of the order of a few percent (except in the case of uncertainties related to jet identification where systematics could be a bit higher, but no more than 5%) and will therefore be completely dominated by the above effects and by statistical uncertainties.

We are mostly concerned here with other systematics effects related to jet objects. Contrary to the "singular" reconstruction objects like particles (electrons, photons, taus, muons) we do not have a good way of determining systematic errors prior to having collision data of sufficient quality, simply due to the composite character of the jets and the corresponding lack of testbeam reference data for this particular object. Another limiting factor is the limited quality of the hadronic shower simulation, and the rather unknown uncertainties of the jet energy scale (JES) and resolution introduced by the underlying event - which most certainly will dependent on the physics channel we are looking at, and, very probably also, on the chosen jet algorithm and its configuration.

We think one should be conservative for the moment. As for the initial systematic error on the jet energy scale, it has been unofficially reported, as a very preliminary result still, that including all uncertainties from test beam simulations we cannot expect more than 5% at best for a given jet. Jets near cracks (big spaces between detector components like the space between barrel and end caps in the hadronic calorimeter) may suffer more, having $\sim$ 10 % uncertainties, as estimated from QCD di-jets samples.

CONCLUSION

Being one of the most successful theories in physics, the SM of electroweak interactions has also many weaknesses and some of its predictions do not meet present experimental data. In particular the nature of the Symmetry Breaking Sector is still unknown and the Higgs boson undiscovered. Since the Goldstone bosons resulting from the symmetry breaking become the longitudinal components of the gauge bosons, the study of longitudinal vector boson scattering in the TeV region could reveal valuable information, hopefully in the form of resonances which should then be discovered at the LHC.

The ChL model, is an effective theory of VB scattering yielding a good description at low energies. A proper implementation of a regularization method inspired by low energy $\pi - \pi$ scattering, allows us to study VB scattering resonances in a higher energy range where new information on the unknown SBS may appear. The Chiral Lagrangian model with Padé unitarisation provides a framework for studying vector boson scattering at high mass, in case a light Higgs boson is not found at the LHC in the first years of running.

ATLAS is a general-purpose detector that will allow us to test many new-physics scenarios. The high energy range available at the LHC and the detection capabilities of ATLAS will allow us to gather information that will surely give answers (or raise more questions) on physics beyond our knowledge. The reconstruction of high-mass WZ resonances arising from a ChL model have been studied using ATLAS full detector simulation and some of the possible channels have been shown to be potentially observable in future collisions at LHC and detectable over the background signals in the ATLAS experiment. Some reconstruction techniques used for event selection and signal reconstruction had to be developed and implemented to perform this analysis, such as: jet definition and reconstruction, forward jets, general particle tagging and overlapping.

To suppress the very high backgrounds from W+jets and Z+jets to acceptable levels requires special techniques investigated here. In particular, at these high masses, hadronic vector boson decay results oftens in a single jet. The $k_\perp$ and the cone al-

gorithms can be applied to resolve a heavy jet into two light jets, suppressing further the background. Other conventional techniques for the study of vector boson fusion are also found essential for the present analysis, like forward jet tagging, and kinematic cuts-based analysis. With full detector simulation, the search for vector and scalar resonances of masses $m = 500$, 800 and 1100 GeV was studied.

The discovery of resonances in vector boson scattering at high mass will take a few tens of fb^{-1}, but the different decay channels of the vector boson pairs allow a cross-check of the presence of a resonance. These results can be considered generic of vector boson scattering and can therefore be interpreted in terms of other theoretical models with possibly different cross-sections. A summary of the discovery potential for the different channels can be found in Table 4.IX.

The analysis presented here is performed with realistic simulation and reconstruction of leptons and jets. Improvements can be expected such as for lepton reconstruction efficiency and for dijet mass resolution by more sophisticated analysis. With real data and a good understanding of the detector, further gains can be achieved by improvements in the reconstruction techniques. This work has resulted in the following publications: [61], [10] and [17] and [78].

We look forward to real data with ATLAS, when we could make these definitive tests of EWSB.

The low threshold of the ATLAS-MPX detectors installed in the ATLAS cavern and detector was successfully calibrated for a given energy range. Also a software infrastructure for ATLAS-MPX data was developed and used for further characterisation studies of the detector for its use in the project. The MediPix analysis framework and data model is being used by a number of people in the collaboration and is a fundamental part of the on-line infrastructure of the ATLAS-MPX project. This work has resulted in the following publications: [79], [80], [81] and [82].

BIBLIOGRAPHY

[1] A. Djouadi, "The Anatomy of Electro-Weak Symmetry Breaking. Tome I: The Higgs boson in the Standard Model," *Phys.Rept.* **457** (2008) 1–216, hep-ph/0503172v2.

[2] LEP Electroweak Working Group, "Precision Electroweak Measurements on the Z Resonance," 2005.

[3] A. Gomez Nicola and J. R. Pelaez, "Meson meson scattering within one loop chiral perturbation theory and its unitarization," *Phys. Rev.* **D65** (2002) 054009, hep-ph/0109056.

[4] A. Dobado, M. J. Herrero, J. R. Pelaez, and E. Ruiz Morales, "LHC sensitivity to the resonance spectrum of a minimal strongly interacting electroweak symmetry breaking sector," *Phys. Rev.* **D62** (2000) 055011, hep-ph/9912224.

[5] A. S. Belyaev *et. al.*, "Strongly Interacting Vector Bosons at the LHC: Quartic Anomalous Couplings," *Phys.Rev.D* **59** (1999) 015022, hep-ph/9805229.

[6] J. Bagger *et. al.*, "CERN LHC analysis of the strongly interacting W W system: Gold plated modes," *Phys. Rev.* **D52** (1995) 3878–3889, hep-ph/9504426.

[7] L. V. M. Fabbrichesi, "Possible experimental signatures at the lhc of strongly interacting electro-weak symmetry breaking," *Phys. Rev. D* **76** (2007), no. 056002 hep-ph/0703236v2.

[8] A.Miagkov, "Vector boson scattering in chiral lagrangian model," ATL-PHYS-99-006.

[9] C. Santamarina, P. Conde Muíño and B. Vachon, "Overview and Performance Studies of Jet Identification in the ATLAS Triger System," *CERN-PH* (2008).

[10] G. Azuelos, P.-A. Delsart, J. Idárraga *et.al.*, "Vector bosons scattering at high mass." CSC note in preparation, 2008.

[11] Eboli, O. J. P. and Gonzalez-Garcia, M. C. and Mizukoshi, J. K., "p p —> j j e+- mu+- nu nu and j j e+- mu-+ nu nu at O(alpha(em)**6) and O(alpha(em)**4 alpha(s)**2) for the study of the quartic electroweak gauge boson vertex at LHC," *Phys. Rev.* **D74** (2006) 073005, hep-ph/0606118.

[12] Barger, Vernon D. and Han, Tao and Ohnemus, J. and Zeppenfeld, D., "Perturbative QCD calculations of Weak Boson production in association with jets at Hadron Colliders," *Phys. Rev.* **D40** (1989) 2888. Erratum-ibid.D41:1715,1990.

[13] J. M. Butterworth, J. R. Ellis, and A. R. Raklev, "Reconstructing sparticle mass spectra using hadronic decays," *JHEP* **05** (2007) 033, hep-ph/0702150.

[14] S. Allwood-Spiers, "Electroweak symmetry breaking without a higgs boson at the lhc," arXiv:0705.2869v1[hep-ex].

[15] S. Allwood, "Manchester Ph.D. Thesis," 2006.

[16] A. Miagkov, "Vector boson scattering in chiral lagrangian model," ATL-PHYS-006.

[17] G. Azuelos, P.-A. Delsart, J. Idarraga *et.al.*, "Les Houches. "Physics at TeV colliders 2005", Beyond the Standard Model Working Group: Summary report," hep-ph/0602198v1.

[18] S. Dawson, "Introduction to electroweak symmetry breaking," hep-ph/9901280.

[19] Particle Data Group, "Nuclear and particle physics," *Journal of Physics G* **33** (2006) http://www.iop.org/journals/jphysg.

[20] J. Dress *et. al.*, 2001. The LEP Collaborations and the LEP Electroweak Working Group, as reported by J. Dress at the XX International Symposium on Lepton and Photon Interactions at High Energy, Rome, Italy.

[21] U. Dore and D. Orestano, "Experimental results on neutrino oscillations," *Rep. Prog. Phys.* **71** (2008), no. 106201 arXiv:0811.1194 [hep-ex].

[22] UA1 Collaboration (G. Arnison *et.al.*), "Recent Results on Intermediate Vector Boson Properties at the CERN Super Proton Synchrotron Collider," *Phys.Lett.B* **166** (1986), no. 484 CERN-EP-85-185.

[23] UA2 Collaboration (R. Ansari *et.al.*), "Measurement of the Standard Model Parameters from a Study of W and Z Bosons," *Phys.Lett.B* **186** (1987), no. 440 CERN-EP-87-05.

[24] Tevatron Electroweak Working Group, for the CDF Collaboration, the D0 Collaboration, "A combination of cdf and d0 results on the mass of the top quark," 2007.

[25] H. E. Haber and G. L. Kane, "The search for supersymmetry : probing physics beyond the standard model," *Phys. Rep.* **117** (1985) 75–263.

[26] C. T. Hill and E. H. Simmons, "Strong dynamics and electroweak symmetry breaking," *Phys.Rept. 381 235-402* **381** (2003) 235–40, hep-ph/0203079v3.

[27] D. D. Dietrich, "Electroweak symmetry breaking in other terms," arXiv:hep-th/0804.0904v1.

[28] J. H. Csaba Csáki and P. Meade, "Tasi lectures on electroweak symmetry breaking from extra dimensions," arXiv:hep-ph/0510275v1.

[29] G. Ecker, "Low-Energy QCD," *Prog. Part. Nucl. Phys.* **36** (1996) 71–83.

[30] T. Appelquist and G.-H. Wu, "The Electroweak Chiral Lagrangian and new precision measurements," *Phys.Rev.D* **48** (1993) 3235–3241, hep-ph/9304240.

[31] W. Kilian, "Electroweak symmetry breaking: The bottom-up approach," *Springer Tracts Mod. Phys.* **198** (2003) 1–113.

[32] Michael E. Peskin and Daniel V. Schroeder, *An Introduction to Quantum Field Theory*. ABP, 1995.

[33] R. M. Rodolfo A. Diaz, "The custodial symmetry," *Rev.Mex.Fis.* **47** (2001) 489–492, hep-ph/0302058.

[34] A. Dobado and J. R. Pelaez, "The inverse amplitude method in chiral perturbation theory," *Phys. Rev.* **D56** (1997) 3057–3073, hep-ph/9604416.

[35] J. D. Jackson, *Classical Electrodynamics*. Wiley, third ed., 1998.

[36] W. K. A. Alboteanu and J. Reuter, "Resonances and unitarity in weak boson scattering at the LHC," *JHEP* **0811** (2008), no. 010 arXiv:0806.4145 [hep-ph].

[37] J. Gasser and H. Leutwyler, "Chiral perturbation theory to one loop.," *Annals Phys.* **158** (1984), no. 142.

[38] A.Dobado and M. Herrero, "Phenomenological lagrangian approach to the symmetry breaking sector of the standard model," *Phys.Lett.B* **228** (1989), no. 495.

[39] M. S. Chanowitz and M. K. Gaillard, "The TeV Physics of Strongly Interacting W's and Z's," *Nucl.Phys.B* **261** (1985), no. 379.

[40] Sarah Allwood, 2005. Talk at ATLAS Physics workshop (Rome). http://indico.cern.ch/conferenceDisplay.py?confId=a044738.

[41] Englert, C. and Jager, B. and Worek, M. and Zeppenfeld, D. , "Observing Strongly Interacting Vector Boson Systems at the CERN Large Hadron Collider," 0810.4861.

[42] "ATLAS Detector Description." http://boudreau.home.cern.ch/boudreau/v-atlas-hepvis.htm.

[43] The ATLAS Collaboration, "The ATLAS Experiment at the CERN Large Hadron Collider," *JINST 3 S08003* (2008).

[44] V. A. Mitsou, "The ATLAS Transition Radiation Tracker," *Como* (2003) 497–501, hep-ex/0311058.

[45] **ATLAS** Collaboration, A. Airapetian *et. al.*, "ATLAS calorimeter performance,". CERN-LHCC-96-40.

[46] ATLAS, "Detector and physics performance technical design report, cern/lhcc/99-15," 1999.

[47] R. Achenbach *et. al.*, "The ATLAS Level-1 Calorimeter Trigger," *JINST* **3** (2008) 03001.

[48] M. W. A. Gupta, "Jet Energy Calibration in the ATLAS detector using DC1 samples," *ATLAS internal note, CERN-ATL-COM-2005,002* (2005).

[49] Jack J. Dongarra, Piotr Luszczek and Antoine Petitet, "The LINPACK benchmark: past, present and future," *Concurrency Computat.: Pract. Exper.* **15** (2003) 803–820.

[50] "Medipix collaboration." http://medipix.web.cern.ch/MEDIPIX.

[51] T. Holý *et. al.*, "Data acquisition and processing software package for medipix2," *Nucl. Instr. and Meth. A* **563** (2006), no. 112.

[52] M. Campbell, C. Leroy, S. Pospisil and M. Suk, 2006. MPX-USB-ATLAS-2006, CERN.

[53] P. Abreu *et. al.*, "DELPHI," *Phys. Lett. B* **446** (1999), no. 62 hep-ex/9903072.

[54] DELPHI Coll. DELPHI Note 2000-032 (CONF 2000-004).

[55] P. N. S. Frixione, M.L. Mangano and G. Ridolfi, "Top quark distributions in hadronic collisions," *Phys. Lett. B* **351** (1995), no. 555 hep-ph/9503213.

[56] R. N. Cahn, S. D. Ellis, R. Kleiss, and W. J. Stirling, "Transverse momentum signatures for heavy higgs bosons," *Phys. Rev.* **D35** (1987) 1626.

[57] R. Kleiss and W. J. Stirling, "Tagging the higgs," *Phys. Lett.* **B200** (1988) 193.

[58] Barger, Vernon D. and Han, Tao and Phillips, R. J. N., "Improving the heavy higgs boson two charget lepton - two neutrino signal," *Phys. Rev.* **D37** (1988) 2005–2008.

[59] V. D. Barger, K.-m. Cheung, T. Han, and D. Zeppenfeld, "Single forward jet tagging and central jet vetoing to identify the leptonic W W decay mode of a heavy Higgs boson," *Phys. Rev.* **D44** (1991) 2701–2716.

[60] A. Dobado, M. J. Herrero, and J. Terron, "W+- Z0 signals from the strongly interacting symmetry breaking sector," *Z. Phys.* **C50** (1991) 465–472.

[61] G. Azuelos, P.-A. Delsart, J. Idárraga *et.al.*, "DC2 Note," *ATL-COM-PHYS* **041** (2006).

[62] "The ATLAS Trigger for early running." ATLAS Trigger groups.

[63] S. Catani, Y. L. Dokshitzer, M. H. Seymour, and B. R. Webber, "Longitudinally invariant K(t) clustering algorithms for hadron hadron collisions," *Nucl. Phys.* **B406** (1993) 187–224.

[64] J. M. Butterworth, J. P. Couchman, B. E. Cox, and B. M. Waugh, "KtJet: A C++ implementation of the K(T) clustering algorithm," *Comput. Phys. Commun.* **153** (2003) 85–96, `hep-ph/0210022`.

[65] M. Cacciari and G. P. Salam, "Dispelling the N**3 myth for the k(t) jet-finder," *Phys. Lett.* **B641** (2006) 57–61, `hep-ph/0512210`.

[66] J. M. Butterworth, B. E. Cox, and J. R. Forshaw, "WW scattering at the LHC," *Phys. Rev. D* **65** (2002) `hep-ph/0201098`.

[67] E. Stefanidis, "UCL PhD Thesis," 2007.

[68] Atlas Collaboration, "The ATLAS Experiment at the CERN Large Hadron Collider," *JINST 3 S08003* (2008).

[69] Higgs group of the ATLAS collaboration, "Higgs to tau tau," 2008. CSC Note in preparation.

[70] V. D. Barger, K.-M. Cheung, T. Han, J. Ohnemus, and D. Zeppenfeld, "A comparative study of the benefits of forward jet tagging in heavy higgs production at the ssc," *Phys. Rev.* **D44** (1991) 1426–1437.

[71] CMS, "Technical Design Report, CERN/LHCC/94-33," 1994.

[72] K. Iordanidis and D. Zeppenfeld, "Searching for a heavy Higgs boson via the H –> l nu j j decay mode at the CERN LHC," *Phys. Rev.* **D57** (1998) 3072–3083, hep-ph/9709506.

[73] D. L. Rainwater and D. Zeppenfeld, "Observing $h \to w^{(*)}w^{(*)} \to e^{\pm}\mu^{\mp}\not{p}_t$ in weak boson fusion with dual forward jet tagging at the cern lhc," *Phys. Rev.* **D60** (1999) 113004, hep-ph/9906218.

[74] T. Sjostrand, S. Mrenna, and P. Skands, "Pythia 6.4 physics and manual," *JHEP* **05** (2006) 026, hep-ph/0603175.

[75] CMS Collaboration, "CMS Physics TDR," *J.Phys.G* **34** (2007) 995–1579.

[76] S. Asai *et. al.*, "Prospects for the search for a standard model Higgs boson in ATLAS using vector boson fusion," *Eur. Phys. J.* **C32S2** (2004) 19–54, hep-ph/0402254.

[77] S. Alekhin *et. al.*, "Hera and the lhc - a workshop on the implications of hera for lhc physics: Proceedings part a," hep-ph/0601012.

[78] J. Idárraga, G. Azuelos and P.-A. Delsart, "Fundamental interactions," *Proceedings of the 22nd Lake Louise Winter Institute* (2007) 305–310.

[79] M. Campbell, E. Heijne, T. Holý, J. Idárraga *et. al.*, "Study of the charge sharing in a silicon pixel detector by means of α-particles interacting with a Medipix2 device," *Nucl. Instr. Methods* **A591** (2008) 38–41.

[80] M. Fiederle, D. Greiffenberg, J. Idárraga *et. al.*, "Energy calibration measurements of the Medipix2," *Nucl. Instr. Methods* **A591** (2008) 75–79.

[81] J. Bouchami, A. Gutiérrez, A. Houdayer, J. Idárraga, C. Leroy *et. al.*, "Study of the charge sharing in silicon pixel detector with heavy ionizing particles interacting with a Medipix2 device." Accepted for publication in Nucl. Instr. Methods A, 2009.

[82] J. Bouchami, A. Gutiérrez, A. Houdayer, J. Idárraga, C. Leroy *et. al.*, "Study of the charge sharing in silicon pixel detector with heavy ionizing particles interacting with a Medipix2 and Timepix devices." Accepted for publication in the proceedings of the IEEE2008 conference, Dresden, 2009.

[83] G. C. Blazey *et. al.*, "Run II Jet Physics," *Batavia* (1999) 47–77, hep-ex/0005012.

[84] S. D. Ellis *et. al.*, "Jets in hadron-hadron collisions," *Prog.Part.Nucl.Phys.* (2008), no. 60 484–551, arXiv:0712.2447v1.

[85] F. Maltoni and T. Stelzer, "MadEvent: Automatic event generation with MadGraph," *JHEP* **02** (2003) 027, hep-ph/0208156.

[86] M. L. Mangano, M. Moretti, F. Piccinini, R. Pittau, and A. D. Polosa, "Alpgen, a generator for hard multiparton processes in hadronic collisions," *JHEP* **07** (2003) 001, hep-ph/0206293.

[87] M. L. Mangano, M. Moretti, and R. Pittau, "Multijet matrix elements and shower evolution in hadronic collisions: W b anti-b + (n)jets as a case study," *Nucl. Phys.* **B632** (2002) 343–362, hep-ph/0108069.

[88] F. Caravaglios, M. L. Mangano, M. Moretti, and R. Pittau, "A new approach to multi-jet calculations in hadron collisions," *Nucl. Phys.* **B539** (1999) 215–232, hep-ph/9807570.

[89] e. J. Alwall, "Comparative study of various algorithms for the merging of parton showers and matrix elements in hadronic collisions," arXiv:0706.2569.

[90] The GEANT4 Collaboration S. Agostinelli *et.al.*, "GEANT4 - A Simulation Toolkit," *Nuclear Instruments and Methods in Physics Research, NIM A* **506** (2003) 250–303.

[91] "Geant4." http://geant4.cern.ch.

[92] "Geant4 collaboration." http://geant4.cern.ch/collaboration.

[93] D. Costanzo *et. al.*, "Validation of the geant4-based full simulation program for the atlas detector: An overview of performance and robustness," *ATL-SOFT-PUB* **002** (2005).

[94] The ATLAS collaboration, "Letter of Intent for a General-Purpose pp Experiment at the Large Hadron Collider at CERN," *CERN/LHCC/92-4* **92-4** (1992).

[95] Elzbieta Richter-Was, Daniel Froidevaux and Luc Poggioli, "ATLFAST 1.0," *ATLAS Internal Note PHYS-NO-079* (1996).

Appendix I

Offline Jet Reconstruction

Jet Reconstruction [83] is based on a sequence of operations that take as input, elements of the hadronic calorimeter to build a Jet object. The set of operations compose the jet building algorithm (see for example [83]).

The algorithm starts from a list of calorimeter *components* which can be any kind of input object one can build at experimental level such as, calorimeter-towers (see section I.1). Ideally, the role of the algorithm is to reverse the process of parton showering and hadronization occurring after a hard process. It associates clusters of these components into jets such that the kinematic properties of the jets (e.g., momenta) can be related to the corresponding properties of the energetic partons produced in the hard scattering process (when comparing to hadronic information from the montecarlo). Thus the jet algorithm allows us to reconstruct the parton level topology from the hadronic final state. The differences between the parton level and the calorimeter level is a major consideration for a jet algorithm.

I.1 Algorithm input

Calorimeter input elements can be defined in different ways. The following two generic definitions are commonly used in ATLAS.

- Calorimeter Towers: piles of calorimeter cells (see section 2.2) in a certain window in the $\eta \times \phi$ space.
- Topological Clusters: group of calorimeter cells with energy deposition above a critical noise level, based on their neighbor relations such as the energy difference between them. Also the significance of their energy contents is taken into account.

However, in general terms, the cone, i.e. the jet, can be filled with any calorimeter cell-based object (proto jet) one may be able to build.

I.2 Cone algorithm

The geometrical definition of a jet is as follows. A cone of radius R_{cone}, consists of all of the calorimeter input elements (components) that lie in an area $A = \pi R^2$ of $\eta \times \phi$ space. Once a cone has been selected in the calorimeter, we require, by a process of iteration, that the axis of the cone coincides with the jet direction as defined by the p_T-weighted centroid [84] of the components within the cone. The p_T-weighted centroids are calculated for the particles in each cone and are used as centers for new cones in the $\eta \times \phi$ space. When the algorithm reaches such a situation the cone is said to be stable. In principle, one simply searches for all such stable cones to define the jet content of a given event. In practice, in order to save computing time, the iterative process of searching for stable cones in experimental data, starts with those regions of the calorimeter centered about the most energetic components in the event (so-called *seeds*). Generally a energy cut is applied to the seeds.

Final stable cones in a given event may overlap. Meaning that a given particle may belong to two or more cones. A procedure must be included in the algorithm to specify how to split overlapping cones [83].

To illustrate the functioning of the algorithm, we show in Fig. I.1: a) the E_T in towers in a few MC generated jets, and b) the directions of pull between iterations moving toward the position of the actual jets. We clearly see how in this rather simple event the algorithm successfully finds the jets.

I.3 $k_\perp$ algorithm

The $k_\perp$ algorithm is based on pair-wise recombination scheme intended, in some sense, to undo the splitting that occurs during the fragmentation stage. Hadrons interact with matter to make hadronic showers and undergo proto-jet splitting. It makes it difficult to compare with parton level as discussed at the beginning of this appendix.

The algorithm then proceeds as follows. Looping over all pair combinations of calorimeter objects (towers for example), the one with least relative transverse momentum is combined into one jet if this relative p_T is less than a given value. This is called a

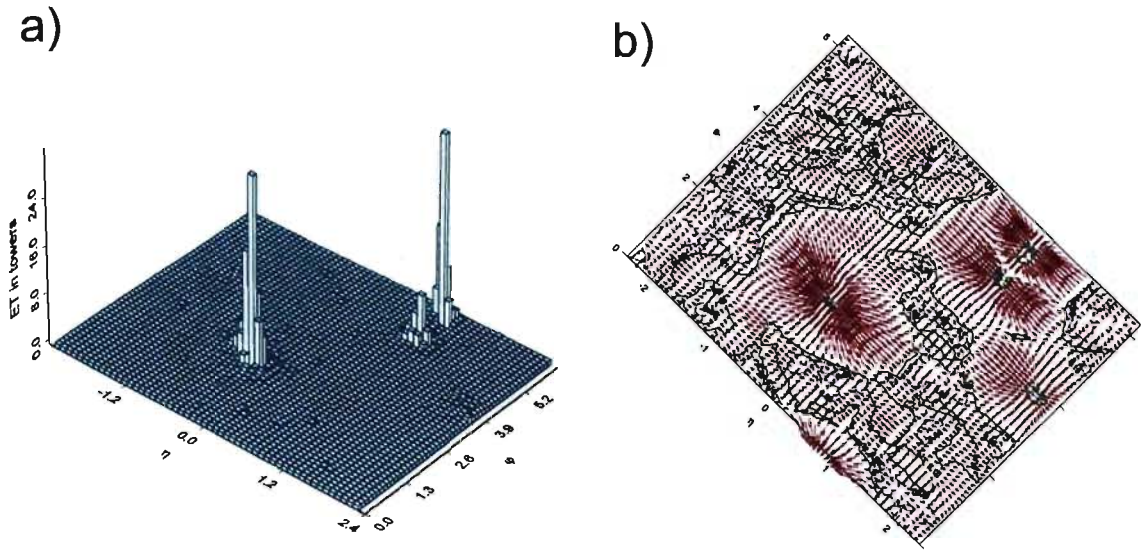

Figure I.1: (An ideal) Monte Carlo generated event with 2 large energy jets and 1 small energy jet in the LEGO plot a), and the corresponding flow structure of the trial cones in b).

clustering process. The $k_\perp$ algorithm is infrared and collinear safe, i.e. the solutions are insensitive to soft or collinear radiation of partons (which are singular).

For each tower, which at this stage is called proto-jet, the following quantities are calculated

$$\begin{aligned} k_{T,i}^2 &= p_{T,i}^2, \\ k_{T,(i,j)}^2 &= \min(p_{T,i}^2, p_{T,j}^2)\frac{\Delta R_{i,j}^2}{D^2} \end{aligned}$$

for each protojet i and each pair of proto-jets ij, respectively. $p_{T,i}$ is the transverse momentum of the i^{th} proto-jet and $\Delta R_{i,j}$ is the distance (in y, ϕ space, $\Delta R_{i,j} = \sqrt{(y_i - y_j)^2 + (\phi_i - \phi_j)^2}$) between each pair of proto-jets. D is the parameter that controls the size of the jet (analogous to R_{cone}). If the smallest of the above quantities is $k_{T,i}^2$, then that proto-jet becomes a jet and is removed from the proto-jet list. If the smallest quantity is a pair combination $k_{T,(i,j)}^2$, then the two proto-jets (i, j) are merged into a

single proto-jet by summing their four-vector components, and the two original entries in the proto-jet list are replaced by this single merged entry. This process is iterated with the corrected proto-jet list until all the proto-jets have become jets, *i.e.*, at the last step the $k^2_{T,(i,j)}$ for all pairs of proto-jets are larger than all $k^2_{T,i}$ for the proto-jets individually (*i.e.*, the remaining proto-jets are well separated).

Appendix II

Monte Carlo Generators

The Monte Carlo (MC) generators used in the main analysis are as follows.

- PYTHIA [74] version 6.4.0.3 was used for the signal, with the CTEQ6L parton distribution function and the renormalisation and factorisation scale $Q^2 = M_Z^2 + p_T^2(j)$. This scale is appropiate for vector boson scattering [12]. The hard process was modified to include new vector boson scattering amplitudes.

- MADGRAPH [85], version 3.95, with PYTHIA for parton shower, hadronisation and underlying event, was used for W+jets and Z+jets backgrounds. The default values of fixed renormalisation and factorisation scales of $Q^2 = m_Z^2$ were set and CTEQ6L1 parton distribution functions were used. This scale is pessimistic for the backgrounds. A more realistic scale, $Q^2 = m_Z^2 + \sum p_T^{j\,2}$ reduces the cross sections by as much as a factor 2 for the samples in our study.

Studies showed that the major effect is on the cross-section rather than on event shapes, and the cross section normalisation was determined independently.

The underlying event samples were tuned to data from previous experiments [77]. ALPGEN [86, 87, 88] is also used for some generator level comparisons.

II.1 Matrix element generation with MADGRAPH

Matrix element generators like MADGRAPH yield an appropriate description of events for well separated jets away from the collinear region (see collinear approximation in next section). It also carries the exact calculations for interference and spin correctly. In the case of MADGRAPH it is done by using Feynman diagrams and helicity amplitude method [85].

In section 3.2.2 we show a few Feynman diagrams which MADGRAPH calculates to produce W + 4jets background. In Fig. II.1 we show a few more as calculated by the

generator.

As MADGRAPH is used to generate a given sample it does the following steps:

- Identifies all the Feynman diagrams and creates Fortran code for the matrix element squared. The models implemented are: SM, SUSY, 2HDM and others [85].
- Matrix element generation for arbitrary processes. It can handle tree-level processes with up to 8 particles in the final state.
- It uses a helicity amplitude method, meaning that diagrams which do not interfere because of different helicity in the final state are separated before squaring.
- Phase space integration and event generation.
- Displays all the diagrams in postcript format as those in Fig. II.1. Also a web-based output is available. It shows the results for each process, where their separate cross section contribution can be monitored as the results are available. A screen-shot of such output page is shown in Fig. II.2.
- Produces an output file containing the event generation.

The number of diagrams and processes that have to be calculated with MADGRAPH for the backgrounds used in this work, is enormous. This was discussed already in section 3.2.2.

II.2 Parton shower and hadronization with PYTHIA

In general, whenever generating events with a Matrix element generator such as MADGRAPH, we leave to PYTHIA the work of producing the parton shower and hadronization since this non-perturbative step is well tuned in PYTHIA [74]. It is said to be universal, i.e., it is independent on the physics process behind the final state and it is still a first principle description. The parton shower comprises the following elements:

- Describes successive QCD bremsstrahlung emissions, or splitting of partons.

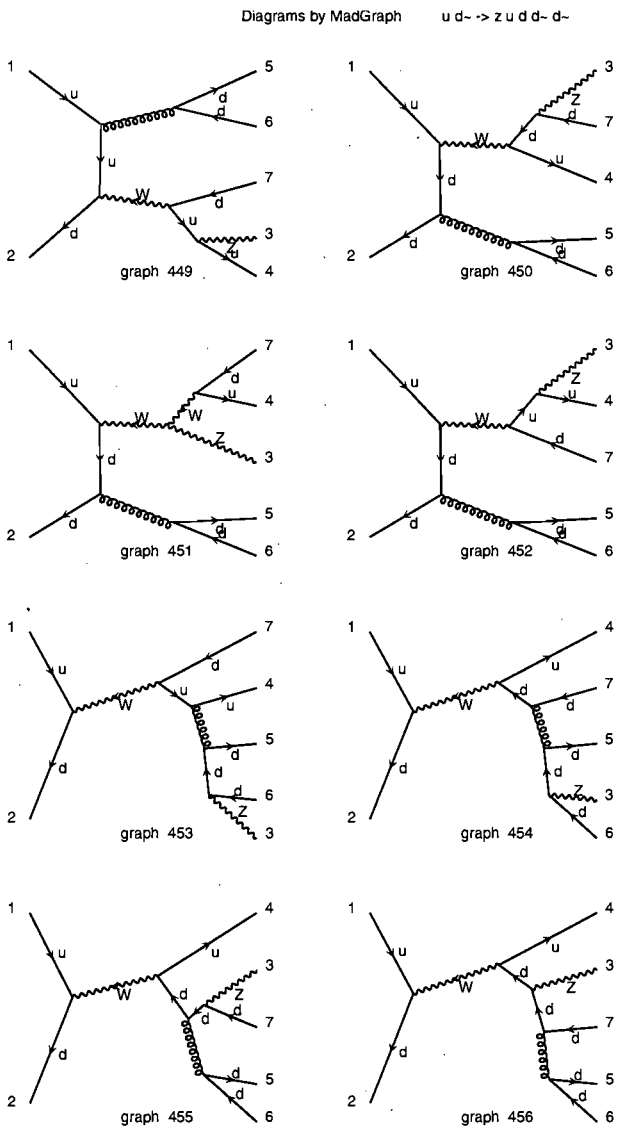

Figure II.1: A few diagrams of $Z + 4$ jets $(\alpha_s^2, \alpha_{ew}^3)$ background. The total number of diagrams is 157008. In this figure we see diagrams corresponding to the scattering of $u\bar{d} \to Zud\bar{d}\bar{d}$ contributing to $Z + 4$ jets.

Graph	Cross Sect(fb)	Error(fb)	Events (K)	Eff	Unwgt	Luminosity
Sum	**1040.106**	**20.409**	**734366**	**531.7**		
du_zudgg	71.360	1.142	1605	20.3		19.10
ud_zudgg	70.805	1.151	1341	18.8		20.10
ug_zuddxg	67.034	1.899	1960	39.7		19.10
gu_zuddxg	64.742	1.687	1706	34.0		19.90
ug_zdsxcg	62.082	1.527	781	21.8		19.40
gu_zdsxcg	62.065	1.516	1179	26.5		19.90
uu_zuuddx	31.368	0.434	1487	16.9		21.60
uu_zudsxc	29.568	0.552	577	14.2		27.90
gd_zuuxdg	29.415	0.677	1687	29.9		24.30
dg_zuuxdg	29.299	0.781	1617	33.9		23.50
dg_zuscxg	26.054	0.597	1011	23.1		26.40
gd_zuscxg	25.758	0.672	553	19.4		25.10
uux_zddxgg	10.180	0.155	1271	17.1		52.40
uxu_zddxgg	10.143	0.154	1558	18.9		56.70
ud_zudddx	9.876	0.146	1809	19.9		86.50
du_zudddx	9.868	0.151	1378	18.0		52.50
du_zuuuxd	8.475	0.130	1600	19.3		64.50
ud_zuuuxd	8.293	0.127	1582	19.2		92.00
⋮						
gsx_zsxccxg	2.761	0.070	1756	33.8		158.00
gs_zsccxg	2.752	0.069	1928	34.9		243.00
udx_zuddxdx	2.737	0.033	1128	13.0		124.00
uu_zuussx	2.703	0.038	1404	16.9		131.00
dxu_zuddxdx	2.683	0.035	1106	13.8		229.00
gg_zssxccx	2.660	0.080	1921	41.6		218.00

Figure II.2: Part of the web-based output of the MADGRAPH generator showing a few interesting values, like the cross section, for each process contributing. This listing corresponds to $Z+4$ jets $(\alpha_s^2, \alpha_{ew}^3)$ background. The process highlighted (`udx_zuddxdx`, i.e. $u\bar{d} \to Zu\bar{d}d\bar{d}$) corresponds to those diagrams in Fig. II.1.

- Uses, soft, collinear approximation (Leading Logarithm Approximation): The probability of emitting QCD radiation in the direction of the momentum of a parton is infinite. There is also a soft radiation singularity. These lead to large

logarithm terms in the splitting of partons. The leading logarithm term is taken into account (resummed to all orders of α_S).

II.3 Matching: Matrix element vs parton shower

As mentioned in section 3.3.1, the matching procedure avoids double counting of jets produced by the parton shower in PYTHIA. In Table II.I we show a comparison between the two scenarios

Matrix elements	**Parton shower**
• Requires lots of CPU time	• Not very CPU-expensive
• Limited number final state particles	• Virtually no limit
• Valid when partons are hard and well separated	• Valid when partons are collinear and/or soft
• Interference taken into account correctly	• Partial quantum interference considered
• Needed for multi-jet description	• Needed for hadronization/detector simulation

Table II.I: Differences between matrix elements calculations and parton shower to deal with hadronic final sates.

Matrix element and Parton showers are indeed complementary approaches. Both are necessary in high-precision studies of multijet processes. One need to combine them avoiding the double counting. This is implemented in ALPGEN and in the latest version of MADGRAPH. The idea behind matching is described in [89]. We use matrix element description for well separated jets and parton shower for collinear jets. In order to separate the two regions a phase-space cutoff is used.

Appendix III

Geant4 simulation

Geant4 is a radiation-matter-interaction simulation kit [90, 91] developed by the Geant4 collaboration [92] which allows one to simulate the interaction between radiation and matter for any desired 3D geometry, material, and custom radiation composite medium. Geant4 has many functionalities:

- Geometry builder in 3 dimensions. Any desired 3D geometry can be built and placed in a virtual space where a given virtual experiment is going to take place.
- A vast number of predefined materials can be used to fill up a given geometry component. The user can define new materials if needed.
- Physics processes for electromagnetic and hadronic interactions, radiative decays, photon-matter processes, among many others, are available. Their ability to describe accurately the physics processes that the radiation undergoes while it encounters matter, has been validated over a wide energy range, typically from a few keV to hundreds of GeV. Also, heavy ion physics and neutron-matter interaction packages are available. Recently, a package for very low energy electromagnetic processes (down to a wavelength of hundreds of nanometers, i.e. visible light) has been introduced and is presently in the process of being validated [91].

III.1 Full simulation of the ATLAS detector

The *Full simulation of the ATLAS detector* [93] was first started when the letter of intent [94] of the experiment was published in 1992. The simulation of the ATLAS detector allows one to study the desired perfomance of the detector in a fairly realistic scenario.

On Fig. III.1 we see a 3D representation of a VBF process as simulated by Geant4. We can see, in the central part, the three components of the Inner Detector (Pixel, SCT

and TRT. See section 2.1) and the tracks that particles leave in it (in white, blue and red). We also see part of the services (cabling and external signals) of the hadronic and electromagnetic calorimeters (in gray). On the rear side (left) we see part of the muon spectrometer in dark red and green.

Here, we can very easily identify, in a graphical way, the type of reconstruction we describe in chapter 4. For instance, for this one event in Fig. III.1, which corresponds to the signal $qqWZ \rightarrow qqjj\ell\ell$ ($m = 1.1$ TeV), we can distinguish the following elements: two high p_T leptons (muons in this case) in the central region which are the yellow dots in the back (right), hadronic activity due to forward jets (in sea-blue, close to the beam-pipe in both sides of the detector) and hadronic activity in the central region (also in sea-blue). Fig. III.1 shows the typical signature of VBS at high energy as simulated by Geant4.

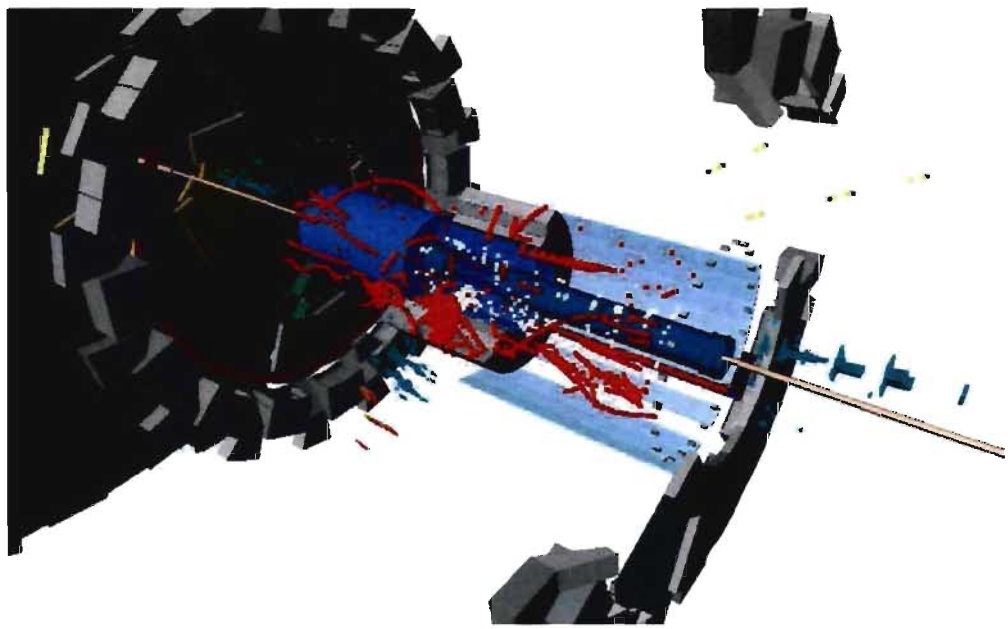

Figure III.1: A 3D representation of a VBF process as simulated by Geant4 taking into account the whole ATLAS geometry.

The geometry of the ATLAS experiment, is known to be one of the most complex implementations ever done with the Geant4 package (others can bee seen at [91]). The details of the geometry building, the collection of energy in the calorimeters or the track-

ing facilities are not given here because it is a vast topic, strongly software oriented, and beyond the scope of this thesis. The output of the simulation, i.e. energy deposition and tracks, are the inputs of the reconstruction algorithms used to identify the observable particles (final states), are described in sections 4.2.2.1, 4.2.2.2 and the appendix I.

III.2 ATLFast simulation

ATLFAST [95] is an effort to do a very fast (non CPU-time consuming) simulation of final state radiation in the ATLAS detector. The full simulation is very expensive in terms of CPU-time (as discussed in section 3.2.2) and for quick studies it is desirable to have a fast facility for simulation even if it is not as realistic as the full simulation. In brief, besides applying geometric acceptance, smearing of the particles is performed in energy and direction by some optimized resolution functions. Efficiency factors are also applied for identification of b quarks, electrons, etc.

A lot of work comparing the full and fast simulations has been done in the past. In the case of VBS, some signals were simulated in both scenarios and compared [10]. In this work, only full simulation was used.